Dissertation

Intra-operative Nuclear Imaging Based on Positron-emitting Radiotracers

Dzhoshkun Ismail Shakir

Fakultät für Informatik

Chair for Computer–Aided Medical Procedures (CAMP)

Intra–operative Nuclear Imaging Based on Positron–emitting Radiotracers

Dzhoshkun Ismail Shakir

Vollständiger Abdruck der von der Fakultät für Informatik der Technischen Universität München zur Erlangung des akademischen Grades eines

Doktors der Naturwissenschaften (Dr. rer. nat.)

genehmigten Dissertation.

Vorsitzende(r): Univ.-Prof. Dr. Burkhard Rost

Prüfer der Dissertation:

1. Univ.-Prof. Dr. Nassir Navab
2. apl. Prof. Dr. Sibylle Ziegler
3. Prof. Pierre Jannin, Ph.D.
   Université de Rennes 1 / Frankreich

Die Dissertation wurde am 24.09.2013 bei der Technischen Universität München eingereicht und durch die Fakultät für Informatik am 25.02.2014 angenommen.

Contents

List of Figures

List of Tables

Bismillāhirraḥmānirraḥīm

(In the Name of God, the Most Gracious, the Most Merciful)

Acknowledgments

All praise is due to God, Lord of the Worlds for His countless blessings on me.

I would like to acknowledge the endless help, advice and support of my family and friends, without whom my research work would not have been possible.

This PhD thesis is the fruit of a kind and continuous guidance provided by Prof. Dr. Nassir Navab, Prof. Dr. Sibylle Ziegler, and Dr. Tobias Lasser. I would like to thank Prof. Dr. Nassir Navab for his tireless efforts in transforming his students into strong people capable of handling tough real–life challenges.

I would like to thank Dr. Tobias Lasser and Florian Schneider for proofreading the thesis with very valuable feedback; Dr. Tobias Lasser and Alexandru Duliu for valuable discussions during the development of our software framework; Alexander Hartl, Aslı Okur, José Gardiazabal, Philipp Matthies, Bernhard Fürst for their kind support on many occasions and valuable discussions; Dr. Melanie Hohberg, Sebastian Fürst, Dr. Ralph Bundschuh, Ian Somlai Schweiger, and the medical technical assistants from the Department of Nuclear Medicine for their support especially with the experimental part.

I would like to acknowledge Dr. Farhad Daghighian from IntraMedical Imaging LLC for kindly providing the technical specifications of the probes we have used. I would like to thank the staff of SurgicEye GmbH, especially Dr. Thomas Wendler, Stefan Wiesner, John–Michael Fischer for their technical support.

I would like to thank the whole Chair for Computer–Aided Medical Procedures for making my stay very comfortable and pleasant, and in particular (apart from those already mentioned) Dr. Asad Ali Safi, Dr. Tobias Reichl, Mehmet Yiğitsoy, Jakob Vogel, Martina Hilla, and Vasileios Belagiannis. In addition I would like to acknowledge Florian Schneider, Dr. Jožef Pulko, Dr. Kuangyu Shi, and Zhen Liu, who made working in IFL a very nice experience for me.

I gratefully acknowledge the generous support of my funding sources: TUM Graduate School, TUM Graduate School of Information Science in Health (GSISH), DFG SFB 824, and DAAD PROCOPE. Finally, I thank the Technische Universität München for the opportunity of becoming part of a great academic environment.

Dzhoshkun Ismail Shakir

Abstract

Positron–emitting radiotracers are an important part of nuclear medical imaging processes. Besides the very famous glucose analog [^{18}F]FDG, many not so well known ones exist, among them the particularly interesting amino acid–based tracers like [^{18}F]FET. Although peri–operative imaging with positron–emitting radiotracers has become state–of–the–art in cases of many types of cancer, their capability is not fully exploited in the operating room yet. In this thesis we explore two intra–operative nuclear imaging modalities exploiting different aspects of positron radiation towards quality assurance in challenging surgical treatment scenarios. The first modality *freehand PET* provides a tomographic image of a volume of interest and aims at minimizing invasiveness by assisting the surgeon in pinpointing target structures marked with a radiotracer. The second imaging modality *epiphanography* generates an image of the radiotracer distribution on a surface of interest and aims at providing a means for improving the control of tumor resection margins. The word *epiphanography* is a compound of the Greek words επιφάνεια (*epiphaneia*) for *surface* and ζωγραφιά (*ographia*) for *image*, and hence means *the image of the surface* similar to the compound τόμος (*tomos*) for *slice/volume* and ζωγραφιά (*ographia*) for *image*, meaning *the image of the volume*, i.e. *tomography*. To our knowledge this is the first use of the word *epiphanography* in the context of nuclear medical imaging. In this thesis we present our approach to modeling, developing and calibrating these two novel imaging modalities. In addition, we present our work towards their clinical integration. In the case of freehand PET, we have already acquired the first intra–operative datasets of a patient. We present this first experience in the operating room together with our phantom studies. In the case of epiphanography, we present our phantom studies with neurosurgeons towards the integration of this imaging modality into the challenging surgical therapy of low–grade glioma patients.

Keywords: Intra–operative Imaging, Radio–guided Cancer Surgery, Nuclear Navigation, Positron Emission Tomography, PET

Zusammenfassung

Positronen–emittierende radioaktive Tracer spielen eine wichtige Rolle in der nuklearmedizinischen Bildgebung von heute. Neben des berühmten [^{18}F]FDG, gibt es zahlreiche andere Tracer. Besonders interessant sind Aminosäure–basierte Tracer wie zum Beispiel [^{18}F]FET. Obwohl im nuklearmedizinischen Alltag viele unterschiedliche Krebsarten durch tomographische Bildgebung mit Positronen–emittierenden radioaktiven Tracern diagnostiziert werden, nutzt ihr Einsatz im Operationssaal noch nicht alle Möglichkeiten aus. In dieser Doktorarbeit untersuchen wir zwei neue intra–operative nuklearmedizinische Bildgebungsmodalitäten, die jeweils auf unterschiedlichen Aspekten der Positronenstrahlung basieren, zum Zweck der Qualitätssicherung in anspruchsvollen chirurgischen Behandlungsszenarien. Die erste Bildgebungsmodalität, *Freehand PET*, bietet dem Chirurgen Unterstützung bei der genauen Lokalisierung radioaktiv–markierter Zielkörperstrukturen durch tomographische Bilder eines bestimmten begrenzten Volumens, um die Invasivität zu minimieren. Die zweite Bildgebungsmodalität, *Epiphanography*, bietet dem Chirurgen Unterstützung zur besseren Bestimmung der Tumorenresektionsgrenzen durch ein Bild der radioaktiven Tracerverteilung auf der Oberfläche des Tumorenbettes. Das Wort *Epiphanography* besteht aus den griechischen Wörtern für *Oberfläche* (*epiphaneia*: επιφάνεια) und für *Bild* (*ographia*: ζωγραφιά), und bedeutet somit *das Bild der Oberfläche* ähnlich zu der Kombination der Wörter für *Volumen/Schnitt* (*tomos*: τόμος) und für *Bild* (*ographia*: ζωγραφιά), also *das Bild des Volumens*, oder *Tomographie*. Unseres Wissens ist dies die erste Verwendung des Wortes *Epiphanography* im Kontext der nuklearmedizinischen Bildgebung. In dieser Doktorarbeit stellen wir unseren Ansatz zur Modellierung, Entwicklung und Kalibrierung dieser neuartigen Bildgebungsmodalitäten vor. Zudem stellen wir unsere Forschungsarbeit in Richtung ihrer klinischen Integration vor. Im Falle von Freehand PET wurde das System bereits für erste intra–operativen Datensätze von einem Patienten eingesetzt. Wir stellen diese erste klinische Erfahrung zusammen mit unseren Phantomstudien vor. Im Falle von Epiphanography stellen wir unsere Phantomstudien mit Neurochirurgen zur Integration dieser Bildgebungsmodalität in die anspruchsvolle neurochirurgische Behandlung von Patienten mit niedrig–gradigen Gliomen vor.

Stichwörter: Intra–operative Bildgebung, Radio–geführte Krebschirurgie, Nuklearе Navigation, Positronen–Emissions–Tomographie, PET

Part I.

Medical & Technical Background

CHAPTER 1

Introduction

THE term *cancer* has in the recent decades gained widespread and increasingly non–specific use in the colloquial of the man on the street. There is no need to write a lengthy introduction to prove the importance of this class of diseases, as the term itself sufficiently scares the masses today. Nevertheless, we find it appropriate to give the (especially non–medical) reader a very brief introduction about the biological process of cancer, laying emphasis on important medical terminology.

When the cellular mechanisms that control cell growth and cell division do not function properly, i.e. the rate of cell division cannot be regulated, the cells start dividing beyond control [Guyt 11, Chapter 2]. Such uncontrollably dividing cells can start forming new tissue masses – *neoplasms*, or *tumors*. In addition, they can start spreading into other tissues, or *metastasize*, forming *metastases*. Tumors that do not invade nearby tissue, nor metastasize are called *benign*, whereas the ones that do are called *malignant*. It is these malignant tumors that are medically classified as *cancerous* or under the meanwhile very liberally used term *cancer*. Cancer has many types, but typically the cell type that has started a cancer is reflected when referring to that specific cancer type. For instance *glioma* is a class of tumors that originates from the *glial* cells (more information in section 2.1). The suffix *–oma* indicates tumorous growth. Another example is *lymphoma*, i.e. cancer that begins in the cells of the immune system (*lymph*) [NCI 13].

The severity of a cancer in a patient is assessed by *staging*, based on *the extent*

of the tumor (T), whether the cancer has spread to neighboring *lymph nodes (N)*, and finally whether it has *metastasized (M)* to other parts of the body. This is the foundation of the *TNM staging system*. Although used for most types of cancer, this system is not used in e.g. brain and spinal cord tumors, which are staged based on their cell type and *grade* (to be defined and discussed in section 2.1.1) [Canc 13].

Treatment options for cancer include, but are not limited to *surgery*, *radiotherapy*, *chemotherapy*, *targeted drug therapy*, *palliative therapy*. Very frequently a combination of different treatment options is applied. The same cancer type may also require different treatment in its different stages. Our focus within this thesis is on the surgical treatment option.

1.1. Competing Goals of Cancer Surgery

THE primary goal of cancer surgery is to remove tumor masses. In addition, lymph nodes may also be removed for therapeutic and/or staging purposes. When removing a tumor mass, the resection usually includes additional healthy tissue around the tumor (or *peri–tumoral tissue*), called a *margin*. This serves the purpose of ensuring that no part of the tumor is missed. Any (even small) non–resected tumor mass is called *residual tumor* and may occasionally cause the tumor to regrow, i.e. to *recur*. In case of recurrence, the whole surgery might have to be repeated. Nonetheless, the resection can obviously not be extended indefinitely due to the associated loss of nearby healthy tissues: the risk of negative side effects to the health after the surgery (or *post–operative morbidity*) is an important factor to consider. This risk can be so high that even some part of the tumor may be left deliberately. In addition, aesthetic motivations for preserving tissues might exist. Another factor that makes tumor resection a challenge is the presence of nearby vital structures like blood vessels and/or nerves. In summary, avoiding recurrence and minimizing post–operative morbidity are the two competing goals of cancer surgery. More detailed information together with two specific classes of tumors is presented in the main part (specifically see section 5.1 and section 6.1) of this thesis.

1.2. Research Objectives of Our Work

OUR research work is aimed at extending the spectrum of radio–guidance in surgery by exploiting the capabilities of positron–emitting radiotracers for intra–operative imaging modalities. These radiotracers have become/are becoming state–of–the–art for imaging many different types of cancer. Nonetheless, their capability is not fully exploited in the *operating room (OR)*, due to the bulky devices needed for imaging. The aim of this thesis is to introduce two novel *intra–operative* (i.e. that can be used *during the surgery*) imaging modalities that work in conjunction with positron–emitting radiotracers for providing real–time information and guidance. The first modality is called *epiphanography* and is based on the direct detection of *positrons*. The second one called *freehand PET (fhPET)* is a PET–like[1] imaging modality, based on the detection of *annihilation gamma rays*[2]. Each imaging modality can be utilized separately, although a combination is also possible, if required.

In this thesis we present the technicalities of these two imaging modalities together with the feasibility studies for each of the two medical application scenarios we have considered so far, namely the surgical treatment of *glioma* and *head and neck cancer*.

1.3. Document Organization

THE next chapter of the thesis presents information about glioma, and head and neck cancer in some detail. The subsequent chapter introduces the fundamental concepts relevant to medical nuclear imaging, especially focusing on PET. The last chapter of this part gives a brief overview of available or emerging intra–operative approaches in conjunction with positron–emitting radiotracers.

The second part of the thesis outlines the contributions of our research work: we dedicate a chapter for each imaging modality. Each chapter begins by elaborating on the relevance of the respective imaging modality to the corresponding medical application scenario. A brief overview of the respective system setup follows this. Then we present our work for calibrating the different components of the respective imaging modality, and talk about the studies conducted in order to prove the feasibility of the respective imaging modality. Finally we discuss the main pitfalls

[1] PET: positron emission tomography

[2] A detailed discussion on these two types of radiation is provided in section 3.2.1.

of the system that need to be addressed on the way to the full integration into the clinical workflow.

We conclude this thesis in the third part by giving an outlook on future work.

CHAPTER 2

Medical Background

THIS chapter gives very brief information about the pathology, treatment, and state–of–the–art imaging of two specific types of tumors relevant to our discussion: *glioma of the central nervous system (CNS)*, and *head and neck squamous cell carcinoma (HNSCC)*. These constitute the first two medical application scenarios for our intra–operative imaging modalities. The reader familiar with the medical aspect of these diseases may skip this whole chapter.

2.1. Glioma

2.1.1. Pathology & classification

The term *glioma* refers to one specific class of more than 120 types of brain tumors that grow from *glial cells* of the brain [Theo 12]. Glial cells include the following types [McPh 08]:

- *Astrocytes* transport nutrients and hold neurons in place
- *Oligodendrocytes* provide the necessary insulation (*myelin*) to neurons
- *Microglia* digest dead neurons and also pathogens
- *Ependymal cells* line the ventricles and secrete cerebrospinal fluid

Primary brain tumors[1] including gliomas do not metastasize to other organs of the body. This is the reason why they do not fit into the term *cancer* [Theo 12]. Nonetheless, brain tumors may invade nearby tissues of the brain and usually manifest themselves with symptoms like headaches, numbness, weakness, personality changes and confusion, and seizures [McPh 08]. Gliomas are divided into the following three types:

- *Astrocytoma*
- *Oligodendroglioma*
- *Glioblastoma*

The World Health Organization (WHO) classification of brain tumors is different than other types of tumors. It involves merely the *grade* of the tumor, which refers to the appearance of the tumor cells under the microscope, and which gives an idea of the aggressiveness of the tumor. There are four grades associated with gliomas:

1. *Grade I – pilocytic astrocytoma* occurs mostly in children. This is the least aggressive type, as the cells are slow growing and are almost normal in appearance [Theo 12]. *Prognosis*, or the predicted outcome in terms of curability, is very favorable for this type of gliomas.

2. *Grade II – low–grade glioma* typically occurs in adults between 20 – 50 years of age. This type includes *astrocytoma*, *oligodendroglioma*, and *mixed oligoastrocytoma*. This is an infiltrative type whose cells grow relatively slowly but have slightly abnormal appearance. This type can be invasive. In addition, it can evolve into higher grade.

3. *Grade III – malignant glioma* includes *anaplastic astrocytoma*, *anaplastic oligodendroglioma*, and *anaplastic mixed oligoastrocytoma*[2]. This is a very invasive type of glioma.

[1] A primary brain tumor refers to a tumor that has started and developed in the brain. It is also possible for another tumor in the body to metastasize to the brain.

[2] *Anaplastic* means that the cell exhibits some loss of structural *differentiation*, or specialization (especially during embryonic development, cells undergo *differentiation* – i.e. become different than the *zygote*, the first cell after fertilization – towards specific types of cells, e.g. nerve cells, liver cells, blood cells). Therefore differentiation in this context refers to cell specialization – a *well differentiated* cell means a specialized cell. *Anaplasia* refers to the reversion of some cell type to a more primitive form [Medi 13].

4. *Grade IV – glioblastoma multiforme (GBM)* is the most aggressive form of primary brain tumor. It tends to spread very quickly and invade other parts of the brain [McPh 08].

2.1.2. Symptoms & diagnosis

More than 359,000 persons in the United States are estimated to be suffering from a primary brain or central nervous system tumor. More than 195,000 U.S. Americans are annually diagnosed with a brain tumor. Brain tumors are the most common form of solid tumor affecting children [Brai 12]. Gliomas constitute about half of all brain tumors [Theo 12]. Symptoms of a glioma are strongly related to the part of the brain where it occurs. Certain symptoms are quite specific due to this relation. The most obvious sign of a brain tumor in infants is a rapidly widening head or bulging crown. Generally speaking, headaches are the most common symptom [Brai 12]. As the brain is responsible for regulating the vast number of all types of body functions, symptoms vary from relatively harmless ones like behavioral and emotional changes to very severe ones like paralysis on one side of the body or vision loss. First diagnosis is made based on a neurological exam to check the mental status and memory, cranial nerve function (sight, hearing, smell, tongue and facial movement), muscle strength, coordination, reflexes, and response to pain. State–of–the–art non–invasive imaging is performed with *magnetic resonance imaging (MRI)* and/or *X–ray computed tomography (CT)*. Quite substantial information can be obtained with these imaging modalities (see figure 2.1). Nonetheless, in some cases biopsy may be needed to determine the type of the tumor. Biopsy can be performed as part of a neurosurgical tumor removal procedure or standalone. In case of a tumor in a deep and critical location, a *stereotactic biopsy* is performed by using a *stereotactic head frame* and a computer for biopsy needle guidance [Theo 12]. *Functional MRI (fMRI)* is used for showing the distance between brain tumors and specific functional areas of the brain. *Magnetic resonance spectroscopy (MRS)* can be used for analyzing the chemical make–up of brain tumors [Brai 12]. Other diagnostic tools used for brain tumors are *electroencephalography (EEG)*, *positron emission tomography (PET)*, *ultrasound (US)* imaging and *single photon emission computed tomography (SPECT)* [Neur 11]. PET is becoming increasingly popular on the one hand due to the introduction of novel radiotracers like [^{18}F]FET, and on the other hand due to its improved sensitivity and specificity compared to other state–of–the–art imaging technologies in some cases.

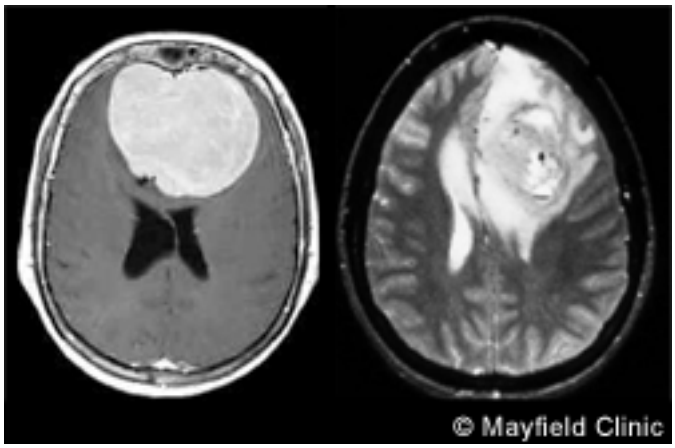

Figure 2.1.: Appearance of brain tumors in MRI. **Left:** a benign brain tumor. **Right:** a malignant brain tumor. Note that the benign tumor has well–defined borders contrary to the irregular borders of the malignant tumor. Benign tumors are easier to remove surgically due to this, while the finger–like projections of malignant tumors make them surgically challenging. ***Copyright notice:*** *Image reprinted from [Theo 12]. Used with permission from the Mayfield Clinic.*

These advantages of PET over the state–of–the–art neuroimaging modalities like MRI and CT are going to be covered in detail later in the text (see section 5.1).

2.1.3. Treatment

Treatment options depend on the grade of the tumor. Mere observation of the progress is an option for grade I tumors and in cases where the tumor is located in the functional areas of the brain. In other cases where it is possible to remove the whole tumor without causing function loss, surgical resection is the treatment of choice. Complete removal can be curative for grade I and II gliomas. Grade I and II gliomas, where surgery is not an option or where there is (slow) residual tumor growth, are candidates for radiotherapy. Grade III and IV gliomas are much more challenging: maximal removal is recommended for tumors in non–functional areas. Usually post–operative treatment is also needed, which is achieved by radiotherapy, chemotherapy or a combination of both. Recurrence is also very common for these two grades. Therefore more aggressive treatment like repeated surgery, radio- and chemotherapy might be needed. In some cases, radioactive seeds are surgically implanted into the tumor region for local radiotherapy [Brai 12]. In ad-

dition, novel chemotherapy drugs, immunotherapy, and vaccines are being clinically investigated as standalone solutions or in combinations [McPh 08]. For more detailed information, see e.g. [Brai 13]. Symptomatic treatment might also be necessary in cases of severe symptoms like seizures [Brai 12].

2.2. Head & Neck Squamous (Epithelial) Cell Carcinoma

2.2.1. Pathology & classification

The top thin surface of the structures of the head and neck region (throat, *larynx* – a.k.a. voice box, nose, sinuses, and mouth, illustrated in figure 2.2) is called the *epithelium* and is made up of flat, *squamous* cells. Most tumors in this region are caused by an abnormal growth of these cells. These tumors can invade deeper layers of nearby tissue and can also metastasize to other parts of the body. It is these malignant tumors that are categorized under the term *head and neck squamous cell carcinoma (HNSCC)*. HNSCCs are classified by the part of the body where they start:

- *Laryngeal and hypopharyngeal cancers* start in the larynx or the *hypopharynx* (the lower part of the throat surrounding the larynx).
- *Nasal cavity and paranasal sinus cancers* start in the nasal cavity (the space just behind the nose) or paranasal sinuses (the air–filled areas surrounding the nasal cavity).
- *Nasopharyngeal cancers* start in the *nasopharynx* (the air passageway at the upper part of the throat behind the nose).
- *Oral and oropharyngeal cancers* start in the oral cavity (mouth and tongue) or *oropharynx* (middle part of the throat from the tonsils down to, but excluding the larynx).
- *Salivary gland cancers* start in the salivary glands, which produce saliva.

HNSCCs are staged using the TNM staging system:

1. *Stage 0* means a *carcinoma in situ* (*Tis*), i.e. a cluster of malignant cells that has not yet invaded the deeper epithelial tissue or spread to other parts of the body [Medi 13], with no lymph node (LN) involvement (*N0*), nor distant metastasis (*M0*).

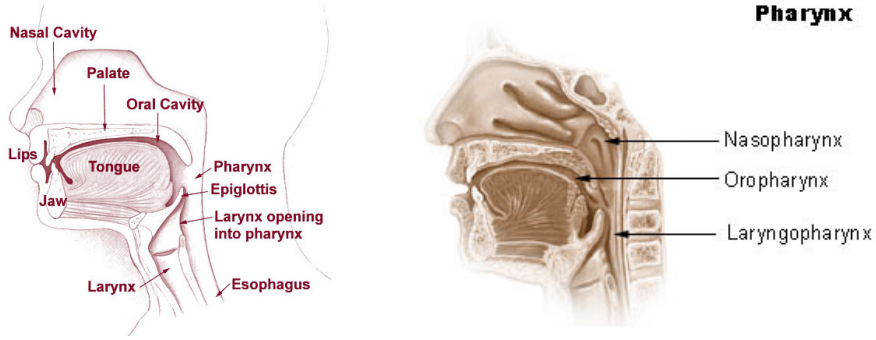

(a) Head and neck anatomy.

(b) The pharynx.

Figure 2.2.: Overview of the different parts of the head and neck anatomy. 2.2(a) ***Copyright notice:*** *Image reprinted from [SEERb].* 2.2(b) ***Copyright notice:*** *Image reprinted from [SEERa].*

2. *Stage I* is a small tumor (*T1*), with no LN involvement (N0), nor distant metastasis (*M0*).

3. *Stage IIA* is an invasive tumor (*T2*), with no LN involvement (N0), nor distant metastasis (M0).

4. *Stage IIB* is a T1 or T2 tumor, with LN involvement (*N1*), but no distant metastasis (M0).

5. *Stage III* is either of:

   - T1 or T2 tumor, with LN involvement (N1 or *N2*)
   - larger tumor (*T3*), with or without LN involvement (N0, N1, or N2)

   yet, with no distant metastasis (M0).

6. *Stage IVA* is either any invasive tumor (*T4*), with either of:

   - no LN involvement (N0)
   - same–sided LN involvement (N1), but no distant metastasis (M0)

   or any T type, with significant LN involvement (N2), yet no distant metastasis (M0).

7. *Stage IVB* is any T type tumor with extensive LN involvement (*N3a* or *N3b*), but no distant metastasis (M0).

Stage	Tumor	Lymph Node	Metastasis
0	Tis	N0	M0
I	T1	N0	M0
IIA	T2	N0	M0
IIB	T1/T2	N1	M0
III	T1/T2	N1/N2	M0
	T3	N0/N1/N2	M0
	any T	N2	M0
IVA	T4	N0	
	T4	N1	M0
	any T	N2	M0
IVB	any T	N3a/N3b	M0
IVC	any T	any N	M1

Table 2.1.: Stages of HNSCC based on the TNM system.

8. *Stage IVC* is any T and N type tumor, with distant metastasis (*M1*).

For an overview of these stages, see table 2.1. In addition to the stage, the grade is also used for describing an HNSCC:

1. *GX* means that the grade cannot be evaluated.
2. *G1* cells look similar to the typical cells of the healthy tissue (well differentiated).
3. *G2* cells are only moderately different than healthy cells.
4. *G3* cells do not look like the typical cells (poorly differentiated).

For a more in–depth discussion with graphical illustrations, see [Head 12].

2.2.2. Symptoms & diagnosis

The clinical workflow starts when the patient shows up with complaints in the head and neck region. These are usually related to a tumor mass that is *palpable*, i.e. can be felt with the touch of the hand, by the patient himself. The most common symptom of HNSCC is a swelling or sore throat that does not heal. However symptoms can be very specifically related to the site of the tumor. They can vary from seemingly harmless ones like a foul mouth odor to more severe ones like loosening of teeth or double vision [SEERb]. The doctor usually examines the

patient with ultrasound (US) and makes the hypothesis for the treatment based on this. Very often no other imaging modality is used pre–operatively. However CT, MRI, and/or PET may also be used for imaging head and neck tumors, as well as any related metastases. Beside the usual blood and/or urine tests for diagnosis, endoscopy and/or biopsy may be performed [Head 12].

2.2.3. Treatment

Early detection gives a much better prognosis for the patient. Due to the sensitive locations of head and neck tumors, doctors from many disciplines may be involved in the treatment. Preservation of vital structures like blood vessels and nerves in the head and neck anatomy, as well as obvious aesthetic motivations are important considerations in the treatment.

The main treatment options for HNSCC are surgery, radiotherapy, chemotherapy, targeted therapy and palliative/supportive care. Surgery aims at resecting the tumor mass with additional peri–tumoral healthy tissue. LN removal, i.e. *dissection* might also be performed during surgery (or standalone), in case of suspicion of nodal involvement and/or metastasis. In addition surgery might include reconstructive (plastic) surgery in cases where major tissue removal is performed (like for instance removal of the jaw, tongue). Reconstructive surgery aims at restoring the appearance and/or lost functionality to the most possible extent. Surgery might be followed by radio- and/or chemotherapy in case of residual tumor due e.g. to sensitive tumor location. Pre– and post–therapy care are very important in case of radiotherapy, as radiotherapy may lead to severe post–therapy morbidity like loss of speech and/or hearing. Targeted therapy involves the use of e.g. gene–specific drugs to block the growth and spread of cancer cells while minimizing damage to healthy cells. It can be an option for some sub–classes of HNSCC where the involvement of a specific gene is known [Head 12].

CHAPTER 3

Medical Nuclear Imaging Basics

THIS chapter presents the concepts of medical nuclear imaging in a nutshell, from the physiological fundamentals of radiotracers, through the briefly mentioned physical and mathematical foundations behind image generation, to the final step of visualizing the acquired information for use by the surgeon and/or nuclear medicine specialist.

3.1. Radiotracers

A *radiotracer* or a *radiopharmaceutical* is a specific biochemical molecule that is associated with a specific physiological pathway in the body and that is labeled with a *radioactive isotope* (or *radioisotope* in short). An example, as will be explored in detail in the following subsection, is *[^{18}F]Fluoro–2–deoxy–2–D–glucose* and the physiological pathway it is coupled to is the glucose metabolism. When administered in a human, a radiotracer allows for imaging the volumetric distribution of (the intensity of) the physiological function it is associated with.[1] Although radiotracers are used for many different purposes, we focus on their use for non–invasive imaging in *oncology*, the branch of medicine that deals with tu-

[1] According to the *tracer principle*, a radioactive isotope of an element takes part in (bio–)chemical reactions, e.g. the body's physiological pathways, exactly the same way as its non–radioactive isotopes would do [Wern 04]. In other words, the physiology of a biochemical molecule is the same regardless of whether its atoms are radioactive or not.

mors. Although the imaging hardware is interested only in the radioisotope within the radiotracer molecules, it is imperative to understand the physiology of the utilized radiotracer in order to really comprehend what story an image has to tell about a patient. We look at the radiotracer physiology at three levels, namely:

a) how it interacts at the biochemical (cellular) level

b) once it enters the body, how it is distributed

c) what possible complications exist with regard to the imaging process

With direct connection to the physiology, we also give a brief overview about the radiation dosimetry aspect of radiotracers. Last but not least, we briefly present how radiotracers are prepared. Following this outline, we confine this very broad topic to the two radiotracers that are of interest in the scope of this thesis, namely *[^{18}F]Fluoro–2–deoxy–2–D–glucose ([^{18}F]FDG)* and *O–(2–[^{18}F]Fluoroethyl)–L–tyrosine ([^{18}F]FET)*.

3.1.1. [^{18}F]Fluoro–2–deoxy–2–D–glucose

[^{18}F]Fluoro–2–deoxy–2–D–glucose is usually abbreviated as [^{18}F]FDG or simply as FDG in literature. [^{18}F]FDG represents more than 95 % of clinical indications in oncology [Fant 10, Chapter 2, pp 8]. [^{18}F]FDG is transported into cells by *glucose transporters* (which are specific molecules by which glucose is transported into the cell as well – see [Guyt 11, Chapter 4]). Therefore [^{18}F]FDG essentially *imitates* glucose (for the molecular structure of [^{18}F]FDG see figure 3.1), i.e. it is a glucose *analog*. However the way it is processed *inside* the cell is different than glucose and it is important to explain this difference in order to understand how [^{18}F]FDG can *label* tumors.

Glucose is the main energy source of the human body. When transported into the cell, glucose undergoes a biochemical process called *glycolysis*[2], at the end of which it is decomposed into *pyruvate*. Pyruvate may later enter the cellular *aerobic*, i.e. *using oxygen*, respiration, where it is fully oxidized to carbondioxide and water. *Anaerobic* respiration is also possible when the oxygen supply of the cell is low. In any case, glycolysis is the essential first step for making use of the energy trapped in a glucose molecule, and in glycolysis one of the first steps is the attachment of *phosphate* to glucose (see [Kyrk 12]), which is called *phosphorilation*.

[2]For a very good interactive animation of glycolysis, see [Kyrk 12].

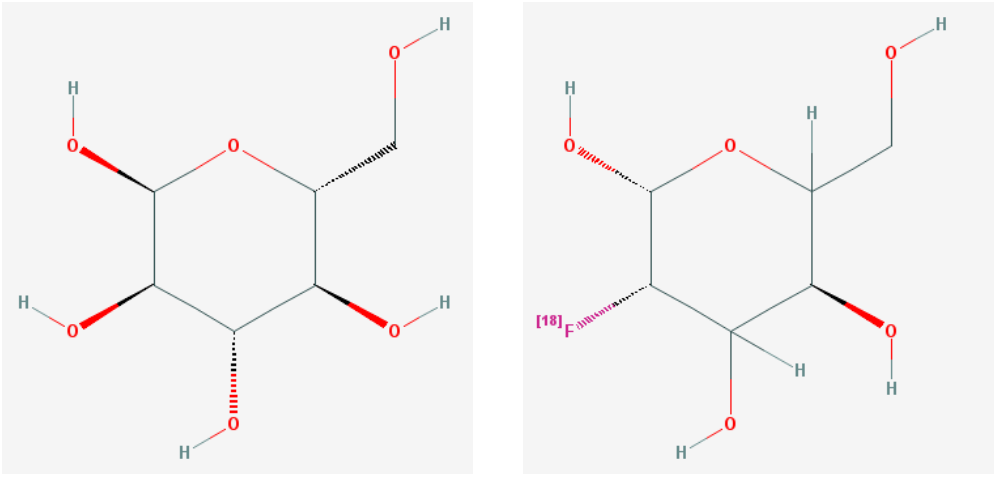

(a) Molecular structure of glucose.

(b) Molecular structure of [^{18}F]FDG.

Figure 3.1.: Molecular structures of glucose and [^{18}F]FDG. Note how ^{18}F is attached in 3.1(b). ***Copyright notice:*** *Both images reprinted from [The 13a].*

[^{18}F]FDG on the other hand, cannot be metabolized any further after its phosphorilation (*[^{18}F]FDG–6–phosphate*) in the glycolytic pathway. In addition, due to the insufficient amount of the enzyme *glucose–6–phosphatase*, the phosphorilation cannot be reversed. This causes the [^{18}F]FDG–6–phosphate molecules to accumulate within the cells. The elevated glycolysis and glucose transport levels of many types of tumor cells make this accumulation more pronounced for tumors than the peri–tumoral healthy tissues [18FF 05]. This is the underlying physiological mechanism by which [^{18}F]FDG is used for the imaging of many types of tumors[3].

After the intra–venous administration of [^{18}F]FDG in a patient, it is cleared from the blood circulation and incorporated into tissues very rapidly. The organs with the largest [^{18}F]FDG uptake are the brain (8 %), liver (5 %), heart wall (4 %) and lungs (3 %). As [^{18}F]FDG is primarily excreted in the urine, the urinary bladder has a very high accumulation (24 %) as well (the numbers in parantheses are the fractional distributions of the original activity) [Vale 08]. This phenomenon may lead to false negatives due to the high *background* radiation from these organs in cases where the targeted tumors and/or metastases are close to these organs. This issue is especially pronounced for radio–guided surgeries in conjunc-

[3]It is an interesting anecdote that historically [^{18}F]FDG was synthesized after *2–Deoxy–D–glucose (2DG)* had been developed with the purpose of inhibiting the utilization of glucose by cancer cells [18FF 05].

tion with [^{18}F]FDG. In addition, muscles [Jack 06] and inflammated tissue [Ishi 02] are well–known for high [^{18}F]FDG uptake. The former is the reason why patients to undergo an [^{18}F]FDG–PET examination are asked to lie in a relaxed position with the least amount of talking possible following the administration of [^{18}F]FDG. [^{18}F]FDG–PET image acquisition is usually performed at least $60\ min$ *post–injection*, due to the fact that [^{18}F]FDG uptake into tumors peaks and plateaus at different points in time, depending on the tumor tissue kinetics. Special cases may require that [^{18}F]FDG–PET acquisition be made $90 - 120\ min$ post–injection [Shan 06].

The average effective dose a patient would get from an [^{18}F]FDG–PET study is $29\ \mu Sv/MBq$.[4] [^{18}F]FDG is usually administered in several hundreds of MBq, and the total effective dose is around $7.0\ mSv$ per [^{18}F]FDG–PET examination [Brix 05]. To give the unfamiliar reader a contextual figure of the magnitude of the radiation dose; a full–body CT scan causes a total effective dose of $18\ mSv$ [Brix 05]. According to the United States Nuclear Regulatory Commission (NRC), an employee working in a radiation–related field like nuclear medicine should not receive more than $50\ mSv$ annually. NRC also states that $4 - 5\ Sv$ received in a very short period is expected to cause half of the exposed population to die within 30 days (see *"lethal dose"* in [NRC 12a]). In addition, NRC reports that 134 employees fighting the fire right at the Chernobyl power plant in 1986 received doses between $0.7\ Sv$ and $13.4\ Sv$. 28 of those died from the injuries associated with this exposure [NRC 12b].

Today the radioactive isotope ^{18}F is produced by bombarding enriched ^{18}O–water with protons in a *cyclotron* or a *linear particle accelerator*. This nuclear reaction is denoted by

$$^{18}\mathrm{O}\ (p, n)\ ^{18}\mathrm{F}$$

where p stands for protons and n for neutrons (released by the reaction). [^{18}F]FDG is then obtained as the result of a complex chemical reaction depicted in figure 3.2 with high *purity* and high *yield* [Fowl 05]. ^{18}F has a *half–life*[5] of $109.77\ min$ [Chu 99], which allows for shipping to satellite clinical centers after production. The half–life of positron emitters is the primary physical characteristic to be considered in order to reliably use the radiotracer on patients [Fant 10, Chapter 2, pp 9].

[4] For a recent extensive review of radiopharmaceutical dosimetry, see the work of Eberlein *et al.* [Eber 11]

[5] Explained in section 3.2.1.

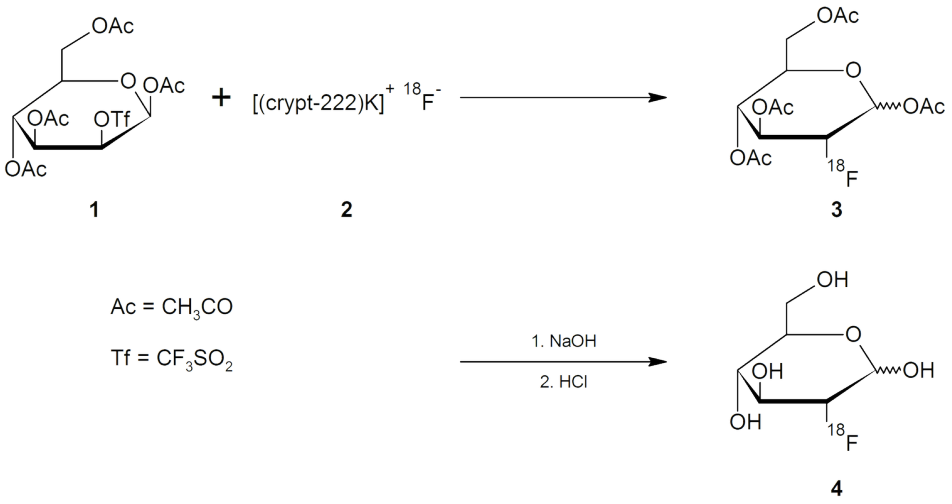

Figure 3.2.: The chemical reaction by which [^{18}F]FDG is produced.

3.1.2. O–(2–[^{18}F]Fluoroethyl)–L–tyrosine

O–(2–[^{18}F]Fluoroethyl)–L–tyrosine is an *amino acid* analog. It is usually abbreviated as [^{18}F]FET in literature. *Tyrosine*, whose molecular formula is depicted in figure 3.3, is a non–essential amino acid[6]. Tyrosine plays an important role for the brain as it is a building block for several *neurotransmitters*[7]. Tyrosine is also involved in many other proteins serving different purposes in the body [Ehrl 11]. Natural amino acids like tyrosine are transported in high quantities into tumor cells due to the fact that tumor cells have over–expressed transport systems, and these amino acids are indeed retained in the cells for incorporation into proteins. This type of amino acids can serve as an agent for imaging *cell proliferation*, which is increased in a cell malignancy like cancer [Jage 01]. On the other hand, O–(2–[^{18}F]Fluoroethyl)–L–tyrosine is an *L–tyrosine analog*[8], i.e. among the set of synthesized amino acids, which are never incorporated into proteins within the cell; but which nonetheless are transported at a high rate into the cell [Leun 05]. Other

[6]The body normally makes tyrosine from another amino acid called *phenylalanine*. The name *tyrosine* involves the Greek word τυρί (*turí* or alternatively *tyros*) for *cheese*, and the chemical suffix *–ine*. This name was coined in 1846 by the German chemist Baron von Justus Liebig, who first discovered it, as tyrosine was easily obtained from old cheese [Harp 12].

[7]Neurotransmitters take part in the communication between nerve cells. Examples of neurotransmitters are *epinephrine*, *norepinephrine*, and *dopamine*.

[8]The prefix *L–* indicates that this chemical compound is transported into the cells mainly (70 %) by the *system L transport mechanism*. The remaining 30 % of the transport is achieved via the *sodium–dependent system B*^{0} [Leun 05].

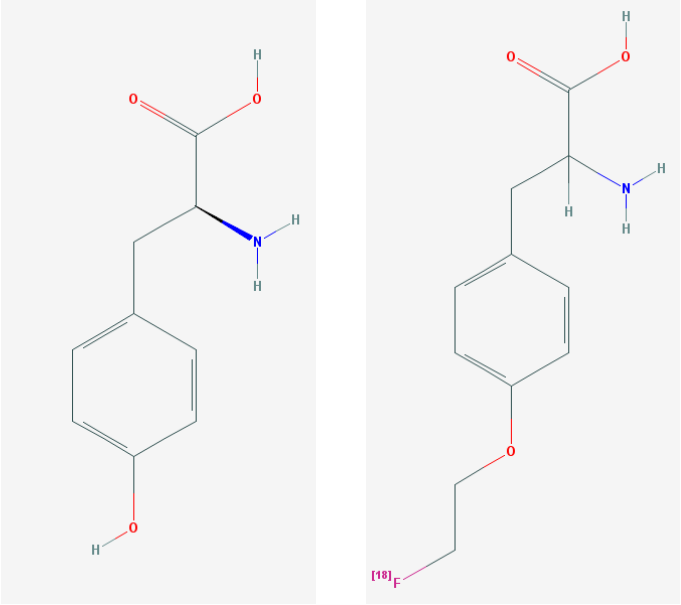

(a) Molecular structure of tyrosine.

(b) Molecular structure of [^{18}F]FET.

Figure 3.3.: Molecular structure of tyrosine and [^{18}F]FET. Note how ^{18}F is attached. ***Copyright notice:*** *Both images reprinted from [The 13a].*

than as building blocks of proteins, amino acids are used in many functions within the cell, such as the *activated methyl cycle*, the *initiation of the translation of ribonucleic acid (RNA) code*. They may even be used as intermediary metabolites for metabolic fuel. All this knowledge suggests that imaging the rate of amino acid transport into the cells is more helpful for localizing malignancies than imaging only protein synthesis. In addition, studies have shown that this mechanism works even when protein synthesis is inhibited [Jage 01].

Pauleit *et al.* studied the distribution of [^{18}F]FET in the human body [Paul 03]. In this study featuring seven patients with different types of brain tumors or unspecific brain lesions, a peak of radioactivity in the blood and a plateau of constant radioactivity were observed $1.5\ min$ and $20\ min$ post–injection respectively. Two whole–body scans were performed for each patient $70\ min$ and $200\ min$ respectively, after intra–venous administration of $400\ MBq$ [^{18}F]FET. The brain showed an uptake of about 2 % of the total activity in both scans. The highest amount of uptake was observed in the muscles with 39.2 % and 32.6 % mean values in the early and later scans respectively. The non–brain organs with the largest up-

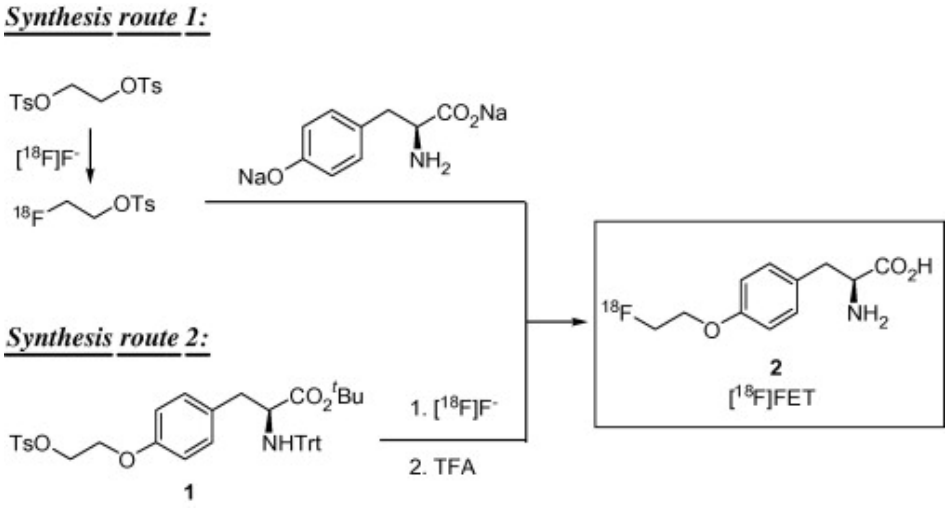

Figure 3.4.: The chemical reaction schemes for producing [^{18}F]FET. For a more detailed discussion see [Bouv 12]. ***Copyright notice:*** *Reprinted from [Bouv 12], with permission from Elsevier.*

take following the muscles were the liver (3.1 %, 2.7 %), the lungs (2.3 %, 2.0 %) and the bone marrow (2.2 %, 2.1 %). Pauleit *et al.* also report that the effective dose to a patient from a [^{18}F]FET–PET study is $16.5\ \mu Sv/MBq$. In a typical study involving $370\ MBq$ of injected activity, this amounts to $6.1\ mSv$ total effective dose [Paul 03]. The very problematic issue of unspecific uptake of [^{18}F]FDG in inflammatory tissues exists for labeled amino acids like [^{18}F]FET as well. However due to the fact that inflammatory cells have a lower protein metabolism compared to glucose metabolism, the problem is not so severe as in the case of [^{18}F]FDG. For [^{18}F]FET unspecific uptake is related to *ischemic brain areas, infarction, scar tissue, abscess, sarcoidosis, irradiated areas, hemangiomas*, among others [Jage 01]. There are two commonly used reaction schemes for producing [^{18}F]FET. Both are depicted in figure 3.4.

3.2. Radiation in a Nutshell

THIS section gives a brief overview of the scientific and technical fundamentals of medical imaging. First we talk about nuclear physics, focusing on gamma and beta radiation. Secondly we give an overview of the design of hardware elements used for detecting radiation.

3.2.1. Radiation fundamentals

An atomic nucleus consists of particles called *nucleons*. There are two types of nucleons:

- A *proton* has one unit of positive fundamental electronic charge.
- A *neutron* has no electronic charge.

Each element in the periodic table is uniquely identified by its proton count, or *atomic number* (denoted by Z). The number of neutrons (denoted by N) in atoms of a specific element may be different. Such different atoms of an element are called *isotopes of that element*. An isotope of an element G is denoted by its atomic number and its *mass number* $A = Z + N$ in the following manner: ${}^{A}_{Z}G$ (for instance ${}^{18}_{9}F$ or simply ${}^{18}F$). An atom also has particles of unit negative fundamental electronic charge each, called *electrons*. Electrons are not found in the nucleus, but orbit around it. The atomic number Z is associated with the number of electrons (of a non–ionized atom), and due to the fact that chemical reactions of an atom involve, generally speaking, only its outermost electrons, this number determines the chemical properties of a specific element. In other words, different isotopes of an element have the same chemical properties [Wern 04].

Each nucleon has a *standalone* mass denoted by:

- the mass of a proton M_H (i.e. a hydrogen nucleus)
- the mass of a neutron M_n

The atomic (nuclear) mass of an element ${}^{A}_{Z}G$ is denoted by $M(A, Z)$. One would therefore expect:

$$M(A, Z) = Z \cdot M_H + (A - Z) \cdot M_n \tag{3.1}$$

However in reality the following holds:

$$M(A, Z) < Z \cdot M_H + (A - Z) \cdot M_n \tag{3.2}$$

The difference in mass is related to the energy that holds the nucleons together (*binding energy*), based on Einstein's famous formulation $E = mc^2$ of energy (E) with respect to mass (m) and the speed of light (c) [Eins 05], in the following manner:

$$B_{tot} = [Z \cdot M_H + (A - Z) \cdot M_n - M(A, Z)] \cdot c^2 \tag{3.3}$$

In principle, the higher *the binding energy per nucleon*, the more stable the nucleus.

The *shell model* of the nucleus states that the nucleons, which move in orbits around one another, may produce different discrete *configurations* of their geometric positions with respect to each other. Only some of such configurations are *allowed*, meaning that others are not possible. Each such allowed configuration represents a *discrete energy state*. Nucleons may re–arrange from one allowed configuration to another, changing the energy level from E_{old} to E_{new}. The difference between these two ΔE increases the binding energy, while decreasing the atomic mass:

$$\Delta E = E_{old} - E_{new} \tag{3.4}$$

$$B_{new} = B_{old} + \Delta E \tag{3.5}$$

$$M_{new} = M_{old} - \Delta E/c^2 \tag{3.6}$$

The optimal configuration such that the overall energy is minimal is called the *ground state*. The energy difference ΔE is released in a number of ways, and this phenomenon is called *radioactive decay*. In a given time interval, a constant fraction of the initially present radioactive atoms undergoes radioactive decay. The temporal aspect of radioactive decay is characterized by the *half–life* of a radioactive isotope: half–life is the time required for half of the initially present radioactive atoms to undergo decay. *Activity* is defined as the rate of generation of radioactive decay. It is measured in *disintegrations (unitless) per second* (i.e. the number of atomic nuclei that decay per second). So the unit is a second–inverse (s^{-1}), which – for this particular case of radiation – is called a *Becquerel* (Bq) in the SI unit system[9]. Radioactive particles have energies on the order of 10^{-19} $Joules$ (J), making a more convenient energy unit necessary. This is the rationale behind the introduction of the *electron–volt* (eV), which is equivalent to $1.602176487 \times 10^{-19}$ J [Levi 04].

There are different types of radioactive decay. We will confine our discussion to the mode of decay relevant to this thesis, namely *positron emission*[10]. In this type of radioactive decay, a proton is converted into a neutron in the nucleus. The positive electric charge of the converted proton is emitted as a *positron* (β^+ or e^+) from the nucleus, as well as an elementary sub–atomic particle called a *neutrino* (ν_e). This

[9] *Curie* (Ci) is also an older unit used. 1 Ci is equivalent to 3.7×10^{10} Bq

[10] The interested reader may consult [Levi 04] and the references provided there for a more detailed discussion of all types of radioactive decay.

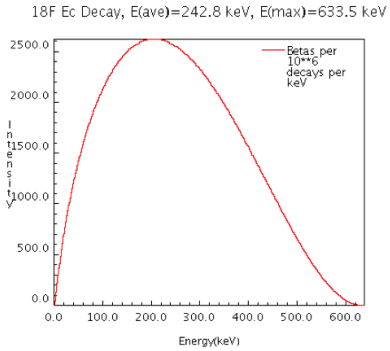

Figure 3.5.: The spectrum of ^{18}F positron energies. ***Copyright notice:*** *Courtesy of Richard B. Firestone [Chu 99].*

can be denoted as:

$$ {}^{A}_{Z}P \rightarrow {}^{A}_{Z\text{-}1}D \qquad n \rightarrow p + e^{+} + \nu_e $$

The emitted positron has kinetic energy up to a maximum value, denoted by $Q_{\beta+}$ or simply Q [Levi 04]. Each kinetic energy value in this range has a specific probability. This probability distribution varies from one isotope to another. ^{18}F emits positrons with a maximum kinetic energy of $633.5\ keV$ (for the whole energy spectrum see figure 3.5) [Chu 99].

3.2.1.1. Interactions of positrons

Positrons emitted from isotopes used in diagnostic nuclear imaging undergo two main types of interactions in matter:

- *Inelastic collisions* with atomic electrons
- *Elastic collisions* with atomic nuclei

Inelastic collisions lead to energy transfer from the positron to an electron. The cumulative effect of many such collisions manifests itself in the positron losing its whole kinetic energy, and coming to a halt. At or near this halting point in space, the positron combines with a nearby atomic electron (which is its *anti–particle*), and *annihilation* occurs, i.e. their charges neutralize each other, and their combined mass energy of $2\times\ 511\ keV = 1,022\ keV$ is converted into two (almost) oppositely directed *photons* (*annihilation gamma rays* or simply *gamma rays*) of $511\ keV$ each[11].

[11]The annihilating positron and electron are not at rest when annihilating. Therefore due to the law of conservation of mass–energy and momentum, the angle between the two annihiliation

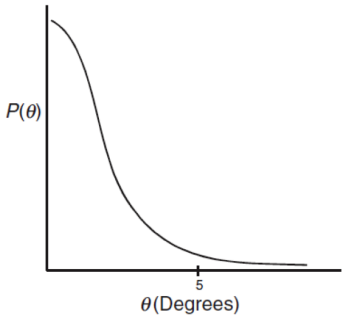

(a) The form of the angular distribution for multiple scattering of positrons in water.

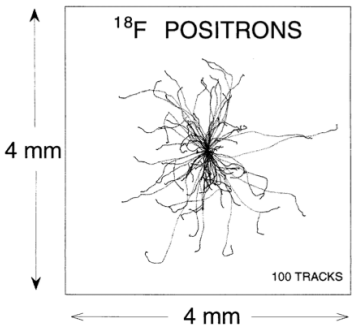

(b) The result of a Monte Carlo simulation of the trajectories of 100 positrons emitted from an ^{18}F point source.

Figure 3.6.: ^{18}F positrons' deflection angles and trajectories. In 3.6(b) note the multiple angular deflections in some trajectories that lead to a much higher total deflection than the probability distribution in 3.6(a) would allow. 3.6(a) ***Copyright notice:*** *Reprinted from [Levi 04], with permission from Elsevier.* 3.6(b) ***Copyright notice:*** *Reprinted from [Levi 99], courtesy of Craig S. Levin. © Institute of Physics and Engineering in Medicine. Published on behalf of IPEM by IOP Publishing Ltd. All rights reserved.*

Elastic collisions, on the other hand, lead to an angular deflection from the incident direction of the positron. The probability for a small angular deflection (much less than $5\ °$) is pronouncedly higher than for one with a large angular deflection (see figure 3.6(a)). Nevertheless many such collisions have a cascading effect of a higher total angular deflection. This is visually illustrated in figure 3.6(b). This figure also visually illustrates that the radial range of ^{18}F positrons is below $2\ mm$ in water. Cho *et al.* experimentally determined that the *full width at half maximum (FWHM)* and *full width at one–tenth maximum (FW(1/10)M) positron ranges* of ^{18}F are $1.02\ mm$ and $1.8\ mm$ respectively in water [Cho 75].

3.2.1.2. Interactions of photons

There are three types of interactions photons undergo in matter:

- *Compton scatter*
- *Photoelectric effect*

photons is usually not exactly $180\ °$, but rather $180 \pm 0.23\ °$ [Rick 92].

- *Pair production*

The third one – pair production – is relevant for photons with energies higher than $1,022\ keV$ and is therefore not within the scope of our discussion. In both of the first two, the photon interacts with the atomic electrons. In Compton scattering the photon transfers some of its energy to the electron and experiences angular deflection from its incident direction. Compton scattering occurs when the energy and the momentum of the photon are much larger than the binding energy and momentum of an electron respectively: the photon cannot transfer *all* of its energy to the electron due to the conservation of energy and momentum[12]. The deflection angle that the photon experiences is a function of its incident energy. This is depicted in figure 3.7. The photoelectric effect occurs when a photon transfers *all* its energy to a *bound* electron, thanks to the atom absorbing some of the recoil momentum[13]. In this case the photon disappears and the involved electron is ejected[14] [Levi 04]. The photons of interest to our work have high energy levels ($511\ keV$), which makes it possible for them to penetrate the whole human body with some energy loss or even escape the human body without undergoing any interaction [Hoff 04].

3.2.2. Radiation detection

In this section we briefly talk about how the interactions that radioactive particles undergo in matter are exploited for their detection. Although many different materials are used for detection, we confine our discussion to *scintillation crystals* (or simply *scintillators*), which are employed in our instrumentation[15]. A scintillator is a medium that emits the energy deposited by an interacting particle in the form of light. When an incoming photon interacts with an electron within the lattice of a scintillation crystal, this electron is excited to a higher energy level. In that sense the scintillation crystal can be described as a *wavelength shifter* [Zeng 04]. On de–excitation, the electron releases this energy difference in the form of ultraviolet or visible light (i.e. of much lower energy than the original photon), which can in turn be detected by e.g. a *photomultiplier tube (PMT)*. Scintillators are the most

[12] *Outer shell* electrons are stronger candidates for Compton scattering.
[13] Photoelectric effect is more probable for *inner shell* electrons, as these have higher binding energies than the outer shell electrons.
[14] For a very good animation of these interactions, see [Harr 04].
[15] Details of our system setup will be introduced in chapters 5 and 6.

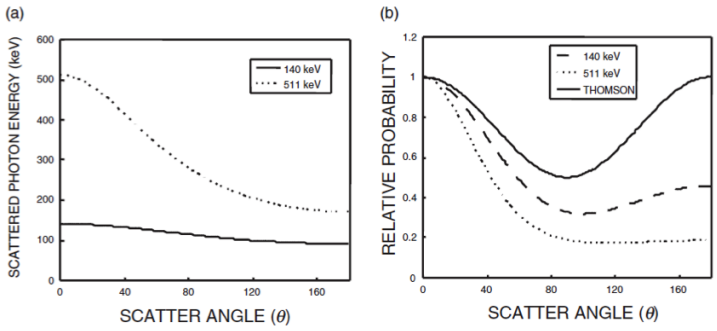

Figure 3.7.: **(a)** The remaining energy of a photon plotted as a function of the deflection angle after Compton scattering. **(b)** The relative probabilities associated with the deflection angle in Compton scattering. The curve for the annihilation photons from e.g. ^{18}F is dashed in each graph. Note that the probability for small deflection angles is significantly higher than larger ones in the case of $511\ keV$, i.e. ^{18}F photons. ***Copyright notice:*** *Reprinted from [Levi 04], with permission from Elsevier.*

commonly used technology in nuclear medicine due to their advantages (for a detailed discussion see [Levi 04]). Commonly used scintillator materials are *NaI(Tl) (sodium iodide)*, $Bi_4Ge_3O_{12}$ *(BGO)*, Lu_2SiO_5*(Ce) (LSO)*. NaI(Tl) is the most commonly used crystal in nuclear medicine [Zeng 04].

The interaction probability (i.e. the detection probability) of a radioactive particle in media like scintillators is characterized by the *effective atomic number* (denoted by Z_{eff} or simply by Z), which is analogous to the atomic number Z of an element $^A_Z G$. Z_{eff} is a numeric value that gives a quantitative scale for the probability of a radioactive particle to interact with that medium and to deposit *all* its energy in that medium. It is by this energy depositing mechanism that radiation is detected. Z_{eff} is calculated using the formula:

$$Z_{eff} = \left(\frac{\sum_i \ w_i \ A_i \ Z_i^4}{\sum_i \ w_i \ A_i} \right)^{(1/4)} \tag{3.7}$$

where A_i and Z_i are respectively the mass number (atomic mass) and atomic number of the i^{th} element of the scintillator, and w_i is that element's material–specific weighting factor, which is the number of atoms of that element within the compound [Wilk 04]. For instance, for NaI(Tl): $w_{Na} = 1$, and $w_I = 1$. The *activator* [Wilk 04], i.e. *Tl (thallium)*, is not counted. Similarly for $Bi_4Ge_3O_{12}$: $w_{Bi} = 4$, $w_{Ge} = 3$, and $w_O = 12$. Usually the detection probability for a photon increases

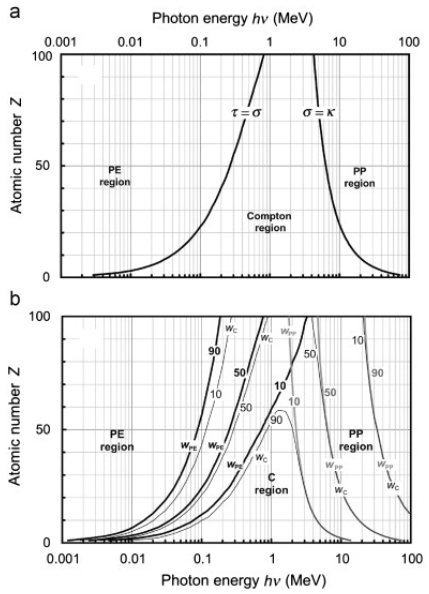

Figure 3.8.: Photon interaction probabilities in relation to detector Z_{eff}. **(a)** Graph showing regions where the photoelectric effect (PE), Compton scatter (C), and pair production (PP) respectively constitute the majority of the interactions that photons undergo in an absorber with different Z (Z_{eff}), plotted in the y–axis. The energy levels of photons are plotted in a logarithmic scale along the x–axis. Note that for the photon energies relevant to this thesis ($0.511\ MeV$ and less), the PP region is of no interest. **(b)** The same graph with contour curves of relative percentages (w_{PE}, w_C and w_{PP}) of the three types of interaction. ***Copyright notice:*** *Reprinted from [Abde 10], with permission from Elsevier.*

with higher Z_{eff}, due to the increase in the probability of the photoelectric effect taking place, i.e. the photon depositing all its energy at once (see figure 3.8). Therefore *inorganic* scintillators like NaI(Tl), which usually have higher Z_{eff}, are preferred for photon detection. For direct positron detection, on the other hand, it is very important that high–energy photons (i.e. annihilation photons) are *not* detected, due to the obvious reason of causing false positives. Therefore *organic* scintillators (e.g. plastic scintillators), which usually have lower Z_{eff}, are preferred for positron detection. This also eliminates the need for a bulky shielding [Hoff 04].

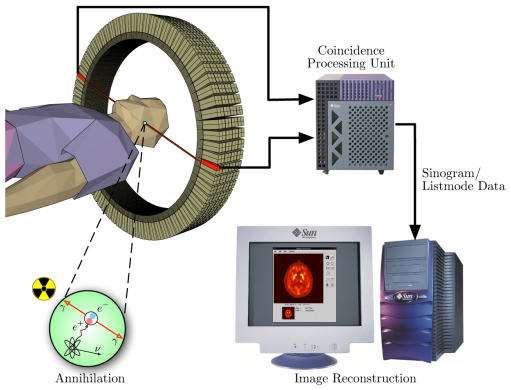

Figure 3.9.: The main components of a PET tomograph. ***Copyright notice:*** *Image courtesy of Jens Langner.*

3.3. Positron Emission Tomography (PET)

HAVING introduced the fundamentals of nuclear physics and how radiation is detected, we focus in this section briefly on the physical and mathematical foundations of *positron emission tomography (PET)*. The PET imaging modality is designed for imaging the radiotracer distribution in the body of a patient by detecting positrons *implicitly* via the detection of the two annihilation photons associated with a positron in two geometrically opposite detectors, in *coincidence*[16]. A PET tomograph consists of detectors arranged in a ring (see figure 3.9). Two events registered simultaneously in a pair of detectors imply that the annihilation has taken place within a thin cylindrical–shaped geometric region defined by the positions of these two detectors, called the *line of response (LOR)* (depicted with the red–colored detectors and a red line in between within figure 3.9). The radiotracer distribution within the *field of view (FOV)* of the PET tomograph is reconstructed by appropriately modeling the detection process. This involves first of all a mathematical representation of the image domain (i.e. the FOV of the tomograph) by some suitable basis function. Secondly a mathematical equation describing the detection of the coincidences is needed. In the third step, this mathematical equation is solved. Although there exist different schemes for these three tasks [Read 07], we confine the mathematical representation of the image domain to uniform voxels; the mathematical equation to a linear system; and the solution procedure to the iterative *maximum likelihood expectation maximization (MLEM)* algorithm.

[16]For a very brief animated narration of how PET works, see [CogN 08].

3.3.1. Mathematical representation of the imaging domain

The image domain is discretized into uniform voxels j, with the (unknown) activity values represented by c_j. Hence the set of activities within the whole domain is represented by $\mathbf{c} = \{c_j\}$. The set of detected coincidence events consists of LORs i, with the actual measured intensity values represented by m_i. The set of these intensity values is then $\mathbf{m} = \{m_i\}$[17]. For each LOR i, the set $\mathbf{a_i} = \{a_{ij}\}$ assigns a weight to each voxel activity c_j, based on the physical effects considered and the geometry of that specific LOR:

$$m_i = \sum_j a_{ij}\, c_j \tag{3.8}$$

In this regard, each a_{ij} can be considered as a probability that an intensity m_i has been measured due to actual positron emission events originating from voxel j, with the detection occurring within the LOR i.

3.3.2. Modeling the detection

The major factors that determine the image quality (and that are to be considered in modeling how the a_{ij}'s are calculated) in PET imaging are the following:

- *Positron range* can be included e.g. by appropriately adjusting the calculating LORs with a positron–range convolution kernel [Read 07].
- *Photon non–colinearity:* although anti–parallel directions are assumed for annihilation photons, the angular uncertainty causes a resolution loss of e.g. $1.3\ mm$ in a PET detector ring with a diameter of $60\ cm$ [Lewe 04].
- *The detector's intrinsic spatial resolution:* this is quantified by the FWHM of the position spectrum obtained for a collimated point source in front of the detector at a fixed distance, called the *point–spread function (PSF)*. For a more detailed discussion, see [Lewe 04].
- *Parallax error* is due to the photons that enter the detector crystals at oblique angles, such that the actual detection happens in a nearby detector. This leads to an inaccurate LOR calculation (see figure 3.11) [Lewe 04].

[17] The intensity value m_i for an LOR i is actually the average of all measurements for that LOR within the entire scan.

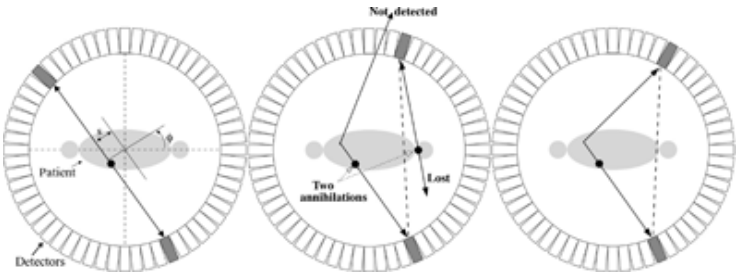

Figure 3.10.: The types of coincidences a PET tomograph accepts. **Left:** *true coincidence*. **Middle:** *random coincidence*. **Right:** *scattered coincidence*. ***Copyright notice:*** *Image reprinted from [Ales 10].*

- *Scattered and random coincidences:* Besides *true coincidences*, a PET tomograph also accepts *false* coincidences resulting from two scattered photons of one annihilation event (technically called *scattered coincidences*). The inability to distinguish between a true and false coincidence leads to wrong LORs. In addition, two simultaneous photons each of which is from a different annihilation event are also accepted. This is called a *random coincidence* (see figure 3.10). Both random and scattered coincidences contribute to a decrease in the PET image resolution [Lewe 04].

- *The uncertainty of the actual annihilation point* within the LOR of a coincidence: this is very commonly referred to as *time–of–flight* information. With proper detector hardware, this uncertainty can be integrated into the PET model by e.g. weighting the a_{ij}'s with an appropriate Gaussian function according to the estimated position of annihilation [Read 07].

In general, PET imaging also suffers from statistics, due to the fact that the number of true event (i.e. coincidence) detections is relatively low, e.g. compared to *X–ray computed tomography (CT)*. PET image quality could theoretically be improved if the number of detected events could be increased by one or more of the following: *i)* increasing the patient dose, *ii)* more efficient scintillators/detectors, *iii)* using a wider portion of the annihilation gamma energy spectrum, *iv)* increasing the solid angle. For a more detailed discussion see [Lewe 04].

Last, but not least, while photons are traveling in the patient's body, some of them get absorbed or scattered such that they do not reach the detector at all. This leads to *attenuation* of a portion of the photons, which could otherwise be useful in improving the image quality (i.e. through improved statistics). Another issue that

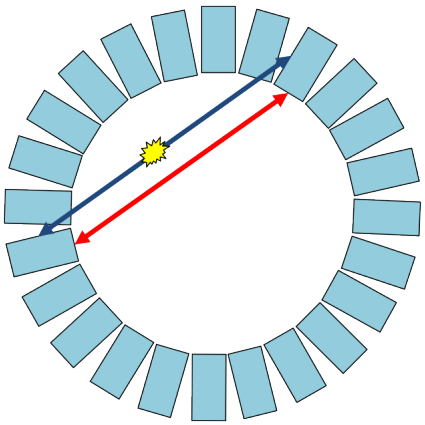

Figure 3.11.: Parallax error in PET coincidence detection: due to an oblique entrance angle, the photon interacts not in the first crystal it traverses, but in the adjacent ones, giving rise to a wrong LOR (red arrow) calculation rather than the correct one (blue arrow).

is introduced by attenuation is that the measured activity (i.e. in the PET image) is actually lower than in reality. Attenuation in this sense is not uniform throughout the body due to the differences in human tissues, and has to be corrected for. Therefore there is need for a map of the patient's body, incorporating the relative attenuations of all voxels within the FOV of a PET tomograph. These are called *attenuation coefficients* and the process accounting for these inhomogeneities *attenuation correction*. In practice, it is very common to acquire a (mostly) low–dose, non–diagnostic resolution CT scan of the patient together with the PET acquisition. CT provides a natural means of attenuation correction (albeit not at the same energy level: compare the $511\ keV$ annihilation gammas of PET to the $80\ keV$ X–rays in CT [Wats 04]), as it images the attenuation of ionizing radiation in different tissues of the body.

After decomposing each LOR based on equation 3.8, all the LORs can in this fashion be stacked into a linear system:

$$\mathbf{Ac} = \mathbf{m} \tag{3.9}$$

where $\mathbf{A} = \{\mathbf{a_i}\}$ is the *system matrix*; $\mathbf{c} = \{c_j\}$ are the (unknown) activity values within the voxels; and $\mathbf{m} = \{m_i\}$ are the measured coincidence counts. Such a modeling scheme allows for a flexible integration of the complex physics behind positron emission [Read 07].

3.3.3. Solving the linear system (reconstruction)

Maximum likelihood expectation maximization (MLEM) is an iterative approach based on a statistical model of the underlying process of acquiring data. As such, MLEM is very suitable for modeling the detection of radiation, which obeys the *Poisson distribution* [Lalu 04]. MLEM models each measurement m_i as the realization of a *Poisson variable* $\mathbf{Q_i}$ with the *mean (expected) value* q_i. The *maximum likelihood (ML)* part of MLEM seeks to maximize – for each measurement i – the conditional probability $Pr\left(m_i|q_i\right)$ that the measurement value of m_i is obtained, assuming a mean value of q_i:

$$Pr\left(m_i|q_i\right) = \frac{\left(q_i\right)^{m_i}\ exp\left(-q_i\right)}{m_i!} \tag{3.10}$$

The *expectation maximization (EM)* part of MLEM starts from an initial guess c_j^0 of the activity values c_j, and performs iterations of the form:

$$c_j^{k+1} \ = \ c_j^k \ + \ \lambda^k \ \frac{\partial O\left(\mathbf{c}^k\right)}{\partial c_j^k} \tag{3.11}$$

where k is the iteration number, and O represents the objective function to optimize. So the whole second term with the partial derivative of O is the update to be applied on the current c_j value c_j^k. λ^k is the step size (or the weighting factor of the update to be applied), commonly chosen such that the whole iteration scheme translates to:

$$c_j^{k+1} \ = \ \frac{c_j^k}{\sum_{i=1}^{I}\ a_{ij}} \ \sum_{i=1}^{I}\left[a_{ij}\ \frac{m_i}{q_i^k}\right] \tag{3.12}$$

For the full derivation of this scheme, as well as a very detailed discussion of other algorithms used in reconstruction, see [Read 07].

3.3.4. Visualization

Generated PET images have very valuable information for localizing malignancies. Nonetheless, due to the resolution limitations, the images are usually blurry, and might have artifacts. There is hence often the need for co–registered anatomic information in order to correctly interpret a PET image. In practice, as we mentioned earlier, mostly at least a low–dose, co–registered CT image accompanies a PET image. It is very common to overlay the PET image on to the CT image by

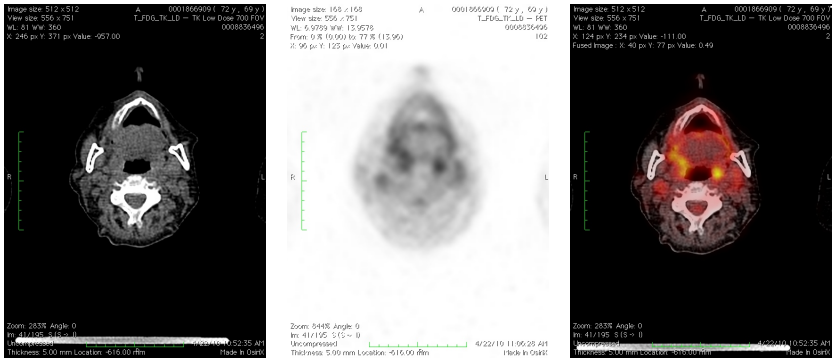

(a) CT (b) PET (c) PET/CT overlay.

Figure 3.12.: Visualization of a PET, a co–registered CT, and an overlaid PET/CT image. Transverse slice from a PET/CT scan of a patient with head and neck cancer. Note that the individual modalities are represented as gray–scale images, while in the fused image a different colormap is used for PET data. Data courtesy of the Nuclear Medicine Department, Klinikum rechts der Isar, Technische Universität München.

alpha–blending, using a variant of the following equation:

$$\chi_\alpha \;=\; \alpha\, \chi_{warm}\left(I_{PET}\right) \;+\; (1-\alpha)\; \chi_{gray}\left(I_{CT}\right) \tag{3.13}$$

where χ_α represents the final image intensities and colors obtained by fusing:

- the PET image intensities I_{PET} transformed into the color–space using the colormap χ_{warm}
- the CT image intensities I_{CT} transformed into the color–space using the colormap χ_{gray}

The fusing is done with a weighting factor α that dictates how much of each of the two images is visible in the image. The rationale behind using the different colormap functions (gray–scale χ_{gray} for CT, and a warm–color–based colormap χ_{warm} for PET) in the overlaid PET/CT image is to avoid confusion [Wats 04]. An example can be seen in figure 3.12.

CHAPTER 4

Intra-operative Imaging Devices & Technologies

POSITRON emission tomography (PET) has gained widespread popularity especially in the last decades in many different clinical and pre–clinical fields of medical imaging. Nevertheless the bulky equipment needed for PET and the long data acquisition times make it of limited use intra–operatively. This is why people started coming up with novel devices and technologies that allow for making use of positron–emitting radiotracers in intra–operative settings. In this chapter we turn our attention to these. Our literature review has revealed very interesting research papers and patents on novel devices. In the first section, we give an overview of devices and technologies by which direct *detection* and *imaging* of positrons is possible. In the second section, we focus on devices and technologies for intra–operatively detecting annihilation gammas from positron–emitters and later on intra–operative PET systems.

4.1. Direct Positron Detection & Imaging

TO the best of our knowledge, we as the Chair for Computer Aided Medical Procedures (CAMP) are the only research group world–wide that conducts research on using beta probes in a navigated setup towards intra–operative imaging. The state–of–the–art research on direct positron detection and potential applications is centered on developing off–the–shelf beta probes and *beta cameras* (i.e.

(a) Probe circuitry.

(b) Probe handle.

(c) Complete probe system.

Figure 4.1.: The intra–operative beta probe system designed and developed by the Center for Advanced Imaging at West Virginia University at Morgantown. ***Copyright notice:*** *All images courtesy of the Center for Advanced Imaging at West Virginia University in Morgantown, West Virginia, USA.*

planar detectors that provide 2D images instead of a 1D signal, with high annihilation photon rejection capability). In the following two subsections we elaborate on the state–of–the–art of these two types of detectors respectively.

4.1.1. Intra–operative Beta Probes

The first beta probe we would like to mention here is the one that we use in our research. The paper describing this beta probe was published about 20 years ago [Dagh 94]. The innovation in this probe is the use of a ring detector in order to account for the contamination with the annihilation gammas, thereby giving a net count of betas detected (we provide detailed information on the construction of the probe in section 5.2.1.1). It is interesting to note that the literature on small radiation detectors suitable for intra–operative use started emerging in the early 80s. The reader will find a lot of those early references in the above mentioned paper of Daghighian *et al.* In this same paper the authors also report the performance of the probe in two phantom studies: a simplified brain phantom and an abdominal cavity phantom. Another very interesting study involving this beta probe (and

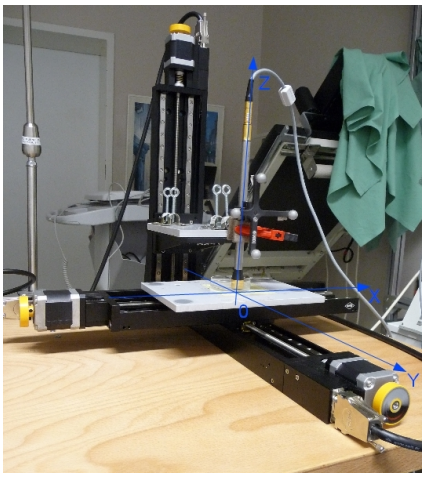

Figure 4.2.: Intra–operative beta probe produced by Silicon Instruments GmbH (now First Sensor AG), Berlin, Germany, mounted on the step–motor.

also our high–energy probe described in section 6.2.1.1) was conducted on animal models of some selected types of malignancies including HNSCC. In this study the authors primarily focused on the correlation between the beta probe readings and the high–energy probe readings. Their measurements in vivo, ex vivo, as well as in vitro showed a high correlation between the readings of both types of probe. Not unexpectedly, they report that the beta probe may be more sensitive than the high–energy probe, due to the fact that the former could identify smaller tumor sites compared to the latter [Stro 09].

Another interesting intra–operative probe is the one reported by Raylman in [Rayl 01]. Figure 4.1 shows images of this intra–operative probe system. This probe can be operated in two modes: beta–optimized and photon–optimized. As such it can be utilized for detecting positrons as well as annihilation photons of e.g. ^{18}F. In his paper, the author after giving a detailed description of the probe presents his studies for determining the sensitivity of the probe as well as the *selectivity*, or the ability to distinguish beta particles from gamma rays. Wherever applicable, the measurements are repeated for three radionuclides: ^{18}F (positron emitter), ^{99m}Tc (pure gamma emitter) and ^{111}In (decays by emitting gammas after *electron capture*[1]). Raylman *et al.* have also been working on an endoscopic version of their beta probe, details of which can be seen in [Nucl 08] under the keyword

[1]The *electron capture* decay mode is not the scope of this thesis. However we would like to refer the interested reader to [Levi 04] for the details of this type of radioactive decay.

"Endo Probe".

A very interesting intra–operative study was conducted by Piert *et al.* and reported in [Pier 07]. In their study the group used the beta probes manufactured by Silicon Instruments GmbH (now First Sensor AG), Berlin, Germany, which the author of this thesis had also used in the research work during his Master's thesis [Ozgu 09a] (see figure 4.2) [2]. In this study, Piert *et al.* included 17 patients with different types of histologically proven malignancies. In concrete terms, they elaborate on the correlation between the radioactivity values they calculated from the [^{18}F]FDG–PET images of the patients and the intra–operative findings with the probes. In addition they report their findings on the technical parameters of the probes like sensitivity, linearity, and resolution. Last but not least they prepared a phantom simulating small superficial tumor masses, similar to the one presented in [Dagh 94], and looked at the performance of the probe in terms of detecting these.

Bogalhas *et al.* published an article on a positron probe developed for intra–operative use in neurosurgery [Boga 09]. This article gives a detailed overview of the construction of this probe (see [TRIO 09] for an image of the probe). In addition it presents the evaluation of various technical probe parameters and a phantom study featuring a simplistic brain phantom simulating a very small post–excision residual tumor mass in the surgical cavity. In this study the authors also varied the size of this residual tumor and the tumor–to–background (T/B) ratio according to values reported for three radiopharmaceuticals used for imaging brain tumors in literature; namely [^{18}F]FDG, [^{18}F]FET, and [^{18}F]Fluoro–[1,2–2H4]choline. We would like to point out here that the reader will also find a review of existing image–guided neurosurgery systems in the introduction of the article by Bogalhas *et al.* [Boga 09].

4.1.2. Intra–operative Beta Cameras

In our literature review pertaining to beta cameras, we came across an article from 1995 about the development of hand–held imaging probe. The beta camera design that is presented in this paper is aimed at having a $1 - 2\ cm^2$ sensitive area with intrinsic spatial resolution on the order of $1\ mm$. The authors talk about utilizing this imaging device in neurosurgery for determining the cleanliness of resection

[2] The author has two different names, and he published his Master's thesis with his other name *Coşkun Özgür*.

Figure 4.3.: MARGINator beta camera by IntraMedical Imaging LLC, Los Angeles, CA, USA. ***Copyright notice:*** *Image courtesy of Dr. Farhad Daghighian, reprinted from [MARG 13].*

borders, which is exactly the medical application of focus in this thesis. In this article the authors illustrate the design of the beta camera and present a very detailed analysis of its various technical parameters [MacD 95].

A very recent beta camera has been developed by the manufacturer of our beta probe, namely IntraMedical Imaging LLC, Los Angeles, CA, USA. This beta camera, depicted in figure 4.3, produces a color image and has a sensitive area of $15 \times 15\ mm^2$. The manufacturer reports that with a one–minute acquisition time the probe is able to detect $4\ mg$ of tumor, and $2\ mm$ spatial resolution. A video featuring a demo of the device is available in [MARG 13]. Although quite innovative, we believe that this device is still too bulky for intra–operative use especially in a navigated setup: the large detector head makes it virtually impossible to freely move the device within the resection cavity.

A *fingertip beta imager* was presented by Stolin *et al.* in 2010 [Stol 10]. This is a finger–size planar imager that can be attached to the finger of the surgeon and due to its small size can be moved quite freely within the resection cavity. The authors report a $10 \times 10\ mm^2$ sensitive area and $2.5\ mm$ intrinsic spatial resolution. This novel device can be seen in figure 4.4, alongside with images obtained from phantoms. The first medical application targeted with this very innovative device is breast cancer excision (*lumpectomy*). We believe that although not used as such, this device is a very good candidate for use in a *navigated* radio–guided surgery setup. The same research group is also working on positron detectors tailored towards different aspects of research on plant biology using ^{11}C–labeled carbondioxide. See for instance [Stol 09] and [Weis 10].

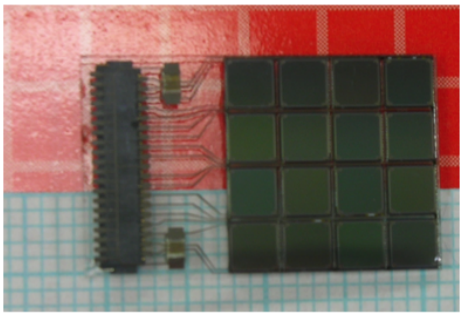

(a) Internal 4×4 detector structure.

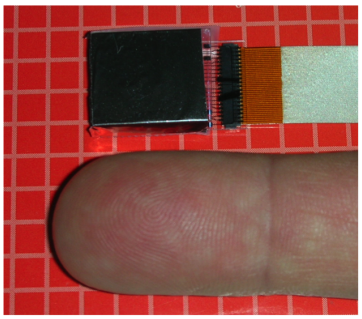

(b) Imager compared to a finger.

(c) Bead phantom (each bead with $150\ nCi$ of ^{18}F).

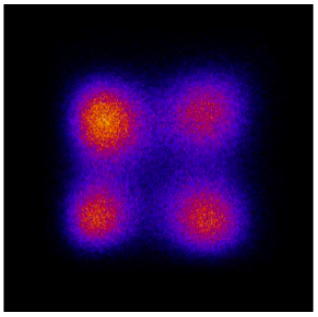

(d) Image of bead phantom.

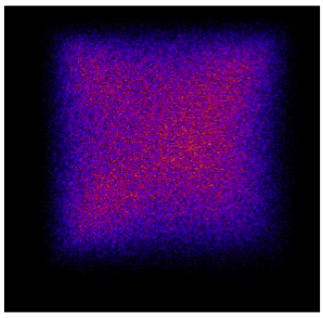

(e) Image of a planar radioactive source flooding the whole sensitive area of imager.

Figure 4.4.: Fingertip imager developed by the Center for Advanced Imaging at West Virginia University at Morgantown, and images obtained with it. ***Copyright notice:*** *All images courtesy of Center for Advanced Imaging, West Virginia University.*

Another research group that is working on the development of a beta camera is the research team of Radiation Monitoring Devices, Inc., (RMD), Watertown, MA, USA. Their imaging device has a $8 \times 8\ mm^2$ imaging area (see figure 4.5), which thanks to *fiber optic tapers* can be increased four– and nine–fold (to $16.4 \times 16.4\ mm^2$ and $24.6 \times 24.6\ mm^2$ respectively). In their same paper, Thacker *et al.* present the construction of the probe, as well as their calibration experiments [Thac 08]. The group conducted an interesting set of experiments with a ^{90}Sr point source[3] and several layers of chicken skin in order to quantify the attenuation of beta particles in tissue. In addition they show images of a *murine* (i.e. grown in mice) tumor model with [^{18}F]FDG. The same group also conducted an in vivo study of their beta camera on a lingual cancer model in rabbits [Sing 09]. In that paper they report that their device is capable of detecting very low activity in tumors. In addition they report low sensitivity to background gamma radiation [Thac 08]. Two earlier papers about this beta camera present the evaluation of the device using standard clinical phantoms, and based on the operational data obtained on swine models and in surgery [Shes 06, Shes 07]. Their most recent paper presents the capabilities of the device on an animal model [Sing 13].

Lauria *et al.* have developed an intra–operative beta camera based on a silicon pixel detector with a sensitive area of $14.08 \times 14.08\ mm^2$ [Laur 07]. The camera is depicted and illustrated in figure 4.6. The authors conducted experiments with an [^{18}F]FDG droplet for determining several calibration parameters. Among others, they report counting linearity in the activity range $37\ Bq$ – $37\ kBq$. This beta camera, however, is not capable of distinguishing annihilation photons from beta particles. Russo *et al.* provide an extended analysis of the technical parameters of the same beta camera, as well as an overview of the camera's performance using biological samples [Russ 08].

Last but not least, Vu *et al.* reported on a silicon semiconductor–based beta camera with a $14 \times 14\ mm^2$ active imaging area [Vu 06, Vu 11]. The latter presents in detail the construction of the beta camera. The authors mention that the detector is primarily sensitive to charged particles, making it highly capable of rejecting the background gamma radiation. In addition, they use the beta camera for imaging colonies of four melanoma cell lines, the colonies featuring cell populations from hundreds of cells down to a single cell.

[3] ^{90}Sr is an electron–emitter with $546\ keV$ maximum energy (compare to $633.5\ keV$ maximum energy of ^{18}F).

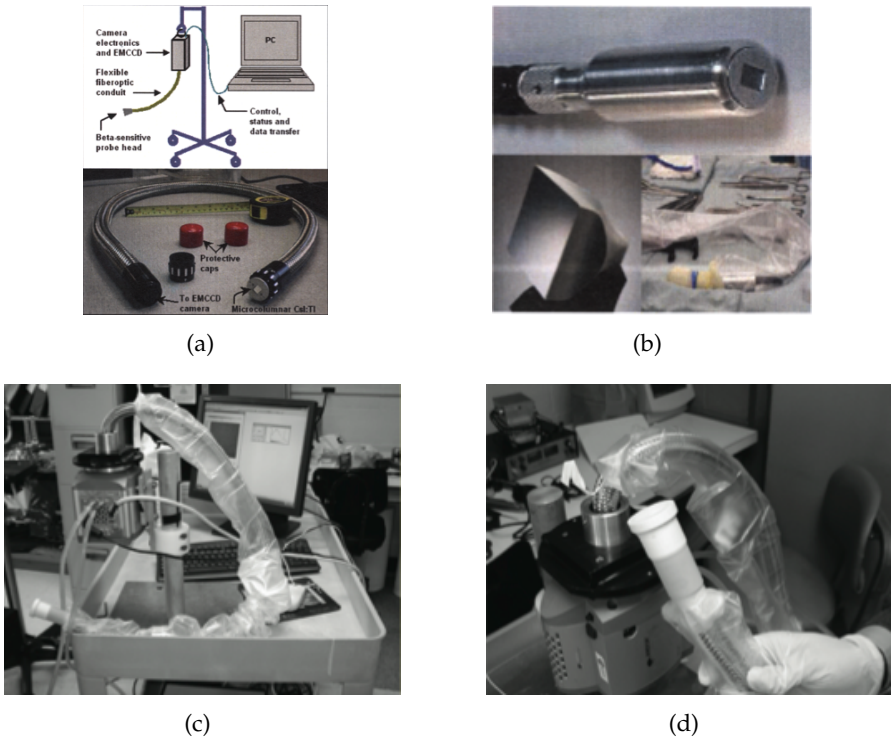

(a) (b)

(c) (d)

Figure 4.5.: RMD intra–operative imaging beta probe. ***Copyright notice:*** *4.5(a) and 4.5(b) reprinted from [Thac 08], © 2008 IEEE. 4.5(c) and 4.5(d) reprinted from [Sing 09], © 2009 IEEE.*

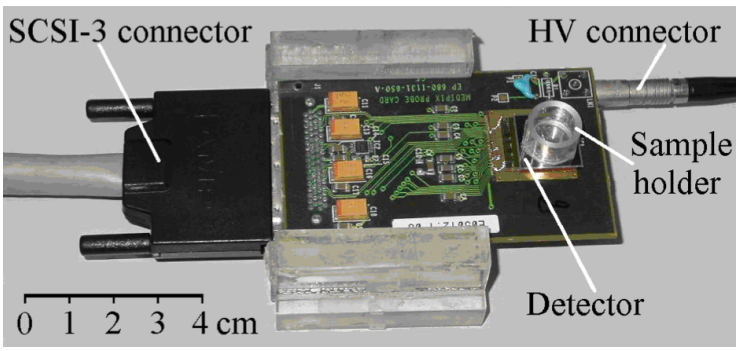

Figure 4.6.: The silicon pixel detector–based intra–operative beta camera developed by Lauria *et al.* ***Copyright notice:*** *Image courtesy of Prof. Dr. Adele Lauria, reprinted from [Laur].*

4.2. High–energy Gamma Detection & Imaging

RESEARCH groups that work on intra–operative PET–like imaging modalities in general use (high–energy) gamma cameras, and not probes. Nonetheless, we find it useful to first outline in the next subsection some papers on high–energy probes in intra–operative settings. Following that we give an overview of the intra–operative and diagnostic–oriented novel PET–like imaging approaches respectively in the two subsequent subsections.

4.2.1. Intra–operative High–energy Probes

The paper by Raylman already mentioned above talks about the utility of an intra–operative probe (see figure 4.1) that can be operated in two modes: beta–optimized and photon–optimized [Rayl 01]. As such, this probe is capable of detecting both the positrons and the annihilation gammas of ^{18}F. In the paper the author reports on the gamma detection sensitivity of the probe in conjunction with three radionuclides: ^{18}F (positron emitter), ^{99m}Tc (pure gamma emitter) and ^{111}In (decays by emitting gammas after electron capture – see the footnote in section 4.1.1). ^{111}In yielded the highest gamma detection sensitivity, and ^{99m}Tc the lowest.

Next we would like to elaborate on the use cases of our high–energy probe in literature, as it is quite rich. The paper by Strong *et al.* (mentioned in detail above) reports on the utilization of this probe for localizing malignancies in murine tumor models; however with a focus on the validation of the beta probe [Stro 09]. On the other hand a recent study was performed by Gulec *et al.* featuring 40 patients [Gule 06]. In this study the probe detected all the [^{18}F]FDG–PET–positive lesions. In 14 patients it guided the surgeon in finding lesions that were not detected by surgical exploration. In eight cases, it localized a non–palpable lesion. Moreover in two patients, it localized an additional lesion not seen on the pre–operative images. In another study featuring 12 patients, Kim *et al.* studied the intra–operative performance of the high–energy probe in conjunction with [^{18}F]FDG in malignancies related to the head and neck anatomy [Kim 11]. The probe was used two to six hours post–injection and the malignancy site was re–explored if the T/B signal ratio was more than 1.3. This somehow lower ratio suggests that the T/B contrast in this anatomy is inherently limited, due probably to the high unspecific uptake of [^{18}F]FDG. The authors report that the probe

could localize all the tumors with a mean T/B ratio of 1.51, and all the T/B ratios falling in the range 1.17 – 4.03. In addition, using the probe, the authors could detect additional lymph nodes that were not identified during the pre–operative US inspection.

Essner *et al.* studied the performance of a high–energy probe in a study featuring eight patients (six melanoma and two colon carcinoma) who had a total of 17 tumors identified in pre–operative [^{18}F]FDG–PET images [Essn 01]. The authors intra–operatively recorded the probe readings on the tumors and peri–tumoral healthy tissue. The tumors yielded T/B ratios between 1.16 – 7.92. 11 of the 17 tumors yielded a T/B ratio higher than 1.5. The authors report that sub–optimal T/B ratios occured as a result of the surgery being performed earlier than $30\ min$ or later than $60\ min$ post–injection.

Gulec *et al.* report a study for quantifying the performance of another high–energy probe, featuring 24 patients [Gule 07]. They recorded T/B ratios based on probe count rates, and the lesion detection success intra–operatively, two to six hours post–injection of [^{18}F]FDG. The probe could detect all lesions with a T/B ratio of 1.5 or more. In addition it was useful in localizing non–obvious lesions in eight patients. Last but not least, the probe was useful in identifying non–palpable lesions.

A very interesting study targeting biopsy–proven head and neck cancer malignancies in 36 patients was published by Meller *et al.* in [Mell 06]. This group developed their own gamma probe (see figure 4.7), whose details they outline in their mentioned paper. 21 of these 36 patients showed lymphatic metastases, while the remaining 15 did not. The authors compared the performance of the probe in conjunction with [^{18}F]FDG to the pre–operative US and pre–operative [^{18}F]FDG–PET inspections. The probe and the US inspections both yielded the highest sensitivity of 95 %. Specificity was highest for [^{18}F]FDG–PET with 80 %, while the probe yielded 60 % and US 40 %. The authors further argue that the sensitivity for the probe investigations could be increased by using different cut–off criteria, however this would then adversely affect the specificity. [^{18}F]FDG–PET and gamma probe performance were comparable in terms of accuracy: 83 % and 81 % respectively.

In a Technical Innovations report, Povoski *et al.* explain a combined approach featuring pre–operative [^{18}F]FDG–PET/CT, intra–operative high–energy probe, and intra–operative US inspections for localizing tumors and verifying the resection in a case of melanoma [Povo 08]. In the study they report the probe had

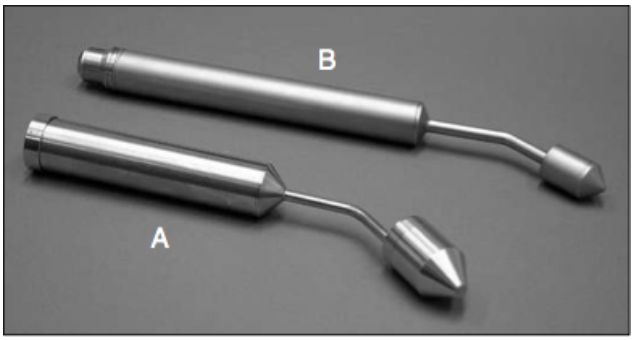

Figure 4.7.: Positron emission probe developed by Meller *et al.* **A** depicts an early prototype, whereas **B** is the actual version used in the study reported in [Mell 06]. ***Copyright notice:*** *Image reprinted from [Mell 06] with permission from Schattauer GmbH.*

the role of localizing post–resection residuals within the tumor bed. After this initial investigation, the resection was extended and another consequent probe inspection was performed, this time showing no residual. In addition, the probe was used for guiding the surgeon to sites of increased activity as seen in the pre–operative [^{18}F]FDG–PET/CT images. Another paper by Hall (the second author of the above report) *et al.* outlines their combined approach featuring pre–operative [^{18}F]FDG–PET/CT and intra–operative high–energy probe (i.e. *no* US this time) inspection for localizing tumors and verifying complete resection in breast cancer [Hall 07]. In their study featuring two patients, they used the probe in a similar manner the above report. Povoski *et al.* also published a review on the spectrum of medical application scenarios using gamma probes [Povo 09].

4.2.2. Intra–operative PET Systems

The Center for Advanced Imaging at the West Virginia University is actively conducting research on hardware pertaining to intra–operative PET imaging. The group presented their work on hand–held PET imagers tailored especially towards breast imaging at the IEEE Medical Imaging Conference (MIC) 2011 [Stol 11]. They have various imaging and non–imaging components, some of which can be operated in coincidence mode (see figure 4.8 for images of the components). Their system allows for the detection of coincidences and hence for PET image reconstruction in the OR. Stolin *et al.* also developed a dual modality planar PET/optical scanner for confirming resection margins based on the ex vivo analysis of *extracted*

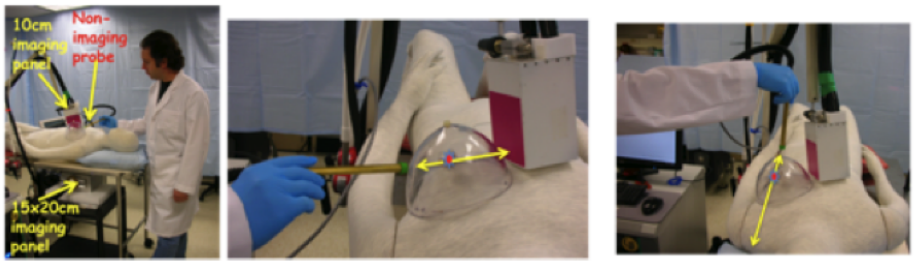

(a) Smaller imaging panel and non–imaging high–energy gamma probe (all images), in combination with larger imaging panel underneath the bed (left image only).

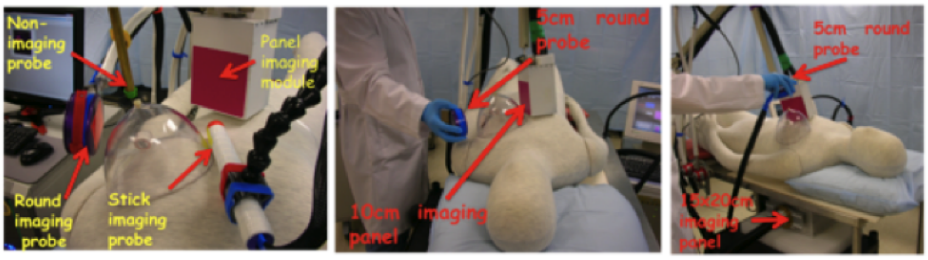

(b) Smaller imaging panel and round imaging probe (all images), and stick imaging probe (left image only).

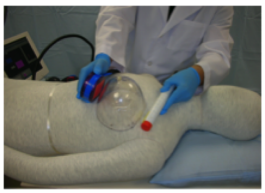

(c) Round imaging probe operated in coincidence with stick imaging probe.

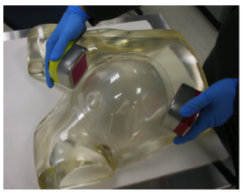

(d) Two round imaging probes operated in coincidence.

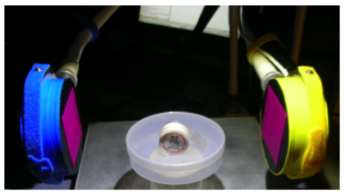

(e) Another version of the two round imaging probes.

Figure 4.8.: Hand–held imaging and non–imaging detectors developed by the Center for Advanced Imaging at West Virginia University at Morgantown. ***Copyright notice:*** *All images courtesy of the Center for Advanced Imaging at West Virginia University in Morgantown, West Virginia, USA.*

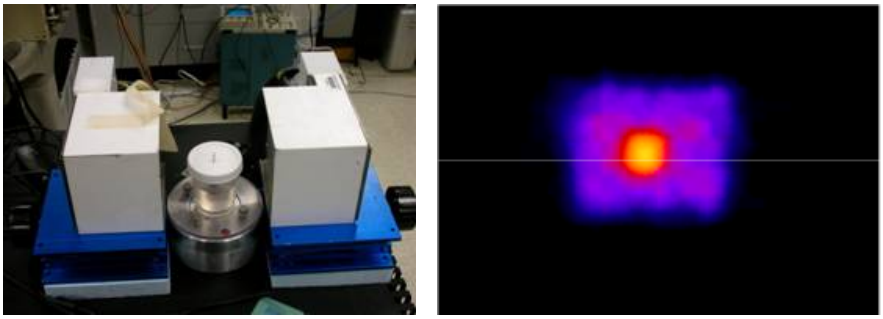

(a) The construction of the system. (b) An image generated by the imager.

Figure 4.9.: The tissue specimen imager developed by the Center for Advanced Imaging at West Virginia University at Morgantown. ***Copyright notice:*** *Both images courtesy of the Center for Advanced Imaging at West Virginia University in Morgantown, West Virginia, USA.*

tissue samples [Stol 08]. This system combines a pair of detector heads for PET imaging and an optical camera for overlaying nuclear information on to the tissue sample, which serves as an anatomical map for orientation. Images of this planar PET/optical scanner can be seen in figure 4.9. This system has recently been patented [Fale 12]. Details can be seen in the patent publication.

Huh *et al.* published very interesting research work featuring a Monte Carlo simulation of an intra–operative PET imaging probe system they were planning to build [Huh 07]. Their concept is similar to the hand–held PET imagers by Stolin *et al.* outlined above. This research group also conducts research on fast reconstruction algorithms that will enable PET reconstruction within a timeframe suitable for intra–operative use. They presented one such method in [Huh 08]. The following year they reported that their method can reconstruct 3D images from simulated data in just 70 $msec$, thanks to their implementation on a GPU [Huh 09].

Weinberg *et al.* presented a method for 3D imaging by using hand–held 2D gamma cameras [Wein 01]. The group also built their own portable gamma cameras. In 2003, Adler (the senior author of the mentioned publication) *et al.* filed a patent application for their technology [Adle 03].

4.2.3. Diagnostic–oriented Novel PET Systems

Another research project of the Center for Advanced Imaging at the West Virginia University in Morgantown is the high–resolution PET prostate imager. The system

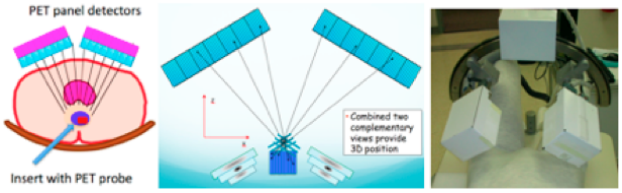

(a) The conceptual illustrations (left and middle) and the actual image of the imager.

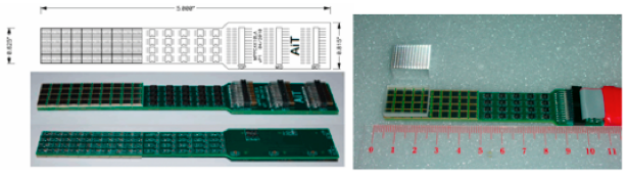

(b) The circuitry of the insertible trans–rectal detector probe.

Figure 4.10.: The dedicated PET prostate imager system developed by the Center for Advanced Imaging at West Virginia University at Morgantown, West Virginia, USA. ***Copyright notice:*** *Both images reprinted from [Maje 11a], © 2011 IEEE.*

consists of two 2D detector blocks placed e.g. close to the patient's torso and a spatially co–registered, insertible trans–rectal detector probe (see figure 4.10). As such it provides coincidence detection and very high resolution reconstruction of the prostate as well as the surrounding organs. A patent application for this invention has recently been filed by the group [Maje 10b]. There are also two papers [Maje 11b, Maje 11a] and a technical report [Maje 10a] about this system.

Another and very recent publication of Stolin, Majewski *et al.* is on a novel tandem PET imaging system [Stol 13]. This is a high–resolution PET imager. See figure 4.11, which shows the system along with images obtained with it, capable of down to $1\ mm$–resolution.

Similar to the work of Majewski *et al.* cited above is the ongoing European Union project "ENDOTOFPET–US" [The 13b]. This is a huge research project undertaken by 12 Europe–wide partners. According to the project website: *"The main clinical objective is to address image–guided diagnosis and minimally invasive surgery with a miniaturized bimodal endoscopic probe with a millimetre spatial resolution and a 100 times higher sensitivity than whole–body PET scanners. The aim is to improve harvesting of tumoural tissue during biopsy by combining the functional biological information of radioactive biomarkers with the morphological information obtained from US."*

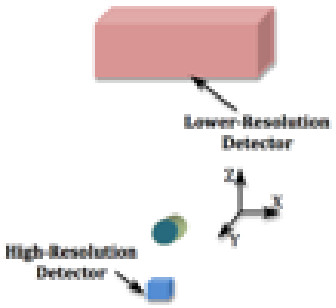

(a) Illustration of the system.

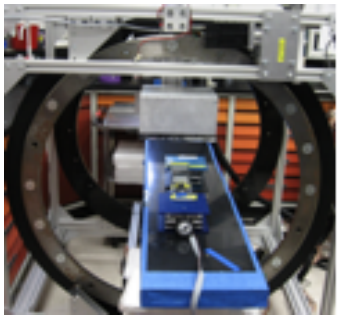

(b) Constructed tandem PET imager prototype.

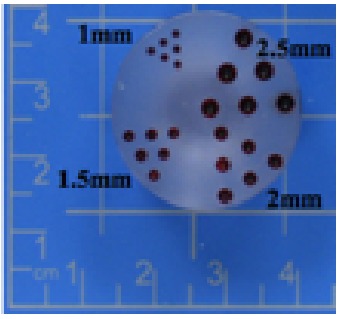

(c) Resolution phantom.

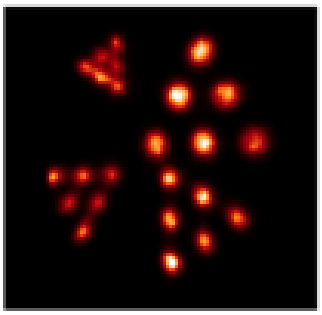

(d) Image of the resolution phantom to the left.

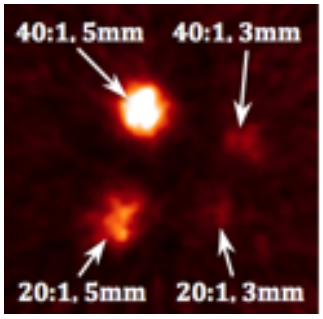

(e) Image of another resolution phantom.

Figure 4.11.: High–resolution tandem PET imager developed by the Center for Advanced Imaging at West Virginia University at Morgantown, along with phantom images. ***Copyright notice:*** *All images courtesy of the Center for Advanced Imaging at West Virginia University in Morgantown, West Virginia, USA.*

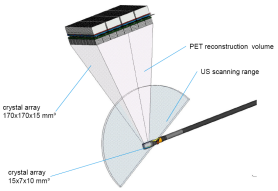

(a) System construction.

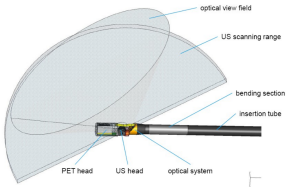

(b) Illustration of PET vs. US field–of–view.

(c) PET–US probe.

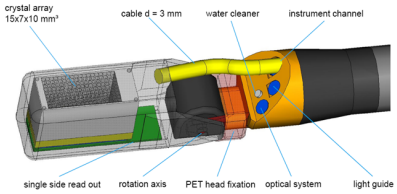

(d) Details of PET–US probe.

Figure 4.12.: ENDOTOFPET–US system construction and components. ***Copyright notice:*** *(All images) Copyright: Gadow/DESY.*

The project primarily focuses on pancreatic cancer and prostatic cancer, due to the fact that both pathologies follow almost asymptomatic development [The 13b]. Various illustrations and an image of the PET–US probe can be seen in figure 4.12.

Turkington *et al.* published a phantom study on the performance of a prostate PET imaging system with dual planar detectors [Turk 04]. The phantom featured different size spheres and all the spheres were filled with 20:1, 10:1 and 5:1 activity concentrations with respect to the background, in three different settings (figure 4.13 shows an image of this phantom as well as the detectors used). The group obtained the data with the detectors **i)** in a fixed orientation, **ii)** orbiting around the body in limited and **iii)** in full arcs. They were able to reconstruct the spheres at 20:1 and 10:1 activity concentrations.

Another, though loosely–related, research work belongs to Judy *et al.* , and is about using a two–head gamma camera system for improving resolution in breast scintigraphy [Judy 07]. The group evaluated a commercially available, as well as a research–based system with a phantom, in order to quantify the resolution as a function of lesion depth. In a more recent publication, Judy *et al.* also provided an analysis of several methods for combining the data from the two gamma cameras into one image [Judy 10]. This research work was conducted in cooperation with Majewski and Stolin.

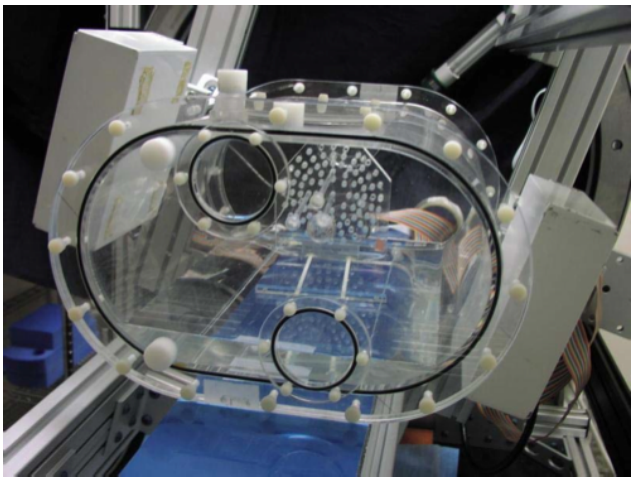

Figure 4.13.: PET prostate imager developed by Turkington *et al.* together with the phantom they used for their study. ***Copyright notice:*** *Image reprinted from [Turk 04], © 2004 IEEE.*

Part II.

Contributions of Our Research Work

CHAPTER 5

Intra–operative Epiphanography

THE intra–operative beta probes presented in section 4.1.1 obviously do not provide images. The beta cameras presented in section 4.1.2 close this gap as they do provide 2D images, albeit of a region limited by the sensitive area of the camera. Nevertheless, in many intra–operative scenarios there is a need for *navigational information*; that is, the surgeon needs to know *which part* of e.g. the tumor bed has a higher radiotracer uptake, in order to make the decision of extending the resection borders in that part. In this chapter we introduce our approach to meeting this need, namely the *epiphanography* imaging modality for intra–operative use. The word *epiphanography* is a compound of the Greek words επιφάνεια (*epiphaneia*) for *surface* and ζωγραφιά (*ographia*) for *image*, and hence means *the image of the surface* similar to the compound τόμος (*tomos*) for *volume/slice* and ζωγραφιά (*ographia*) for *image*, meaning *the image of the volume*, i.e. *tomography*. To our knowledge this is the first use of the word *epiphanography* in the context of nuclear medical imaging.

We first present the relevance of epiphanography in the neurosurgical context. Then we talk about the general design and calibration of our system. Following that we elaborate on the experiments for evaluating various parameters of the system. Finally we present our feasibility studies with phantoms and conclude with a discussion of our results.

Acknowledgements and publications

Spatial resolution study in section 5.3: in collaboration with Prof. Dr. Pierre Jannin[7], and Frédéric Monge[7]; under medical supervision of Dr. Florence Le Jeune[8]; supported by the DAAD PROCOPE.

Biological feasibility study in section 5.4: in collaboration with Sabine Pirsig[3], Jakub Bieniarz[2], and Dr. Thomas Wendler[5]; published in [Shak 10a].

Ad-hoc detection models in section 5.5: in collaboration with Alexander Hartl[1,2,3], Florian R. Schneider[3,6], and Dr. Jožef Pulko[3,6]; published in [Shak 10b, Shak 11a, Shak 12a]. Probe specifications courtesy of Dr. Farhad Daghighian.

Neurosurgical phantom studies in section 5.6: under medical supervision of Prof. Dr. Alexander Drzezga[3], Dr. Florence Le Jeune[8], Prof. Dr. Xavier Morandi[9], Dr. Sylma Diabira[9], Dr. Laurent Riffaud[9]; in collaboration with Prof. Dr. Pierre Jannin[7], Dr. Maximilian Baust[2], Frédéric Monge[7], and Aslı Okur[2,3]; supported by the DAAD PROCOPE; first study published in [Shak 11b].

All publications: under the scientific supervision of Dr. Tobias Lasser[2,4], supported by the SFB 824 (DFG, Germany), the Graduate School of Information Science in Health (GSISH), and the TUM Graduate School (Munich, Germany).

Affiliations

1 Graduate School of Information Science in Health (GSISH), Technische Universität München, Munich, Germany

2 Computer Aided Medical Procedures (CAMP), Technische Universität München, Munich, Germany

3 Department of Nuclear Medicine, Klinikum rechts der Isar, Munich, Germany

4 Institute of Biomathematics and Biometry, HelmholtzZentrum München, Germany

5 SurgicEye GmbH, Munich, Germany

6 Department of Physics (E18), Technische Universität München, Munich, Germany

7 Equipe MediCIS, Université de Rennes 1, Rennes, France

8 Centre E. Marquis, Université de Rennes 1, Rennes, France

9 Department of Neurosurgery, Rennes University Hospital, Rennes, France

5.1. Medical Relevance

LOW–GRADE gliomas (LGG) represent about 30 % of all gliomas. LGGs have an annual prevalence of 1 in 100,000 and affect mostly adults between 20 – 50 years of age [Loui 07]. Most LGG lesions can be resected to some extent [Whit 04]. Their survival prognosis is more favorable than other types of gliomas: total remission for LGG is possible, whereas for instance the average survival time for glioblastoma is 12 months [Dole 12]. The main treatment option in LGGs is surgical resection with a careful consideration of the brain eloquent areas to avoid neurological deficiencies. Total surgical resection was shown to increase the survival rate [McGi 08, Ius 12, Orri 12]. Moliterno *et al.* state that *"when possible, aggressive resection of malignant gliomas is the preferred initial step in management. Tumor resection to the maximum extent that is safely possible can decrease tumor burden and thereby enhance the effects of adjuvant therapies, improve symptoms from mass effect, reduce the frequency of seizures, and provide tissue for pathological and genomic studies to better identify and test novel therapy"* [Moli 12]. On the other hand *"the likelihood of complications increases with the proximity of the lesion to eloquent cortex. If it is within* $0.5\ cm$ *of functionally active and important brain, there is a high risk of complications"* [Whit 04]. Yet, due to their infiltrative nature, residual tumors can cause an LGG to evolve into a more aggressive high–grade glioma (HGG – grade III or IV). The competition between these two criteria – *extent–of–resection (EOR)* and *post–operative morbidity* – is a clear indication for an intra–operative method that allows for detecting post–resection residual tumors and thereby guides the surgeon in extending the resection accordingly. In addition, the state–of–the–art techniques MRI and CT were shown to fail to accurately identify the full extent of brain tumors, as well as microscopic infiltration. This is another indication for an intra–operative (i.e. real–time) method to be utilized in neurosurgery [Ghol 11].

Although [^{18}F]FDG–PET has become the state–of–the–art imaging modality for the imaging and grading of tumors, it suffers from a low T/B uptake ratio in brain tumors. This is due to the fact that the brain consumes large amounts of glucose and therefore the glucose metabolism of a brain tumor does not sufficiently contrast to the peri–tumoral healthy tissue. On the other hand, amino acid analogs like [^{18}F]FET yield higher T/B ratios in brain tumors. For instance [^{18}F]FDG (glucose analog) yields 1.7, whereas [^{18}F]FET (amino acid analog) yields 3.1 [Boga 09]. In addition, [^{18}F]FET is reported to be useful in surgery planning [Gros 10] and post–operative detection of malignant residual tumor [Popp 04]. Two other amino

acid analogs [^{18}F]FDOPA[1] and [^{11}C]MET[2] yield 2.0 T/B ratio [Bech 03]. This is the reason why amino acid analogs have much higher specificity in tumor mass delineation [Paul 03, Gros 10], both in LGGs and HGGs [Popp 04]. Another (though not an amino acid analog) radiotracer used for imaging brain tumors is [^{18}F]12c[3], which yields a very high T/B ratio of 8 [Boga 09]. Based on all these findings, our hypothesis is that using our system in conjunction with such radiotracers intra–operatively can help the neurosurgeon to detect post–resection residual tumors and increase the EOR accordingly. In a concrete neurosurgery scenario, [^{18}F]FET could be injected after the surgical hole in the skull has been opened (i.e. *craniotomy*), but $30\ min$ before the actual resection of the tumor. This $30\ min$ gap until the resection would ensure that the radiotracer reaches the optimal T/B uptake ratio, or the plateau of constant radioactivity (see section 3.1.2) by the time the neurosurgeon has finished the resection. It is exactly at this point that epiphanography would be used for inspecting the tumor cavity.

In a clinical scenario, the residual tumor is due to the neurosurgeon's limitations to distinguish between healthy and tumoral tissue, especially with LGGs (where tumoral tissue is not much different than healthy tissue and LGGs tend to infiltrate surrounding healthy tissues), except of course, when residual tumor is deliberately left in order to avoid post–operative neurological deficits. Epiphanography in that respect is a promising approach that could enhance the neurosurgeon's vision. Considering the high correlation between the EOR and the overall survival rate [Orri 12], epiphanography could have a high impact on the neurosurgical management of especially the infiltrative LGGs, as the objective in the surgical management of LGGs is to remove as much tumoral tissue as possible to avoid recurrence or malignant progression, with minimal brain damage and minimal post–operative function loss.

5.2. Design & System Setup

5.2.1. General system setup

Our system combines a *beta probe (NodeSeeker 800, Intra Medical Imaging LLC, Los Angeles, CA, USA)*, and an *optical tracking system (Polaris Vicra, Northern Digital*

[1] L–3,4–Dihydroxy–6–[^{18}F]fluorophenylalanine
[2] L–[methyl–^{11}C]Methionine
[3] [^{18}F]Fluoro–[1,2–2H4]choline

Incorporated, Waterloo, ON, Canada) and is depicted in figure 5.1. The following two subsections give brief information about these two components.

5.2.1.1. Beta (positron) probe

A beta (or positron) probe is a device that can detect positrons. It follows from the typically millimetric penetration depths of positrons in tissue, that the positrons detected by a beta probe must have been emitted from within a few millimeters of the surface. This is why a beta probe is very sensitive to positron sources *at* or *very close to* the surface, and virtually insensitive to deeper ones. Our beta probe together with the control unit is depicted in figure 5.1. It features two plastic scintillators: one cylindrical, and one ring–shaped. The two scintillators are concentric, and the ring detector is shielded with a $1\ mm$ stainless steel layer, which stops almost all positrons with energies lower than $1.5\ MeV$. As mentioned in section 3.2.2, a plastic scintillator cannot be used for efficiently detecting the $511\ keV$ annihilation photons. Yet, annihilation photons still interact with it, thereby causing *false positives*, or *contamination* in the signal. The rationale behind the ring detector in the NodeSeeker 800 beta probe is to account for this contamination of the main (cylindrical) detector (see [Dagh 94] for a more detailed discussion).

The beta probe must be calibrated for the detection of the positrons of the specific isotope to be used (^{18}F in our case), before it can be utilized. The calibration consists of three steps:

1. *Count acquisition and channel selection* A point source containing ^{18}F is put close to the probe's sensitive area, and the data acquisition for the twenty channels of the two detectors is started. The point source is to remain at the same position for the whole acquisition. Once the acquisition is finished, a histogram of counted events is obtained for the twenty channels of both detectors. Then, based on the typical energy spectrum of positrons for the isotope in question, the first few channels are to be excluded, by selecting the rest, in order to minimize the detection noise[4].

2. *Mutual detector sensitivity estimation* The same ^{18}F point source is covered (e.g. with a coin) such that all the positrons are stopped before reaching the probe detectors. The purpose of this step is to flood both probe detectors

[4]The positron energy spectrum is only vaguely discernable from the histogram of counted events (binned into the twenty channels), so in practice the channel selection is done purely based on the specifications of the manufacturer.

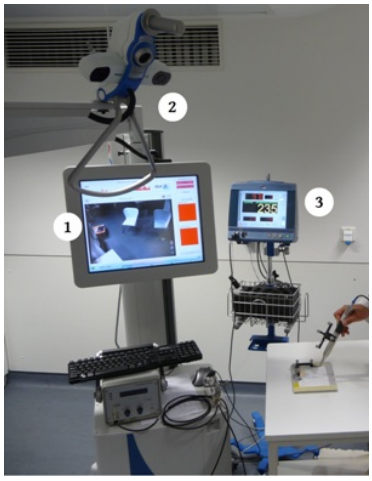

(a) The navigated probe system setup.

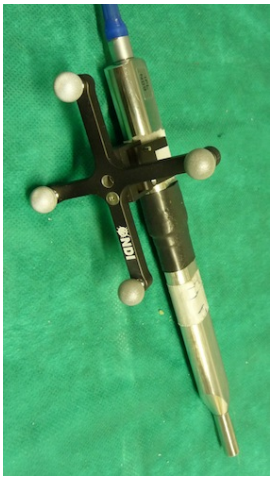

(b) Close up view of the beta probe.

Figure 5.1.: Navigated beta probe system setup. 5.1(a)) 1) Augmented reality (AR) visualization. 2) Polaris Vicra optical tracking system. 3) NodeSeeker 800 control unit (beta probe hand–held on the right). 5.1(b)) The beta probe with an attached tracking target.

with photons, for determining their respective sensitivities to photons. This step should be performed with care as it is crucial for computing the weighting factor that will be used for subtracting the pure photon signal (registered by the ring detector) from the photon–contaminated positron signal (registered by the cylindrical detector) in order to obtain the net positron count.

3. *Quality control* This step is for a qualitative check of the quality of the performed calibration. A ^{22}Na source is to be used. In this step, the overall detection sensitivity of the probe is also reported.

5.2.1.2. Optical tracking system

The Polaris Vicra optical tracking system comprises two near infra–red cameras, with *strobe lights* close to each (see figure 5.2). The strobe lights *illuminate* the scene with near infra–red light, which is reflected by dedicated spheres called *fiducials*, a rigid set of which comprises a *tracking target* (see figure 5.1(b)). Spherical fiducials are very suitable in particular, due to the fact that the image of a sphere is always a circle regardless of orientation [Reic 13]. The two cameras are rigidly fixed to each

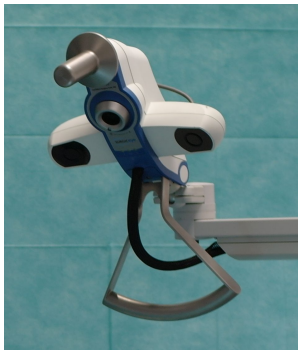

(a) declipseSPECT imaging system (SurgicEye GmbH, Munich, Germany), including an NDI Polaris Vicra.

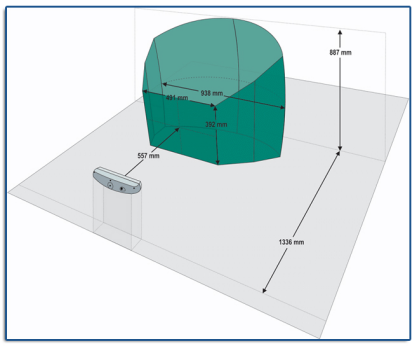

(b) Tracking volume of NDI Polaris Vicra.

Figure 5.2.: A clinically used optical tracking system and its conceptual tracking volume. In 5.2(a)) part of the black regions around the two tracking cameras left and right are rings of infra–red strobe lights. 5.2(a)) ***Copyright notice:*** *Image courtesy of Dr. Tobias Reichl.* 5.2(b)) ***Copyright notice:*** *Image courtesy of NDI, reprinted from [Pola 13].*

other, and *calibrated*, i.e. in a known geometric configuration. The tracking system works in three steps. In the first step, the fiducials, which can be distinguished very well in the camera images due to their brightness, are segmented. In the second step, the position of each fiducial is triangulated[5]. Each tracking target has a unique geometry consisting of at least three fiducials, by which the target registration is performed in the third and final step. Lack of symmetry and lack of collinearity within the geometric shape defined by the fiducial positions within a tracking target are crucial factors for accurate tracking. For more details on the principles of tracking, as well as a very good review of state–of–the–art tracking technologies, see [Reic 13].

In concrete tracking scenarios, there is usually a need for localizing an instrument relative to a scan object (e.g. a patient, or a phantom). Therefore a unique tracking target is attached to both of these. The tracking system provides in real–time the transformations ${}^{world}T_{inst}{}^{(k)} \in \mathbb{R}^{4\times4}$ and ${}^{world}T_{obj}{}^{(k)} \in \mathbb{R}^{4\times4}$, denoting respectively the transformation from the instrument tracking target to the world (i.e. the coordinates of the tracking system) and from the scan object to the world. The super–index k indicates that these transformations are valid only at a point k

[5]For triangulation, the fiducial must be visible in at least two camera images.

in time. In addition, the actual point of interest on the instrument or within the scan object is usually not exactly the tracking target itself, but rather some other point that is rigidly related to its tracking target. For instance, in figure 5.1(b), the tip of the probe is of interest rather than the actual position of the tracking target. Therefore two other (usually rigid) transformations ${}^{inst}T_{tip} \in \mathbb{R}^{4\times4}$ (from the instrument's tip to the instrument tracking target) and ${}^{roi}T_{obj} \in \mathbb{R}^{4\times4}$ (from the scan object's tracking target to the *region of interest – ROI –* within the scan object) are also involved. In our scenario both of these transformations are rigid, which is why they are not marked with the super–index k. If neither scaling nor projection are involved in these transformations (which is the case in our scenario), each of these transformations can be decomposed in the following fashion:

$$T = \begin{bmatrix} R & t \\ 0 & 1 \end{bmatrix} \tag{5.1}$$

where $R \in \mathbb{R}^{3\times3}$ is a *rotation matrix*, and $t \in \mathbb{R}^{3\times1}$ is a *translation vector*.

A 3D point $p_o \in \mathbb{R}^{3\times1}$ within a coordinate system o can be transformed to the corresponding point $p_c \in \mathbb{R}^{3\times1}$ within another coordinate system c via the following equations:

$$\begin{bmatrix} p_c \\ 1 \end{bmatrix} = {}^{c}T_o \begin{bmatrix} p_o \\ 1 \end{bmatrix} \tag{5.2}$$

$$= \begin{bmatrix} {}^{c}R_o & {}^{c}t_o \\ 0 & 1 \end{bmatrix} \begin{bmatrix} p_o \\ 1 \end{bmatrix} \tag{5.3}$$

$$= \begin{bmatrix} {}^{c}R_o\, p_o \;+\; {}^{c}t_o \\ 1 \end{bmatrix} \tag{5.4}$$

Hence p_c is related to p_o by:

$$p_c = {}^{c}R_o\, p_o \;+\; {}^{c}t_o \tag{5.5}$$

Transforming a point p_{tip} at the tip of the probe to the corresponding ROI coordinate system point ${p_{roi}}^{(k)}$ involves the compound transformation ${}^{roi}{T_{tip}}^{(k)}$ (from the tip of the probe to the ROI):

$$\begin{bmatrix} {p_{roi}}^{(k)} \\ 1 \end{bmatrix} = {}^{roi}{T_{tip}}^{(k)} \begin{bmatrix} p_{tip} \\ 1 \end{bmatrix} \tag{5.6}$$

This compound transformation can be decomposed in the following way:

$$
\begin{aligned}
{}^{roi}T_{tip}{}^{(k)} &= {}^{roi}T_{world}{}^{(k)}\ {}^{world}T_{tip}{}^{(k)} && (5.7)\\
&= \left({}^{roi}T_{obj}{}^{(k)}\ {}^{obj}T_{world}{}^{(k)}\right)\ \left({}^{world}T_{inst}{}^{(k)}\ {}^{inst}T_{tip}{}^{(k)}\right) && (5.8)\\
&= {}^{roi}T_{obj}\ \left({}^{world}T_{obj}{}^{(k)}\right)^{-1}\ {}^{world}T_{inst}{}^{(k)}\ \left({}^{tip}T_{inst}\right)^{-1} && (5.9)
\end{aligned}
$$

As mentioned before, the transformations ${}^{world}T_{obj}{}^{(k)}$ and ${}^{world}T_{inst}{}^{(k)}$ are provided in real–time by the tracking system. On the other hand ${}^{tip}T_{inst}$ and ${}^{roi}T_{obj}$ are to be determined in advance. This is the whole calibration required for tracking.

5.2.2. Epiphanographic imaging with beta probes

A beta probe by itself provides only a count rate (referred to as *probe reading* from this point on) that is ideally proportional to the level of radioactivity within its *field of view (FOV)*. This information is by itself of limited use within a surgery. First of all, it is almost impossible for the surgeon using a beta probe to follow the numerical values of the probe reading visually. This problem is overcome by an audio feedback mechanism integrated into the probe control unit depicted in figure 5.1(a). Although a great improvement compared to the mere numerical value, the audio feedback is still of limited use: it is rather the information contained in the spatial distribution of the radiotracer that is of interest to the surgeon.

Combining a beta probe with a spatial localization system makes it possible to record the probe readings synchronously with the probe position relative to the patient. This opens the way for generating 3D images of the spatial distribution of the radiotracer, which can be used for guiding cancer surgery intra–operatively by augmenting the surgeon's view with real–time information. The idea of combining a beta probe with a spatial localization system was first proposed by Wendler *et al.* in [Wend 06]. In their work, Wendler *et al.* conceptualized each probe reading as the count rate of an infinitesimal positron detector in 3D space. They visualized this data by connecting those 3D positions into a triangulated mesh. As such, they laid down the foundations towards using a non–imaging beta probe within a real–time imaging modality. Although this first work was a very innovative step, it had the major pitfall of assuming an infinitesimal detector size, thereby neglecting the physical and geometric laws governing

the detection of positrons. In addition the main medical application scenario for epiphanography is the detection of residual tumor after resection. Typically small tumor deposits with diameter smaller than $5\ mm$ are of interest in this scenario. The approach presented in [Wend 06] in that sense is faced with a major constraint: the resolution is limited by the sensitive area of the detector. To give an example, a scintillating detector with a diameter of $8\ mm$ can with this approach be used to detect a circular tumor deposit of $8\ mm$ diameter in the best case.

The first major contribution of our work is an attempt to model the detection of positrons mathematically to overcome this limitation on the resolution. Similarly to how the detection of annihilation photons is modeled in PET (see section 3.3), we discretize the geometric surface model (referred to as *surface of interest – SOI* – from here on). We call each element of the SOI a *suxel* (short for ***su**rface vo**xel***). Each suxel j has an (unknown) activity value c_j. Each probe reading value m_i can thus be formulated as a linear combination of the activity values of the suxels, with almost the same logic as in equation 3.8, which we would like to once again expand here for the sake of clarity:

$$m_i = \sum_j a_{ij}\ c_j$$

In PET, the a_{ij}'s that fall within the LOR indexed i are non–zero. Using the same analogy, in epiphanography the a_{ij}'s that fall within the FOV of the beta probe are non–zero. A major difference however, is that the geometry of a PET tomograph is known a priory, and therefore the a_{ij}'s can be determined in advance by e.g. Monte Carlo simulation [Read 07]. On the other hand, the a_{ij}'s in epiphanography are never known in advance, due to *i)* the fact that data is acquired with a *freehand* scan, and *ii)* the varying surface topology. We use *analytical ad–hoc detection models* for computing these coefficients *on–the–fly* in epiphanography. In the course of our research work, we have developed and evaluated several of these, which we present in section 5.5.

5.2.3. Challenges & limitations

Similarly to the case of image generation in PET, thanks to the probe models, data acquired with our system can be described by equation 3.9: $\mathbf{Ac} = \mathbf{m}$, where $\mathbf{A}$ is the matrix of the coefficients a_{ij} computed with the ad–hoc model; $\mathbf{c}$ is vector of the (unknown) suxel activity values; and $\mathbf{m}$ is the vector of the probe readings.

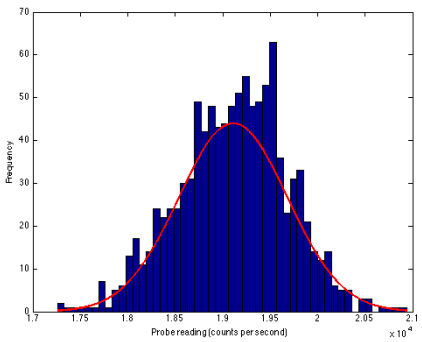

Figure 5.3.: Histogram of probe readings acquired for 2 min with a single point source at a fixed position. A single probe reading in a freehand scan can be conceptualized as *picking a value at random* from the x–axis of this graph. The red line is the normal distribution fitted to the probe readings. The probability of *picking the mean value of this distribution* – i.e. measuring the correct activity – in a freehand scan is very low – numerically speaking 4.62 % for this particular dataset.

However, the acceptable time to obtain data with epiphanography in an intra–operative setting is typically on the order of a few minutes. This leads to the major limitation that the obtained data do not have statistically sufficient information (see figure 5.3).

Another important factor affecting the data quality is the measurement noise. Measurement noise becomes apparent in lower activity concentrations, which are unfortunately also what is to be expected in a real–life setting. The data quality might also be severely hampered if the probe is not well–calibrated in terms of rejecting annihilation photons. This effect is minimal for NodeSeeker 800, as far as we could discern, but is worth mentioning here as a possible cause of low quality data.

Apart from these limitations, the major issues for epiphanography are related to the actual scan procedure. The fact that the data is obtained with a *freehand* scan might lead to the problem that, depending on the data rate of the used probe and the scanning speed of the operator, the probe reading is not of a stationary probe position in space, but rather an accumulated value of several consecutive positions. This effect leads to a *smearing* of the high activities, and hence to resolution loss. The higher the speed at which the operator scans, the more pronounced this effect becomes.

All these limitations make the linear system $\mathbf{Ac} = \mathbf{m}$ obtained in epiphanography ill–posed, rendering a direct inversion of the linear system $\mathbf{Ac} = \mathbf{m}$ ($\mathbf{c} = \mathbf{A}^{-1}\mathbf{m}$) virtually impossible. Instead, similar to the case of PET image generation, an iterative approach like MLEM, which inherently takes into account the nature of radiation detection, is more suitable. For generating images with epiphanography, we apply MLEM with 25 iterations, selected heuristically based on our experience. Furthermore, smoothing with a Gaussian kernel is usually necessary to dump the effect of noise in the generated images.

Due to the fact that a beta probe is very sensitive to superficial radiation, it has to be kept very close to the surface during data acquisition (in fact, sterilization with e.g. latex sheathing in the OR might be an issue because of this – for a discussion of this issue on the basis of practical experiments, see [Thac 08]). This means that even small errors in the detector–to–source distance values (the parameter d_{ij} wherever applicable in the ad–hoc models to be explained in section 5.5) might have pronounced negative influences directly in the resulting linear system, contributing for the worse to its ill–posedness. The first source of error in the detector–to–source distance is the localization error of the tracking system (or the *tracking error*). The tracking error is larger in the edges of the tracking volume [Reic 13]. Therefore it is important that the scan be performed inside the optimal part of the tracking volume.

The issue of the acquisition and mathematical representation of the SOI for use in epiphanography is a problem in itself. In an intra–operative setting, first of all, some surface points representative of the SOI are to be obtained. This can be performed using a tracking pointer or with a combined infra–red laser and optical tracking approach [Wend 08]. Both methods require extra time (i.e. apart from the actual epiphanography scan). The former approach should be more accurate, however with limited applicability in an intra–operative setting. The latter approach has the advantage of being *touch–free*, however it works only when the surface to be scanned is totally exposed. A third approach is to *infer* the surface point positions from the probe tip positions recorded during the epiphanography scan. The advantages of this are that *i)* it does not require extra time, *ii)* it makes sure that all the regions of the surface that the probe sweeps are covered. Nevertheless, accuracy may become a concern esp. when the probe–to–surface distance varies significantly between measurements. As to the representation of the SOI, our software platform outlined in appendix C supports surface meshing for arbitrary surfaces from a point cloud.

The attenuation of positrons in tissue is a line spread function (see the work of Cho *et al.* [Cho 75]). This attenuation can be modeled after the curves presented by Cho *et al.* in their work. However, as these curves span a sub–millimeter spatial resolution, modeling the attenuation as a function of the depth makes sense only if the above mentioned errors pertaining to the representation of the surface can be properly addressed.

Last but not least, to be able to correctly delineate the post–excision residual tumor from the peri–tumoral healthy tissue it is important to have a good T/B radiotracer uptake contrast. The T/B uptake ratio depends principally on the physiology of the radiotracer used for imaging. However, the imaging protocol does contribute – for the better or for the worse – to how well the T/B uptake ratio is captured in the obtained epiphanography images.

5.3. Spatial Resolution

FOR preventing tumor recurrence, it is important to detect small residual tumor masses. It is in that respect important to quantify the resolution limitations of our system. In this section we outline the experimental study we have conducted especially for this purpose.

We devised a resolution phantom featuring a compact disc (CD) box and drilled small holes on top of this CD box, comprising hole pairs with mutual distances ranging (in $1\ mm$ steps) from $4\ mm$ to $13\ mm$ (see figure 5.4). We obtained the ground truth positions of these holes by pointing a tracking pointer directly on each hole.

After filling two *haematocrit tubes* (see figure 5.4(c)) with ^{18}F fluid, we inserted them into the mutual hole pairs, fixing them with a sponge we had inserted into the CD box. This construction gave us two point sources with one of the mentioned distances in between. On each such tube placement we scanned the surface with our epiphanography system. The two point sources are distinguishable in the $11\ mm$ and $12\ mm$ images, albeit with a not so small artifact in the latter (see figure 5.5). In these images there is some misalignment between the reconstructed image and the ground truth image. We believe this is on the one hand due to the continuous placement–replacement of the haematocrit tubes. On the other hand, the skewness of the probe with respect to the surface during the free-hand scan might also have contributed to this misalignment (we used the *ad–hoc*

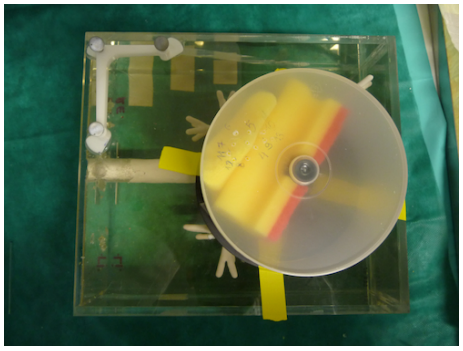

(a) Resolution phantom from top.

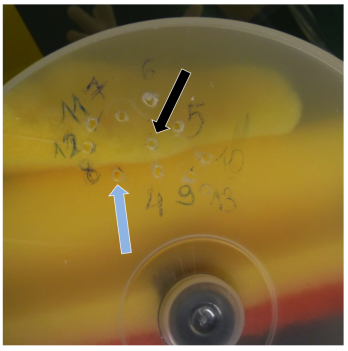

(b) Close–up view of the holes.

(c) Haematocrit tube.

Figure 5.4.: The resolution phantom. 5.4(a) Holes are marked with a pen. 5.4(b) Arrows show the hole pair with $8\ mm$ mutual distance. 5.4(c) Note that the upper two thirds of the haematocrit tube are filled with stained radioactive fluid. The tip of the beta probe is visible in the upper part of the image.

model described in section 5.5.4, which tends to assign larger activities *along* the probe axis). All the spatial resolution phantom images can be seen in appendix A.

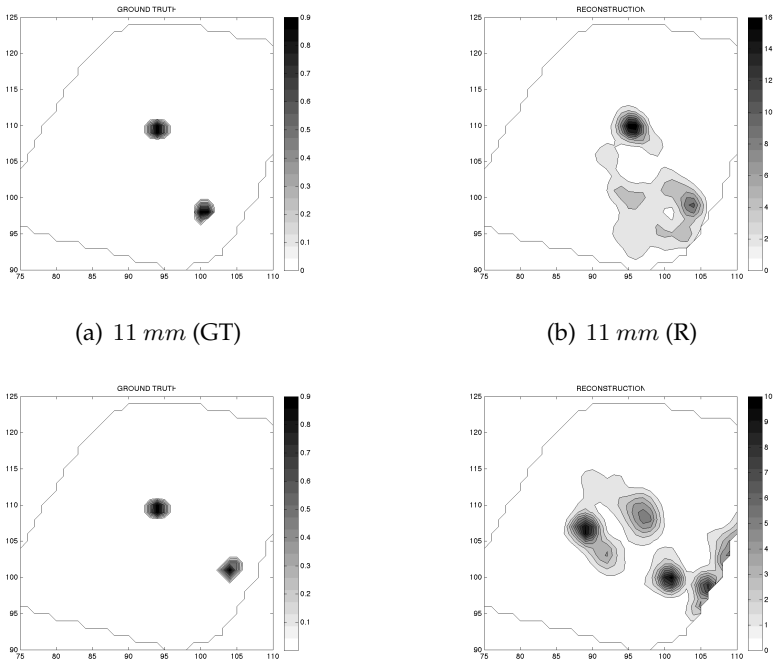

(a) 11 mm (GT)

(b) 11 mm (R)

(c) 12 mm (GT)

(d) 12 mm (R)

Figure 5.5.: Selected reconstructions of the resolution phantom scans. *(GT):* ground truth. *(R):* reconstruction (mm is used as unit in these as well as other images with axes throughout the thesis, unless indicated otherwise).

5.4. Biological Feasibility Study

APART from the resolution limitations, it is also important to assess how well the beta probe can be used for localizing tumor cell colonies. Such an assessment provides further data for quantifying the resolution limitations. Nevertheless in order to conduct such a study there is need for a known ground truth in terms of the precise location and shape of the cell colonies involved. To meet this need, we used a variant of the *bladder carcinoma* cell line *EJ 28*, that is genetically modified (in other words *transfected*) such that they are capable of producing the *firefly–luciferase* enzyme. This is reflected in the suffix *–luc* appended to the name of the cell line: *EJ 28–luc*. This enzyme *catalyzes* the *oxidation* of *luciferin* to *oxyluciferin*. This produced oxyluciferin is in an excited state of energy, which causes it to emit the excessive energy in the form of light (for a more detailed discussion of the chemistry of this reaction, as well as an historical background, see [Frag 08]). Due to the fact that this light emission comes from living cells, it is called *bioluminescence*. Bioluminescence allows for imaging EJ 28–luc cell colonies under suitable conditions with a special sensitive *charge–coupled–device (CCD)* camera. The core assumption of our study is that the spatial bioluminescence signal intensity correlates with the density of these tumor cells. Therefore we used the bioluminescence signal intensity as a ground truth for tumor cell density. Apart from the EJ 28–luc cell line, we also used cell colonies of *human foreskin fibroblasts (HFF)* in order to simulate healthy peri–tumoral tissue.

5.4.1. Experiment setup

We seeded and grew the EJ 28–luc and HFF cells in two different spatial configurations, so as to emulate small tumor deposits (of EJ 28–luc cells) against a background of peri–tumoral healthy tissue (of HFF cells). The first spatial configuration featured two tumor spots and two healthy tissue spots, with all four being disjoint from each other. We grew this spatial configuration on a single Petri dish (see figure 5.11(a)), and refer to it as Cell_{22}. The second spatial configuration featured a homogeneous layer of HFFs on the Petri dish surface, on top of which we seeded and grew three tumor spots. We grew this configuration on two Petri dishes (see figure 5.11(b) and figure 5.11(c)), and refer to them as Cell_{31a} and Cell_{31b} respectively.

In order to register the different modality images of each single Petri dish in

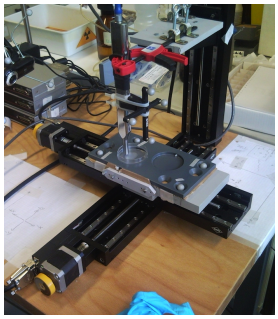

(a) The scan setup with the beta probe, the Petri dish attached to the fixation plate, and finally the fixation plate attached to the step motor.

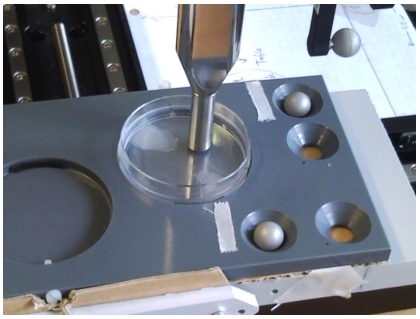

(b) A close–up view of the probe tip scanning the Petri dish surface.

Figure 5.6.: Step motor–probe setup for scanning Petri dishes. Note how the tracking fiducials are placed on the fixation plate holes for forming a tracking target in 5.6(a).

this study, there was need for a common reference. For this purpose we designed a special fixation plate that allows for rigidly attaching Petri dishes (see figure 5.9). This fixation plate features eight holes that serve two purposes. First, they can be used as landmarks for localizing the Petri dish in each image. For this purpose, an additional (bright–field) image (see figure 5.8) has to be taken accompanying each bioluminescence image acquisition. Secondly, the holes serve the purpose of placing tracking fiducials in a pre–defined geometrical configuration such that they form a tracking target (see figure 5.6(a)). We assume that the centroids of the fiducials segmented by the optical tracking system and the centroids segmented from the images as in figure 5.8 correspond to the same point due to the spherical/circular – i.e. symmetric – geometry in each case.

5.4.2. Experiment protocol

On the day of the experiment, we supplied each Petri dish with a $3\ ml$ reduced–glucose medium ($1\ mg/ml$). We then induced bioluminescence in the EJ 28–luc colonies by adding $0.1\ ml$ luciferine per Petri dish and took a bioluminescence image together with a co–registered bright–field image using the CCD device. Following that, we incubated the cells for $30\ min$ in $3\ ml$ [^{18}F]FDG solution ($3.071\ MBq/ml$). We scanned each Petri dish's surface with our beta probe–step

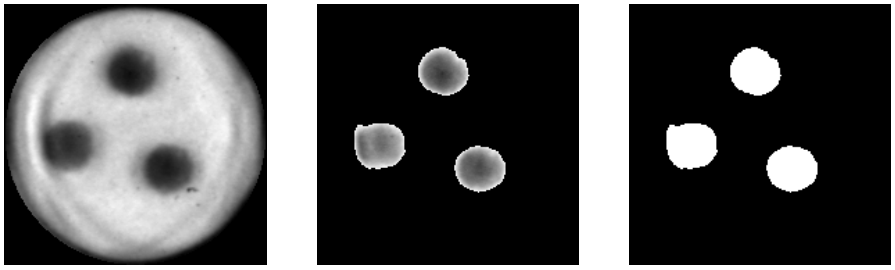

(a) Three EJ 28–luc colonies stained with trypan blue.

(b) The three colonies segmented.

(c) The binary segmentation image.

Figure 5.7.: Segmentation of EJ 28–luc colonies after staining.

motor construction shown in figure 5.6(a), featuring the *beta probe (NodeSeeker 800, IntraMedical Imaging LLC, Los Angeles, CA, USA)* rigidly attached to a *step motor (Owis GmbH, Staufen im Breisgau, Germany)*.

After the scan, we stained each Petri dish with the *trypan blue* dye[6], and took a bright–field image. Colonies of both cell lines get stained with this dye, however there is a clear contrast between the respective dye uptakes due to the different cell densities (see figure 5.9), apparent in the bright–field images (see for an example figure 5.7(a)). Consequently, tumor colonies can be easily segmented from these images (see figure 5.7(b)).

5.4.3. Evaluation & results

Each scan consisted of a regular circular raster customized to cover the Petri dish's surface in $1\ mm$ steps. We acquired probe readings for $3\ sec$ (approximately 30 measurements) per raster position. As the measurement for a specific raster position, we took the average value of the time–corrected (i.e. to account for the radioactive decay) probe readings for that raster position. We then generated positron emission images by interpolating these averaged readings (see the middle row in figure 5.11), i.e. without applying any reconstruction.

We segmented the Petri dish surface from each bioluminescence image using the visible edges of the Petri dish in the corresponding co–registered bright–field image (see figure 5.8). In addition, we segmented the known features of the tracking plate seen in these images, in order to compute the coordinate system used by

[6]For more information on trypan blue, see the corresponding entry in PubChem [The 13a].

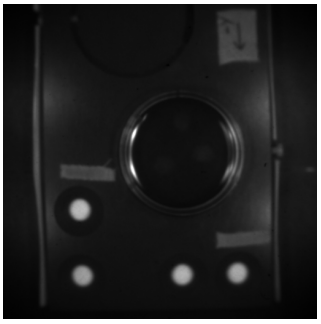

(a) Petri dish attached to the fixation plate.

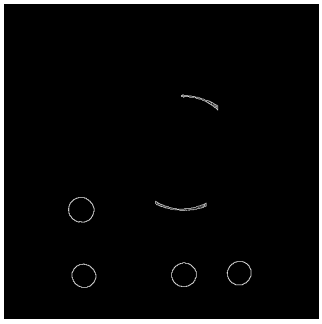

(b) The same image with segmented features.

Figure 5.8.: Bright–field image of a Petri dish attached to the fixation plate and the corresponding segmentation. The holes of the fixation plate can be segmented to provide a common reference for registration between different images. The Petri dish is localized based on the segmentation of the visible portion of its edges, and later fitting a circle to these segmented edges.

the tracking system in the image coordinates as well as the metric–to–pixel scaling. For all segmentations, we used the *seeded region growing* algorithm [Adam 94]. The biolumiscence and the corresponding positron emission image were slightly misaligned in each case. This implies our assumption in section 5.4.1 of the correspondence between the center of the tracking fiducials and the center of the segmented tracking plate circles correspond to the same point in space is wrong. We corrected this consistent misalignment using the average distance between the center of the tumor spots in the bioluminescence image and the center of the respective spots in the positron emission image.

The tumor spots can be visually identified in all the positron emission images, which look quite similar to the bioluminescence images (see the middle row in figure 5.11). Positron emission images yielded 87 % mean *normalized cross–correlation (NCC)* to the bioluminescence images. All numerical results can be seen in figure 5.10.

We presented this study at the annual meeting of the *Society of Nuclear Medicine (SNM)*[7] [Shak 10a]. This study shows that positron emission imaging is a feasible approach giving strong correlation to the expected ground truth, provided that statistically sufficient data can be collected with a navigated beta probe. We

[7]SNM is now the *Society of Nuclear Medicine and Molecular Imaging (SNMMI)*.

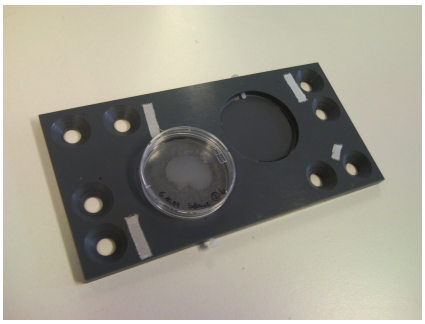

(a) Petri dish with a single EJ 28–luc colony (faintly seen whitish spot) on top of HFFs.

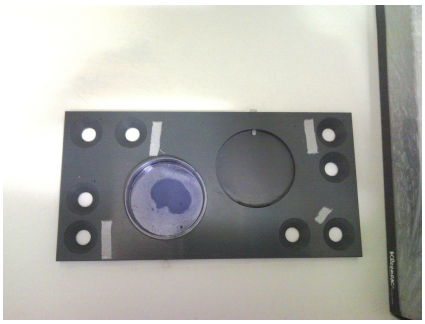

(b) The same Petri dish stained with trypan blue.

Figure 5.9.: Petri dish attached to the fixation plate. Note in 5.9(b) that the EJ 28–luc colony has a clear contrasting dense blue compared to the much more faintly seen HFF colony.

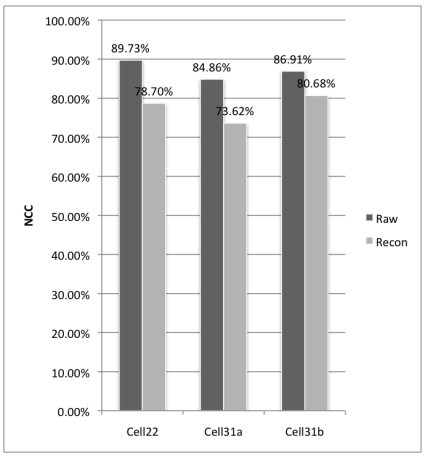

(a) NCC

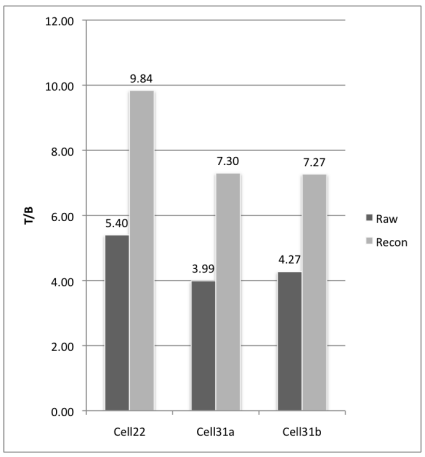

(b) T/B

Figure 5.10.: Numerical results: raw probe readings vs. reconstruction. $Cell_{22}$, $Cell_{31a}$, $Cell_{31b}$ are abbreviations corresponding to cell configurations in figures 5.11(a), 5.11(b), 5.11(c) respectively.

should however also state that the positron emission images generated using this approach fail to resolve structures smaller than the sensitive area of the probe (compare for instance figure 5.11(e) to its ground truth in figure 5.11(b)), which is not unexpected, in the light of the discussions in section 5.2.2.

5.5. Ad–hoc Detection Models

BEFORE we start our discussion of the different ad–hoc models we have developed, we would like to motivate the reader by showing the advantage of adopting a reconstruction approach compared to the raw probe readings. For this purpose we reconstructed images using the cell study data outlined in the previous section. We used a discretization grid of $1 \times 1\ mm^2$ suxels covering the Petri dish surface and applied the MLEM algorithm (briefly outlined in section 3.3) with 25 iterations (heuristically selected) to the linear system obtained using the *solid angle model* (explained in the following subsection). This resulted in a minor decline in the NCC to the bioluminescence images (mean 77 %: compare to 87 % achieved by the raw probe readings). However the reconstructed images almost **doubled** the T/B signal contrast (mean 8.17: compare to 4.13 of the raw probe readings). We present a detailed overview of the numerical results in figure 5.10. Figure 5.11 shows how raw probe readings compare to the reconstructed images. Note in the images how the reconstruction compensates for the smearing present around the hot spot borders in the positron emission images obtained by interpolating raw probe readings [Shak 10b].

Although this factor of doubled T/B contrast is in itself a great improvement, it is important to develop even better ad–hoc models. The main motivation for this is to be able to cope with reduced T/B uptake situations in real–life conditions for resolving small tumor deposits.

In each of the following four subsections we introduce one of the ad–hoc models we have developed in the course of our research work. These are the *solid angle model*, *look–up table (LUT) model*, *LUT–fitted analytic model*, and finally the *partition model*. We then conclude this section by presenting our work on simulating probe measurements in the last subsection.

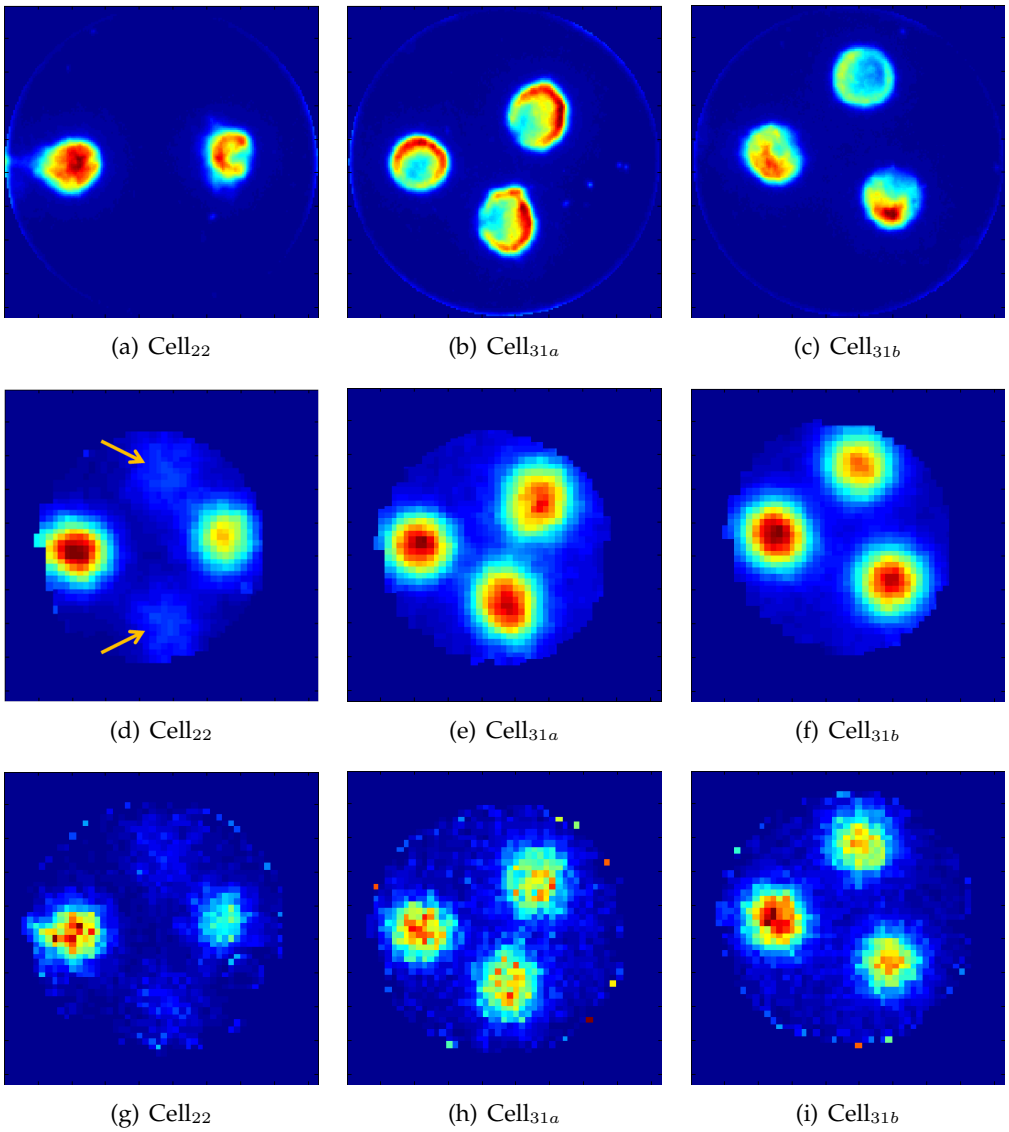

(a) Cell_{22} (b) Cell_{31a} (c) Cell_{31b}

(d) Cell_{22} (e) Cell_{31a} (f) Cell_{31b}

(g) Cell_{22} (h) Cell_{31a} (i) Cell_{31b}

Figure 5.11.: Positron emission images obtained by interpolating raw beta probe readings vs. reconstructed images. **Upper row:** bioluminescence images. **Middle row:** positron emission images obtained by interpolating raw beta probe readings (the arrows indicate the two HFF colonies captured by the beta probe). **Lower row:** reconstructed images.

5.5.1. Solid angle model

Radiation is an isotropic process in 3D space. A corollary of this is that in order to be able to detect all the radioactive events from a point source, ideally a closed form detector must be used. The most straightforward geometry for such a detector is a sphere (around the point source). However in reality this is obviously an impossible construction. Due to this phenomenon, it is impossible to detect all the radioactive events from a point source in practice. Instead, an attempt is made to approximately quantify the *portion* of radioactive events from a point source that can be detected based on the geometric position of the detector with respect to the point source. The term *solid angle subtended by the detector (on the point source)* is used in a broad sense to denote this portion. A practical formula for analytically approximating the solid angle subtended by a circular–shaped (e.g. cylindrical) detector on a point source is:

$$a_{ij} = \Omega\left(d_{ij}, r, \alpha_{ij}\right) = \frac{1}{2}\left(1 - \frac{1}{\sqrt{\frac{r^2}{(d_{ij})^2} + 1}}\right) cos\left(\alpha_{ij}\right) \tag{5.10}$$

where d_{ij} is the distance between the detector and the point source[8], r is the detector radius, and α_{ij} is the *inclination angle* (i.e. between the detector axis and the detector–to–source distance axis) – see figure 5.12 for graphical illustrations. Ω is used for denoting the solid angle.

This complex looking formula is actually very easy to decompose. The $1/2$ term on the right models the phenomenon that due to the isotropy, it is impossible to detect the events that go from the point source in the direction opposite to the detector (i.e. one half of all the events). The middle term in parantheses models first of all the effect of the detector area, which is proportional to the square of the

[8]Similar to the case of equation 3.8, we use the sub–index j to refer to the suxel j within the SOI, and i to refer to the measurement i within our epiphanography system data acquisition. We use this enumeration scheme for parameters that vary from measurement to measurement.

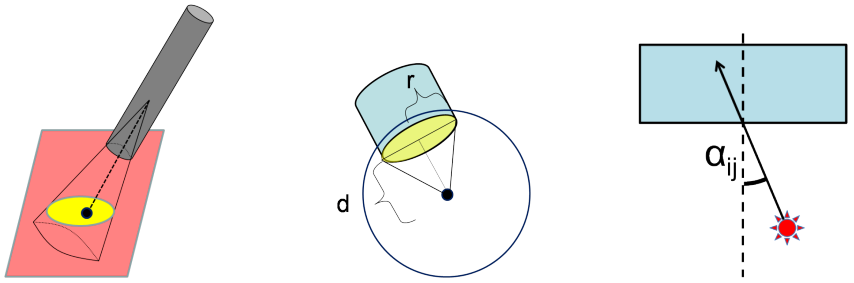

(a) Assumed conic field of view (FOV) of the probe.

(b) Solid angle subtended by the probe on a point source.

(c) Inclination angle of the detection.

Figure 5.12.: Graphical illustrations of the solid angle probe model parameters in equation 5.10. The grey cylinder in 5.12(a) illustrates the probe, while the blue cylinder/rectangle in 5.12(b) and 5.12(c) respectively illustrate the detector.

detector radius. Assuming constant d_{ij}:

$$\lim_{r \to +\infty} \left(1 - \frac{1}{\sqrt{\frac{r^2}{(d_{ij})^2} + 1}} \right) = 1 \tag{5.11}$$

$$\lim_{r \to 0} \left(1 - \frac{1}{\sqrt{\frac{r^2}{(d_{ij})^2} + 1}} \right) = 0 \tag{5.12}$$

Equation 5.11 says that the larger the radius (i.e. the larger the detector area) gets, the larger the portion of the detected events to all the events. Equation 5.12 on the other hand says that with smaller radius (i.e. smaller detector area), this portion will also diminish. The effect of ionizing radiation (e.g. on a nearby object) is inversely proportional to the distance. This is modeled with the $(d_{ij})^2$ term. Similar to the above limits:

$$\lim_{d_{ij} \to +\infty} \left(1 - \frac{1}{\sqrt{\frac{r^2}{(d_{ij})^2} + 1}} \right) = 0 \tag{5.13}$$

$$\lim_{d_{ij} \to 0} \left(1 - \frac{1}{\sqrt{\frac{r^2}{(d_{ij})^2} + 1}} \right) = 1 \tag{5.14}$$

In other words, when the distance is very large, it dominates the middle term,

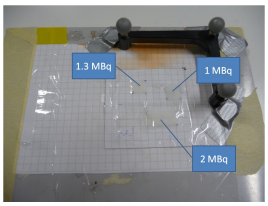

(a) The phantom with indications of the measured activities of the hot–spots.

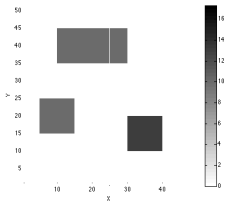

(b) The ground truth image of the phantom.

Figure 5.13.: The controlled phantom construction prepared for studying different probe models.

making it close to 0. On the other hand, when the distance is very small, the middle term comes closer to 1. The cosine term $cos\,(\alpha_{ij})$ models the sensitivity loss due to the inclination angle illustrated in figure 5.12(c) [Ozgu 09b]. For calibrating the solid angle model, we proposed a method in [Ozgu 09b]. The interested reader may consult this publication, as well as [Ozgu 09a].

5.5.1.1. Evaluation: reconstructions

For evaluating the solid angle model in a controlled setup with freehand scans, we designed a simple 2D phantom, featuring a well–defined geometry consisting of three pieces of cellulose soaked with [^{18}F]FDG and attached on a tracked plate. Two of these were of square shape with dimensions $10 \times 10\ mm^2$, and the third one rectangular with dimensions $20 \times 10\ mm^2$. The phantom construction together with indications of the corresponding activities can be seen in figure 5.13. We obtained four totally freehand scans (coded Acq_{1a}, Acq_{1b}, Acq_{3a}, and Acq_{3b}) of this phantom with our system. Each scan featured approximately 2,000 measurements (approximately $2\ min$ acquisition time). We performed two of these scans (Acq_{1a}, Acq_{1b}) at approximately $1\ cm$ distance from the plate surface and the remaining two (Acq_{3a} and Acq_{3b}) at approximately $3\ cm$ distance.

Images reconstructed using these four datasets can be seen in figure 5.14. The effect of distance is immediately clear: at $1\ cm$ the three hot–spots can be quite well distinguished in the reconstructions, while at $3\ cm$ some smearing is introduced. This smearing leads to the rectangular hot–spot appearing more like a square. The numerical values for the correlation between these images and the ground truth can be seen in figure 5.15 [Shak 11a]. These results show that epiphanography is

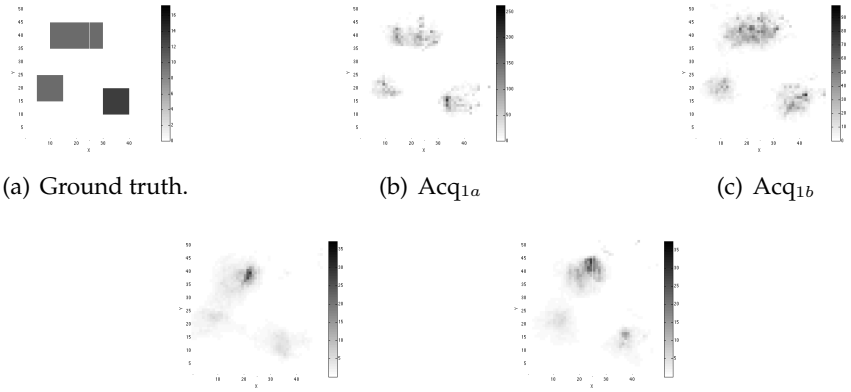

(a) Ground truth. (b) Acq_{1a} (c) Acq_{1b}

(d) Acq_{3a} (e) Acq_{3b}

Figure 5.14.: Model study phantom: reconstructions with the solid angle model.

feasible in a realistic setup in terms of the freehand scan procedure and especially short data acquisition time.

5.5.1.2. Evaluation: scattered probe readings vs. model

A curious question is how well the probe model can *predict* the actual probe measurements. For quantifying this, we *calculated* probe readings by simulating them on the basis of the solid angle ad–hoc model using the tracking data available for the four datasets. The numerical correlation values of these simulated probe readings to the real probe readings can be seen in figure 5.16. We also ran reconstructions using these simulated readings. The resulting images can be seen in figure 5.17. The numerical correlation values of these images to the ground truth image are shown in figure 5.18. Note that these correlation values are not really meaningful for comparing one probe model to some other one. However they give an idea on the ultimate limitation of the reconstruction procedure in terms of correlation to the ground truth with this specific probe model [Shak 11a].

5.5.1.3. Evaluation: rastered probe readings vs. model

We also obtained a rectangular raster of probe reading–position value pairs using a slightly modified version of the beta probe–step motor setup mentioned before. We prepared a small circular radioactive source by soaking a circular piece of cellulose (ø $12\ mm$) with $1.2\ MBq$ [^{18}F]FET (see figure 5.19(a)) and attached it rigidly

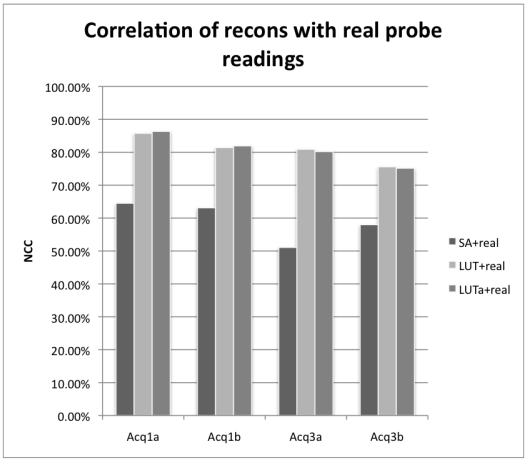

Figure 5.15.: Numerical correlation values of the reconstructions in figure 5.14, figure 5.21, and figure 5.23 (coded *SA+real*, *LUT+real*, and *LUTa+real* respectively) to the ground truth in figure 5.13(b).

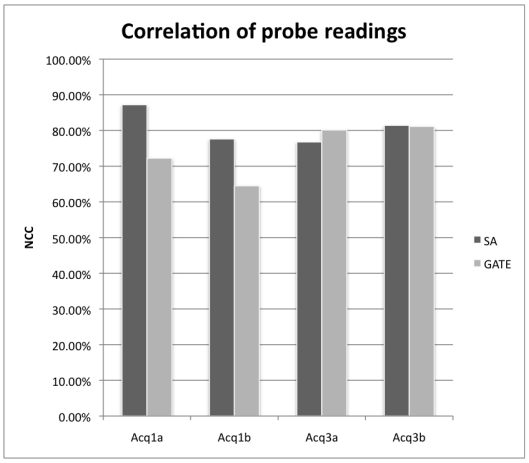

Figure 5.16.: Numerical correlation values of the probe readings simulated using the solid angle model and GATE (coded *SA*, and *GATE* respectively) to the real probe readings.

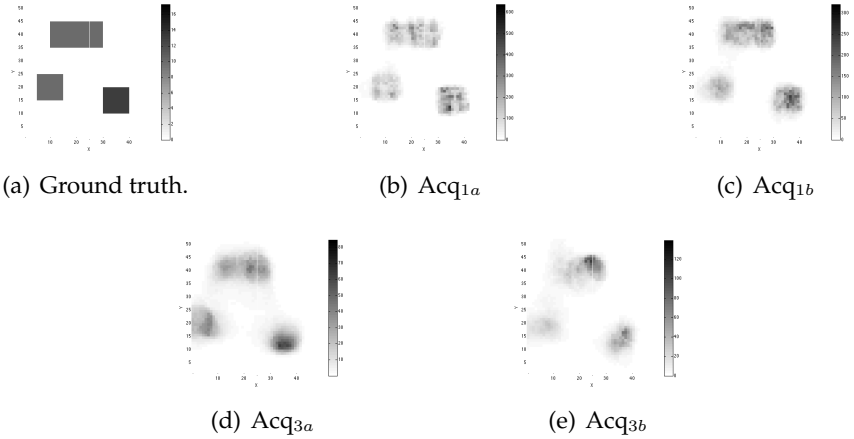

(a) Ground truth. (b) Acq_{1a} (c) Acq_{1b}

(d) Acq_{3a} (e) Acq_{3b}

Figure 5.17.: Model study phantom: reconstructions with the solid angle model (using the probe readings simulated using the same model).

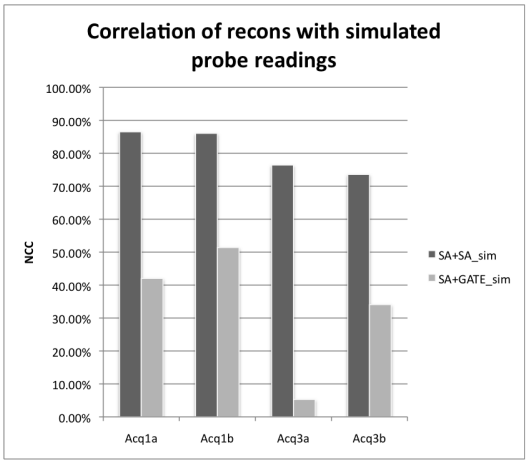

Figure 5.18.: Numerical correlation values of the reconstructions in figure 5.17, and figure 5.26 (coded *SA+SA_sim*, and *SA+GATE_sim* respectively) to the ground truth in figure 5.13(b).

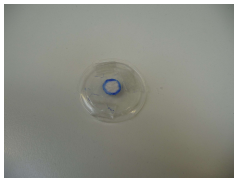

(a) Circular radioactive point source.

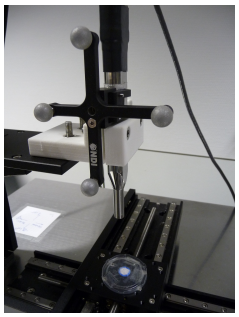

(c) The source attached to the step motor plate.

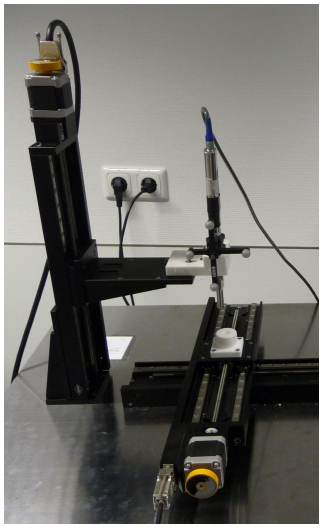

(b) The probe calibrator mount fixed on the step motor plate.

Figure 5.19.: Rectangular probe reading–position raster acquisition setup.

to the horizontal plate of the step motor. We calibrated the probe position for the most accurate alignment with the source by fitting the probe tip into a custom designed calibrator mount seen in figure 5.19(b).

We programmed the step motor to move the horizontal plate and the beta probe for generating a rectangular scan raster of $50 \times 50\ mm^2$ in steps of $1\ mm$, acquiring $9\ sec$ (approximately 90 probe readings) of probe readings per raster position. The total acquisition took about eight hours (i.e. about four half–lives of the initial ^{18}F activity). Thus in order to maximize the sensitivity, we started the acquisition with the probe at the most distant position to the radioactive source. After correcting for radioactive decay, we obtained the probe reading values in each specific raster position by averaging all acquired probe readings in that position:

$$a = a\left(d_h, d_v\right) = \frac{1}{K}\sum_{k=1}^{K} m_k\left(d_h, d_v\right) \tag{5.15}$$

where d_h and d_v are respectively the horizontal and vertical distances from the radioactive source. For all the positions dictated by the d_h and d_v values of the

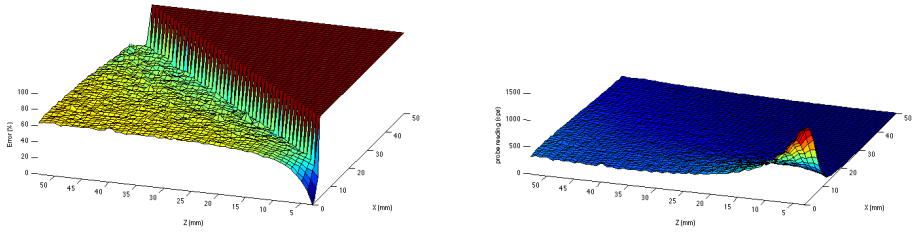

(a) Relative error of the solid angle model.

(b) Actual raster values.

Figure 5.20.: Coefficients calculated using the solid angle model vs. the raster of probe readings. **x–axis:** d_h values, **y–axis:** d_v values (both in mm), **z–axis:** relative error values as a percentage in 5.20(a); probe readings (counts per second – cps) in 5.20(b).

raster, we also calculated the coefficients a_{ij} with the solid angle model (that is, after this calculation, we now have two rasters). We normalized the coefficients of both rasters with the respective maximum value. Finally we calculated the relative error of the solid angle model with respect to the probe readings in the following manner:

$$\epsilon\left(d_h, d_v\right) = \frac{\left|a_{sa}\left(d_h, d_v\right) - a_{lut}\left(d_h, d_v\right)\right|}{a_{raster}\left(d_h, d_v\right)} \tag{5.16}$$

where $a_{sa}\left(d_h, d_v\right)$ and $a_{raster}\left(d_h, d_v\right)$ are the coefficient values for respectively the solid angle model and the raster generated from probe readings for the position dictated by d_h and d_v. The distribution of the relative errors can be seen in figure 5.20(a). Note that the solid angle produces 100 % relative error in the upper triangular region due to the FOV–cut. This error is however not relevant, due to the fact that the probe readings are almost zero in this region, as seen in 5.20(b). However on the other hand, the solid angle is moderately accurate only in the right corner of the lower triangular region, up to a few mm, and in the rest of this region produces an error of about 60 % even in relatively small distances like $5\ mm$ [Shak 12a].

5.5.2. Look–up table (LUT) model

Instead of calculating the coefficients a_{ij} directly with a mathematical formula, it is also possible to calculate them based on a raster like the one mentioned above. In acquiring such a raster, a symmetric probe construction (e.g. cylinder) can be exploited such that only a 2D raster of probe reading–position pairs is obtained,

and then mirrored around the probe axis. As our probe fits into this category, we base the rest of our discussion on this type of rasters.

A raster as such can be conceptualized as a *look–up table (LUT)* $L : \mathbb{R} \times \mathbb{R} \rightarrow \mathbb{R}$, mapping from the 2D horizontal and vertical distance values (d_h and d_v) to a probe reading value. Our models calculate the (direct) detector–to–source distance d_{ij} and the detector–to–source angle α_{ij}, which cannot be directly used for retrieving the corresponding coefficient value a_{ij} from this type of LUT. Instead, a function $f = f(d_{ij}, \alpha_{ij})$ takes the d_{ij} and α_{ij} values, and calculates the corresponding d_h and d_v. In case there is no direct match to the discrete horizontal and vertical distance values of the LUT, f returns two *sets* of such distances $\{d_h\}$ and $\{d_v\}$: $f : \mathbb{R} \times [0, \pi/2] \rightarrow \mathbb{R} \times \mathbb{R}$. The LUT function L then takes these distance values as parameters and returns the corresponding coefficient a_{ij} in the case the LUT has exactly matching d_h and d_v values (i.e. one value in each of both sets). Otherwise, i.e. if there is no exact match, L computes the value a_{ij} by performing (e.g. nine–neighborhood) interpolation between the values of the distance value sets $\{d_h\}$ and $\{d_v\}$. In summary, the LUT probe model calculates a coefficient a_{ij} as:

$$a_{ij} = a(d_{ij}, \alpha_{ij}) = L(f(d_{ij}, \alpha_{ij})) \tag{5.17}$$

We used the same datasets from the probe model study as mentioned above for evaluating the LUT model as well and ran reconstructions using these. The reconstructed images can be seen in figure 5.21. The numerical correlation values to ground truth can be seen in figure 5.15 [Shak 12a].

5.5.3. LUT–fitting analytical model

Another approach to ad–hoc models of detection we have tried is to fit a heuristical analytical formula to an LUT. The advantage of this approach is that it eliminates the need for interpolation in case the exact position is not found within the LUT. The following is an exemplary formula we came up with, that can be used to analytically describe the relation between the geometric parameters and the probe reading obtained for each combination of these parameters:

$$a_{ij} = a(d_{ij}, \alpha_{ij}) = \frac{cos(\alpha_{ij})}{(d_{ij})^p} \tag{5.18}$$

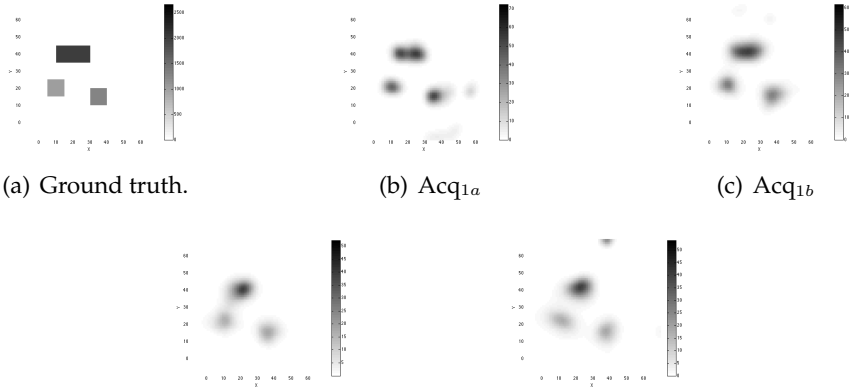

(a) Ground truth. (b) Acq_{1a} (c) Acq_{1b}

(d) Acq_{3a} (e) Acq_{3b}

Figure 5.21.: Model study phantom: reconstructions with the LUT model.

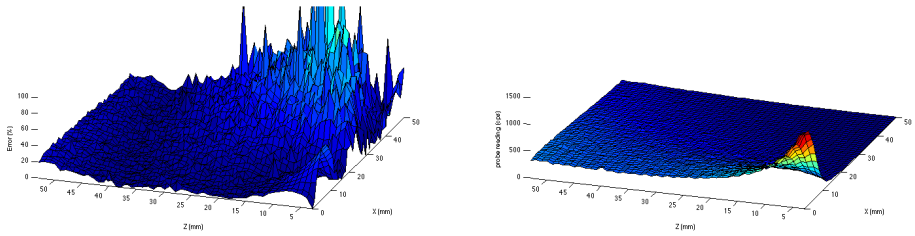

(a) Relative error of the LUT–fitting analytic model.

(b) Actual LUT values.

Figure 5.22.: Coefficients calculated using the LUT–fitted analytical model vs. the look–up table of probe readings. **x–axis:** d_h values, **y–axis:** d_v values (both in mm), **z–axis:** relative error values as a percentage in 5.22(a); probe readings (counts per second – cps) in 5.22(b).

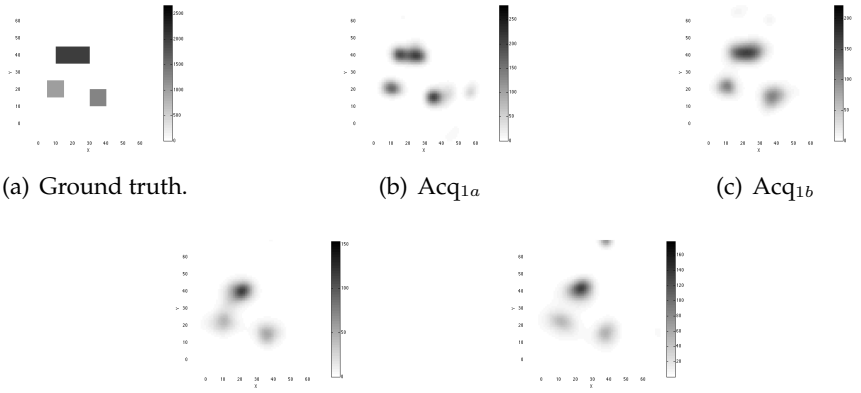

(a) Ground truth. (b) Acq_{1a} (c) Acq_{1b}

(d) Acq_{3a} (e) Acq_{3b}

Figure 5.23.: Model study phantom: reconstructions with the LUT–fitted analytical model.

The power p to which the probe detector–to–source distance d_{ij} is raised is calculated using the formula:

$$p_{ij} = p\left(d_{ij}, d_{max}, \alpha_{ij}\right) = b + w_1 \left(cos\left(\alpha_{ij}\right) \frac{d_{ij}}{d_{max}}\right) - w_2 \left(\frac{d_{max} - d_{ij}}{d_{max}}\right) \tag{5.19}$$

In this equation b is the basis power. w_1, w_2 provide options for varying the total power to which d_{ij} is raised. The term $w_1 \left(cos\left(\alpha_{ij}\right) \frac{d_{ij}}{d_{max}}\right)$ penalizes large distances, whereas the term $w_2 \left(\frac{d_{max} - d_{ij}}{d_{max}}\right)$ makes coefficients even higher at smaller distances [Shak 12a]. In a manner similar to the solid angle model mentioned above, we quanitified the relative error of this LUT–fitting analytical model for each LUT position. The error distribution can be seen in figure 5.22. The LUT–fitting analytic model produces more than 100 % relative error in the upper triangular region, similar to the solid angle model, but in a smaller area. This error is again not relevant, due to the fact that the probe readings are almost zero in this region (see figure 5.22(b)). However on the other hand, the LUT–fitted analytic model does not have so large error values as the solid angle model in the actually relevant region. The maximum error in this region is about 20 %.

We present the images reconstructed from the model study phantom data using the LUT–fitted analytical model in figure 5.23. The numerical correlation values to ground truth can be seen in figure 5.15 [Shak 12a].

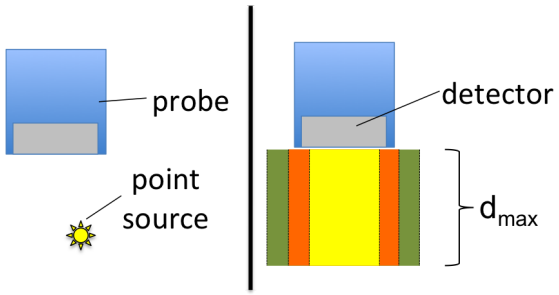

Figure 5.24.: Illustration of an exemplary partitioning scheme for the partition model. The left image shows the position of a hypothetical radioactive point source with respect to the probe. The right image shows the three partitions of the probe FOV (cylindrical in this case rather than conic), each encoded in a different color. d_{max} is the maximum vertical distance up to which a point source is considered: beyond d_{max}, the probe is assumed to be insensitive.

5.5.4. Partition model

A beta probe is very sensitive to radiation when in very close vicinity of a source within its FOV, however as soon as the source is out of the FOV, the probe reading drops dramatically (see for instance in figure 5.22(b) the region out of the probe FOV, that is $x > 5\ mm$). Hence our experience is that an efficient way for computing the coefficients a_{ij} is by dividing the probe FOV into partitions and then assigning a particular homogeneous weighting factor for each partition. Figure 5.24 illustrates an exemplary partitioning scheme. As the probe detector–to–source distance d_{ij} is mostly within the millimetric range, this approach could also minimize a cascading effect on the magnitude of error due to possible inaccuracies in the geometric surface model and the spatial localization error. This probe model translates analytically the following formula:

$$a_{ij} = a\left(d_{ij}, d_{max}, \alpha_{ij}\right) = \begin{cases} a_p & \text{source within partition } p \\ 0 & \text{source not within any partition} \end{cases} \tag{5.20}$$

As the detector is practically insensitive to sources more distant than a particular vertical distance value, d_{max} is used for limiting the probe FOV vertically along the probe axis. The relative error of this new model with respect to the LUT can be seen in figure 5.25. Note that at lower distances the error is low, whereas it increases with distance.

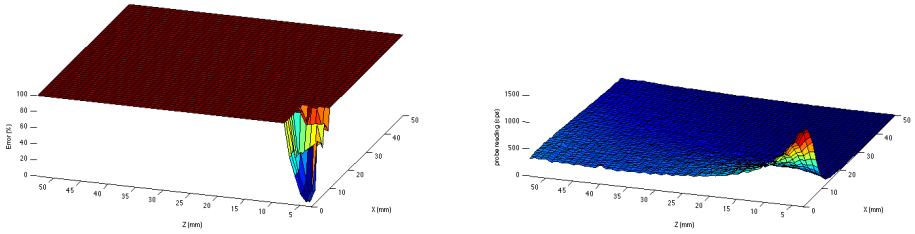

(a) Relative error values of the partition probe model.

(b) Actual LUT values.

Figure 5.25.: Coefficients calculated using the partition model vs. the look–up table of probe readings. **x–axis:** d_h values, **y–axis:** d_v values (both in mm), **z–axis:** relative error values as a percentage in 5.25(a); probe readings (counts per second – cps) in 5.25(b).

5.5.5. Role of simulation

Simulation in the realm of state–of–the–art nuclear imaging is fairly popular. For instance Monte Carlo simulations are performed for determining and optimizing the system matrix that mathematically describes a PET tomograph geometry [Read 07]. Especially the well established GATE simulation framework presented in [Stru 03] is used for simulating detector geometries. Therefore it can be used for studying precisely the capabilities and limitations of a specific imaging system design in a very controlled environment, even before building that system physically. This constitutes the major advantage of simulation. Furthermore, simulation avoids unnecesary exposure to ionizing radiation (e.g. while preparing a phantom).

In order to better understand the impact of our ad–hoc models in the imaging process, we made an attempt to simulate our beta probe measurements using GATE. For this simulation, we used the probe construction geometry, as well as the already known phantom geometry and the tracking data from our four datasets of the probe model study. Contrary to our expectations, the simulated probe readings yielded very low correlation to the actual probe readings (see figure 5.16).

The images reconstructed with the probe readings simulated by GATE, and using the solid angle model can be seen in figure 5.26. The correlation values of these images to the ground are listed in figure 5.18. Neither of these results suggest any realiable correlation between the simulations and the ground truth. We can only speculate here that GATE, which is well established for simulating radi-

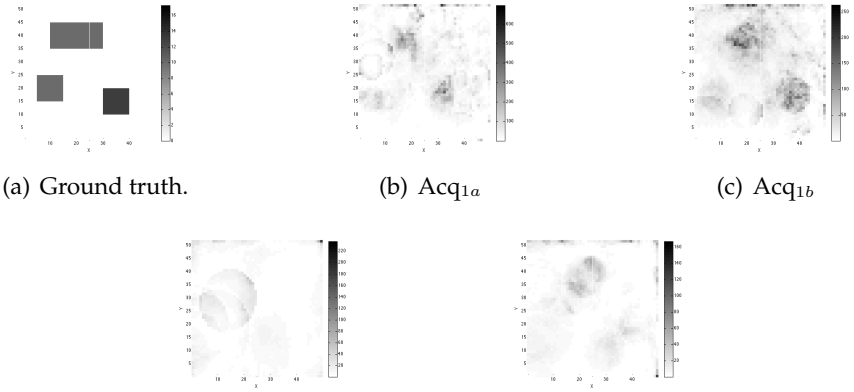

(a) Ground truth. (b) Acq_{1a} (c) Acq_{1b}

(d) Acq_{3a} (e) Acq_{3b}

Figure 5.26.: Model study phantom: reconstructions with the solid angle model (using the probe readings simulated using GATE).

ation detection for photons, is not suited (or maybe *not optimized* is a better word) for simulating radiation detection for positrons. This could be the reason why there is for practical purposes no correlation between the measurements nor the reconstructions [Shak 11a].

5.6. Experimental Neurosurgical Feasibility Studies

PROVING the technical feasibility of our system before moving on to pre–clinical and clinical studies is an obligatory step. The flat phantom studies as well as the probe model calibration setups we have shown above are one part of the whole story for the investigation of the various parameters relevant to the imaging process. Another important aspect is to prove the feasibility of epiphanography on realistic phantom setups, which provide the opportunity for testing the system in simulated real–life scenarios within a controlled experimental environment. In this section we present the two phantom studies we have conducted in the context of introducing our system for use in neurosurgery.

5.6.1. Realistic neurosurgical phantom study I

For this study we prepared a phantom mimicking an open brain surgery with a radiotracer like [^{18}F]FET pre–operatively administered in the patient.

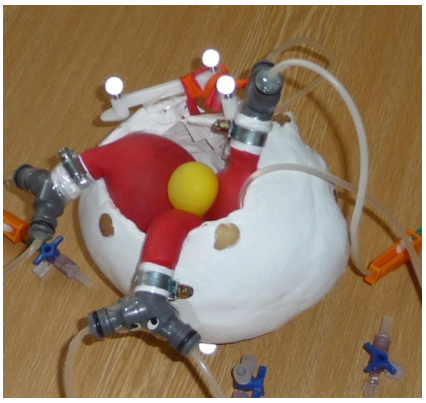

Figure 5.27.: The first open neurosurgery mimicking phantom. The red balloons emulate healthy brain tissue with background activity, while the yellow balloon emulates a tumor lesion. Note that the optical tracking target is rigidly attached.

5.6.1.1. Experiment setup

We had a skull model fabricated from the CT image of a real skull as a template, keeping the right side open to mimick an open brain surgery. To simulate the brain tissue along with a tumor lesion (as far as radiotracer uptake is concerned), we inserted three balloons inside this skull model and inflated them with water. We inflated a smaller balloon among these three in order to emulate a tumor lesion within healthy peri–tumoral tissue. There are two motivations for this setup with balloons. First of all, balloons configured in this way provide a semi–realistic surgical cavity (with respect to the arbitrariness of the surface) with an exposed surface. Secondly, our assumption is that the radioactive fluid is distributed homogeneously inside a balloon, and therefore we can be sure to have a homogeneous amount of activity on its surface. One drawback of this approach however is that there is a loss of the continuity of surface between two balloons. Another issue that could be raised is the permeability of the balloon material to positrons. For this second issue, we assume that there is no critical loss of positrons, based on the experimental observations of Singh *et al.* in [Sing 09].

After preparing our initial setup with the water–inflated balloons, we injected [^{18}F]FDG into each balloon proportional to its volume, so as to obtain a T/B activity ratio of 20:1. The phantom can be seen in figure 5.27.

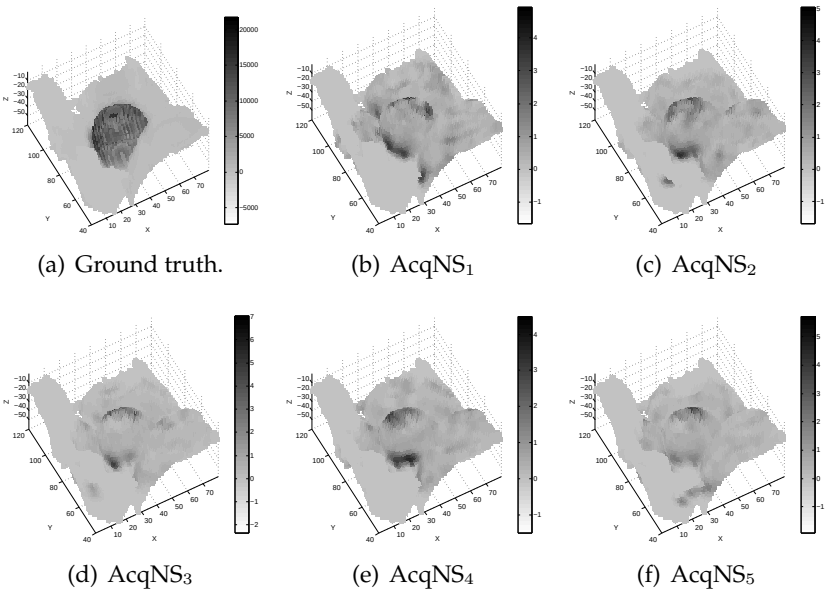

(a) Ground truth. (b) AcqNS$_1$ (c) AcqNS$_2$

(d) AcqNS$_3$ (e) AcqNS$_4$ (f) AcqNS$_5$

Figure 5.28.: First neurosugery phantom: reconstructions with the solid angle model.

5.6.1.2. Experiment protocol

Before scanning the phantom with our system, we obtained its PET/CT image with the tracking target already fixed on it (see figure 5.27) during the PET/CT acquisition. The purpose of fixing the tracking target is to provide a common reference coordinate system to register the PET/CT data to the epiphanography images. Following the PET/CT acquisition, we obtained five freehand epiphanography scans (enumerated AcqNS$_1$ through AcqNS$_5$). Each of these datasets consists of about 5,000 measurements (taking approximately $5\ min$ to acquire the data).

5.6.1.3. Evaluation & results

We segmented the balloon profiles seen in each CT slice using the *multiphase soft segmentation with total variation and H1 regularization* approach outlined in [Li 10] to generate the surface of the phantom[9]. We manually selected the region of interest (ROI), including the scanned surface, within the CT image frame. Within this

[9]We would like to acknowledge Dr. Maximilian Baust for kindly providing the implementation of this segmentation algorithm and configuring the relevant parameters for optimally segmenting the balloon profiles.

selected ROI, we obtained the surface profile by simple edge detection in the segmentation. We then stacked the surface profile from each CT slice within the ROI to form a 3D model of the surface. This model serves as the suxel basis function for the reconstruction part of epiphanography. As ground truth, we extracted the activity values from the PET data corresponding to the locations of the suxels of this surface model.

In order to compare the epiphanography images to the ground truth image with activities obtained from PET, these two had to be registered. We did this by fitting a coordinate system to the optical tracking target. For that purpose, we manually segmented the three fiducials of the tracking target (see figure 5.27) from the CT slices. Later we fitted a coordinate system on to their centroids. Finally, we transformed the extracted coordinates from the PET/CT coordinate system onto the tracking target coordinate system, thereby providing a common reference to compare the epiphanography images to the ground truth.

All reconstructions as well as the ground truth image can be seen in figure 5.28. We calculated the correlation of the epiphanography image obtained from each of the five datasets to the obtained ground truth surface activity. In addition, we calculated the T/B signal ratio of each by averaging all the activities within the tumor and background regions respectively (we performed tumor/background segmentation by manual thresholding of the ground truth image). Figure 5.29 shows these numeric results. The ground truth T/B ratio (i.e. in PET images) was around 30:1 and T/B in the epiphanography images was around 7:1 [Shak 11b].

5.6.2. Realistic neurosurgical phantom study II

Although the first phantom study outlined in the previous section was realistic in terms of simulating a surgical cavity with an arbitrary surface, it has the major shortcoming of not having a reproducible geometry. In addition, the tumor lesion emulation does not really correspond to a realistic residual tumor mass in terms of size. Furthermore the T/B activity ratio of 20:1 was much higher than what could be expected in a real surgery. In our second open neurosurgery–mimicking phantom study, we aimed at overcoming the geometric deficiency by preparing a phantom with realistic–size, and reproducible post–resection residual tumor deposits within the surgical cavity. Regarding the activity concentration aspect, we aimed at varying the T/B ratio in order to see the capabilities and limitations of epiphanography in a neurosurgical setup.

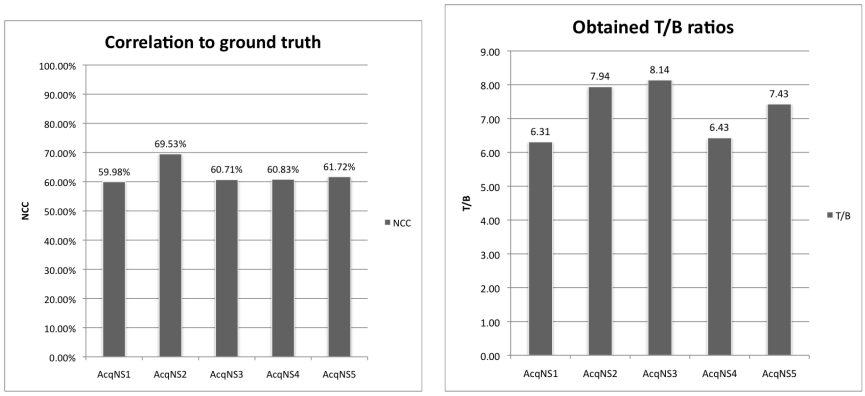

(a) NCC (b) T/B

Figure 5.29.: Numerical results of the evaluation of the reconstructions in figure 5.28 to the ground truth.

5.6.2.1. Experiment setup

We glued a compact disc (CD) box inside a mixing bowl, after inserting an inlet and an outlet to the CD box allowing for radioactive fluid injection. Following that we poured agar over and around this CD box to fill all the empty volume around it. We covered the agar and the CD box surface with silicon for improving rigidity. Finally we attached a *96 well microplate* (referred to simply as *well plate* from this point on) with *wells* of ø $6.96\ mm$ on top of this construction (see figure 5.30). Please note that our primary interest is the residual tumor emulations on the microwell plate, and that in the ideal case the radioactive fluid within the CD box (termed *deep background – DBG* from here on) should contribute nothing to this experiment. Nevertheless, as our beta probe obtains the net positron count by a weighted subtraction of the gamma ray signal from the combined gamma and positron signal [Dagh 94], we conducted all the experiments with and without this DBG radioactivity, in order to find out the effect of this radiation in a realistic setting. For a realistic setup based on the whole–body distribution of [^{18}F]FET reported in [Paul 03], we injected $5\ MBq$ of activity into the CD box. We simulated residual tumor masses in three different geometric configurations featuring one, two and three holes of the well plate filled with ^{18}F fluid (i.e. one, two and three hot spots, see the ground truth image illustrations in figure 5.32(a), figure 5.32(d), and figure 5.32(g) respectively), and four different T/B configurations. In one of these four, we used no background activity, in the remaining three we produced

Figure 5.30.: The second open neurosurgery–mimicking phantom.

T/B ratios of 8:1, 4:1 and 2:1 respectively.

5.6.2.2. Experiment protocol

Two operators scanned the phantom with the epiphanography system to obtain three datasets per phantom configuration. Each dataset consisted of approximately 1,500 measurements (approximately $3\ min$ of scanning). This was the first set of experiments in which the data acquisition was performed using our new ***Nu**clear **I**ntra–**o**perative **Na**vigation (**NuIoNa**)* software framework outlined in appendix C.

5.6.2.3. Evaluation & results

After performing all the experiments, we attempted to reconstruct images with all the datasets. However, being unable to get any viable image from any dataset, we decided to analyze the data we had obtained. While scanning the phantom, we had been visually observing that the highest probe readings were recorded with the probe directly on top of the hot–spots. This was however not the case when we plotted the raw probe readings on to the ground truth images using the tracking data. Therefore we decided to try to see whether a systematic temporal shift would lead all the datasets to have their highest probe readings on top of the hot–spots. We found out that a systematic shift of $58\ sec$ achieves this goal on all but very few datasets. From this analysis we concluded that this phenomenon is caused by a bug in the **NuIoNa** software framework, and discarded the corresponding $58\ sec$ data from each dataset. Such a delay is unthinkable in terms

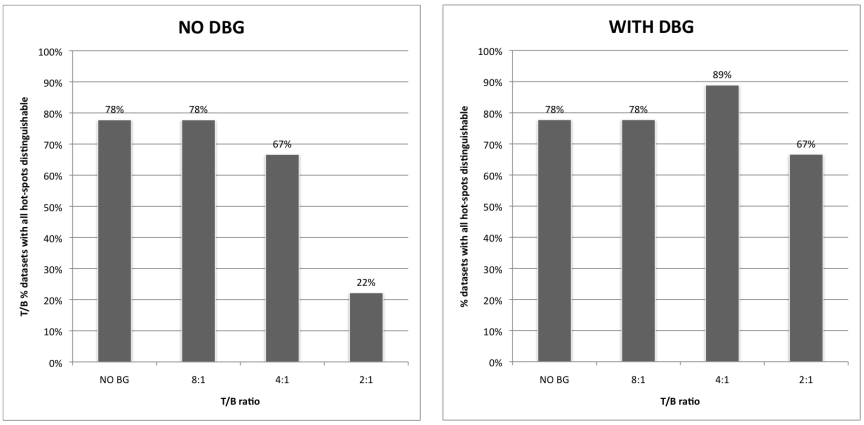

(a) No DBG. (b) With DBG.

Figure 5.31.: Hot–spot distinguishability in reconstructions of the second neurosurgery phantom datasets. The y–axis shows the percentage of the datasets in which all hot–spots are distinguishable.

of the CPU processing or network communication timeframes. Nevertheless, our software framework has its own buffered data accumulation mechanism, which is probably the place where the bug is located.

We reconstructed epiphanography images with the partition model presented in section 5.5.4, applying MLEM with 25 iterations, and smoothed each reconstruction with a 3 mm Gaussian kernel. We managed to get visually correct reconstructions for all the spatial phantom configurations. Figure 5.32 shows a good as well as bad reconstruction for each spatial configuration. As expected, when the T/B ratio goes lower, the quality of the images decreases and it becomes hard to distinguish the hot–spots. All the reconstructions from this study can be seen in appendix B. One thing worth noting here is that in almost all spatial and T/B configurations, the addition of the DBG has a positive effect on the resulting images in terms of the distinguishability of the hot–spots (compare the hot–spot distinguishability percentages – esp. with T/B 4:1 and 2:1 between figure 5.31(a) and figure 5.31(b)). This is a positive outcome, as background activity on the order of the magnitude of the DBG is definitely to be expected in a real–life scenario. We qualitatively evaluated the distinguishability of the hot–spots in each reconstructed image. The results can be seen in figure 5.31.

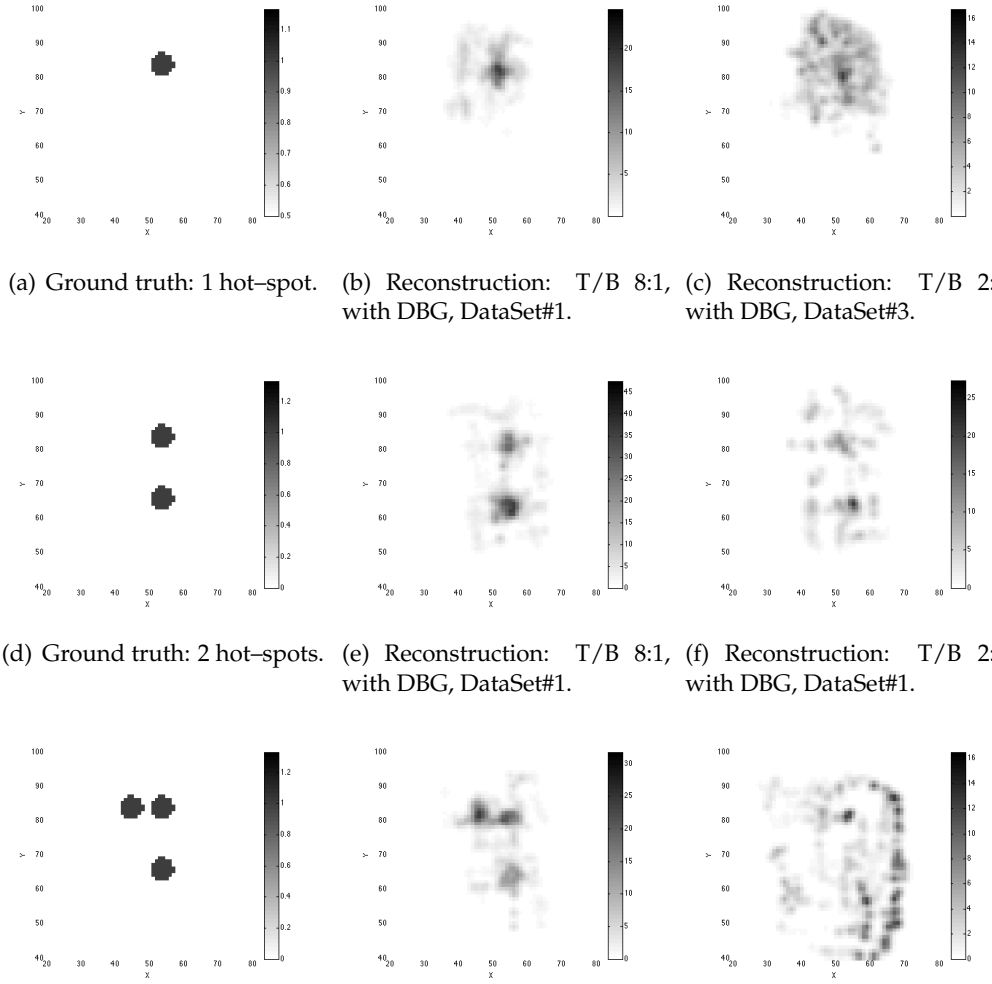

(a) Ground truth: 1 hot–spot. (b) Reconstruction: T/B 8:1, with DBG, DataSet#1. (c) Reconstruction: T/B 2:1, with DBG, DataSet#3.

(d) Ground truth: 2 hot–spots. (e) Reconstruction: T/B 8:1, with DBG, DataSet#1. (f) Reconstruction: T/B 2:1, with DBG, DataSet#1.

(g) Ground truth: 3 hot–spots. (h) Reconstruction: T/B 8:1, with DBG, DataSet#3. (i) Reconstruction: T/B 2:1, with DBG, DataSet#2.

Figure 5.32.: Selected reconstruction images from the second neurosurgical phantom study. **Left column:** ground truths. **Middle column:** good reconstructions. **Right column:** bad reconstructions.

5.7. Discussion

THE idea of controlling tumor resection margins via intra–operative imaging in radio–guided surgery came about in the early 80s, after high–contrast PET–images of brain tumors with ^{18}F*–fluorodeoxyuridine* were obtained. However the heavy and bulky shielding needed in order to confine the field–of–view of a probe (due to the high penetration of $511\ keV$ annihilation gammas) was the bottleneck to the implementation of this idea by gamma detection, until Daghighian *et al.* came up with the idea of detecting positrons directly [Hoff 04]. As presented in section 4.1, the technology has evolved since then, and today devices are out or just a final step away from being in the market, that make it possible to obtain a 2D image of the positron distribution of a surface just within seconds. Compared to beta probes, these devices have the advantage of delivering an image rather than a simple count rate.

Our approach is somewhere between beta probes and beta cameras: the whole area of interest is to be scanned with a beta probe in order to deliver an image thereof. Within our approach it could be of great advantage to use a beta camera instead of a beta probe, though: in the same timeframe that it would take to cover the whole region with a beta probe, much more data could be collected with a beta camera, leading to improved statistics. Nevertheless, most of the current beta cameras are too bulky to be used in such a setting, especially when the tumor bed to be scanned is rather small in size, the beta probe has much less limitation than a beta camera. Devices like the fingertip imager of Stolin *et al.* or even the RMD imaging beta probe could be good candidates to replace the beta probe, though.

We have presented in this thesis the technical system design, with a focus on the different ad–hoc detection models we have tried so far. A significant part of our work, although not visible in the scientific portion of the text, has been in laying down the foundations of a large–scale modular software framework for data acquisition, reconstruction using the ad–hoc models, and visualization. We call this framework ***Nu**clear **I**ntra–**o**perative **Na**vigation (**NuIoNa**)*. A short guideline to working with and further developing **NuIoNa** can be found in appendix C. In particular, **NuIoNa** provides support for generating arbitrary–shaped surface models from an irregular scattered point cloud: an accurate geometric model of the surface is a crucial aspect of epiphanography, as discussed in section 5.2.3.

The validation of epiphanography on phantoms before moving to pre–clinical and later to clinical studies is mandatory due to the use of radiotracers, in addition

to the potential invasiveness associated with it (i.e. the need for scanning the tumor cavity surface by almost touching it with the beta probe). Therefore in order to put epiphanography into the context of the neurosurgical treatment of LGGs, we have made an attempt to go from simplistic 2D phantoms towards more realistic 3D phantoms. Our phantom studies in that respect demonstrate in a controlled experimental setup the feasibility of epiphanography in neurosurgical applications. The main advantage of the first phantom outlined in section 5.6.1 is the arbitrary surface, while its main disadvantage is the geometric irreproducibility. On the other hand, the main advantage of the second phantom outlined in section 5.6.2 is the high reproducibility, while its main disadvantage is the unrealistic surface with respect to the curvature and soft tissue associated with a tumor cavity. This phantom also makes it possible to use close–to–realistic orders of magnitude of radioactive fluid, therefore emulating a realistic scenario. In addition, the well plate is a perfect model serving the purpose of a well–defined ground truth. Moreover, thanks to the support for arbitrary surface models within our software framework, these results obtained with this flat surface should be applicable to phantoms with more realistic surfaces.

We found out that to make realistic phantoms is a real challenge, mainly due to two major issues. First, due to the fact that even very thin material can stop a lot of positrons (i.e. from ever reaching the detector), it is crucial that the surface of the actual radioactive material be either exposed or covered with a material that will allow at least a major portion of positrons to pass without annihilation and with minimal energy loss. In case of an exposed surface, scanning with a probe/camera becomes a real nuisance: the detector must be held very close to the surface and yet *without* touching it, in order to avoid contamination of the device. In an intra–operative scenario, the beta probe/camera is to be covered with sterile latex sheathing, which avoids a direct contamination of the device itself. Yet, if and after the latex sheathing has touched the scan surface (even only once), it *is* contaminated. As this is an inevitable issue, possible remedies can be suggested, such as updating the probe's/camera's background signal setting several times *during* the (actually quite short) scan. In addition, the contribution of the latex sheathing to the loss in the signal (due to the attenuation of positrons) is also questionable, although it is reported to be minimal (see [Sing 09]). The second issue in a phantom study involving positron detection is about the dosing of radioactivity: realistic activities estimated from patient data are in the range of kBq rather than MBq. This first of all made the preparation of the radioactive

fluid to inject into phantoms very difficult, due to the fact that the measurement equipment we have in the Department of Nuclear Medicine is tuned for patient studies (typically tens to hundreds of MBq). Secondly, due to the relatively short half–life of ^{18}F, the timeframe to obtain viable data is limited. All these issues make it extremely difficult to configure a realistic 3D phantom in a reproducible setting.

Some of the issues discussed apply directly to the intra–operative setting in a clinical scenario. Therefore the technology of navigated intra–operative imaging with beta probes/cameras has still a not very short way to go before becoming mature enough for everyday clinical application. One could even pose the question whether it is not better to use a non–radio–guided approach for controlling resection margins in cancer surgery, in the light of new contrast agents like *5–Aminolevulinic acid (5–ALA)*. Although the answer to this question may be straightforward for some scenarios, it is not trivial for LGGs. Fluorescence imaging with 5–ALA has been used for intra–operatively imaging HGG residuals [Roes 12], albeit with low resection accuracy [Panc 12]. Roberts *et al.* on the other hand report that 5–ALA can potentially be intra–operatively useful for LGGs in conjunction with quantitative fluorescence [Robe 12]. Another study reports that fluorescence lifetime spectroscopy can intra–operatively detect LGGs with perfect sensitivity and specificity [Butt 11]. Other intra-operative ultrasound–based methods like *guided elastography* and 2D imaging can also be used to distinguish resectable tissue and internal tumor structures, however these techniques suffer from low resolution and presence of acoustic noise artifacts [Gerg 11, Selb 12].

CHAPTER 6

Intra–operative PET

In this chapter we present our work on the *freehand PET* imaging modality for intra–operative use. The word *PET* is almost synonymous with *coincidence detection*. Therefore technically speaking, our imaging modality is rather *freehand high–energy single photon emission computed tomography (SPECT)*. Nonetheless, as we aim at imaging the volumetric distribution of positron–emitting radiotracers – with different challenges compared to the freehand SPECT modality that works in conjunction with single gamma emitters, we call our imaging modality *freehand PET (fhPET)*. Our fhPET imaging modality takes the high–energy probe technology introduced in section 4.2.1 one step further by adding tracking towards a navigated solution, and generating images with non–imaging probes. However compared to the novel imaging technologies introduced in section 4.2.2, fhPET is one step behind, that is coincidence detection, and hence improved resolution (at least in theory). The main advantage of a setup like ours is the exclusion of a second detector block (e.g. to be placed under the patient), and therefore the elimination of a potentially bulky construction.

In the current chapter we first introduce the medical relevance of fhPET in the context of head and neck squamous cell carcinoma (HNSCC). After that we elaborate on the general design and setup of our system. Following that we present the ad–hoc detection model we employ for imaging. Then we present the feasibility study conducted with a realistic neck phantom. Finally we talk about our first experience with fhPET in the OR and conclude with a discussion of our results.

Acknowledgements and publications

Ad–hoc detection model in section 6.3: in collaboration with Alexander Hartl; published in [Shak 12b]. Probe specifications courtesy of Dr. Farhad Daghighian.

HNSCC phantom study in section 6.4: under medical supervision of Prof. Dr. Markus Essler[2]; in collaboration with Aslı Okur[1,2], and Philipp Matthies[1]; published in [Shak 12b, Okur 13].

First experience in the OR in section 6.5: under medical supervision of PD Dr. Marc Martignoni[4], Prof. Dr. Klemens Scheidhauer[2]; in collaboration with Aslı Okur[1,2], and Philipp Matthies[1].

All publications: under the scientific supervision of Dr. Tobias Lasser[1,3], supported by the SFB 824 (DFG, Germany), the Graduate School of Information Science in Health (GSISH), and the TUM Graduate School (Munich, Germany).

Affiliations

1 Computer Aided Medical Procedures (CAMP), Technische Universität München, Munich, Germany

2 Department of Nuclear Medicine, Klinikum rechts der Isar, Munich, Germany

3 Institute of Biomathematics and Biometry, HelmholtzZentrum München, Germany

4 Department of Surgery, Klinikum rechts der Isar, Munich, Germany

6.1. Medical Relevance

HEAD and neck squamous (epithelial) cell carcinoma (HNSCC) is diagnosed in 500,000 patients world–wide each year. HNSCC primarily affects the oropharynx, oral cavity, hypopharynx, and larynx; but has a risk of metastasizing into the *cervical* lymph nodes (LN), i.e. the LNs in the *cervix* (neck) [Hadd 08]. While the general *five-year survival rate* for HNSCC is reported to be 67.9 %, in the presence of cervical LN metastases, it goes down to 31 % [Whit 77]. It is therefore important for prognosis to assess the status of these LNs and to remove the ones containing metastases.

The aim of the surgical treatment option in HNSCC is to completely resect the tumor and all LN metastases. However the micro–presence of metastatic cells in a specific cervical LN cannot be excluded with any state–of–the–art imaging modality. In addition, the intra–operative localization of all suspicious LNs is difficult. Therefore, in practice the surgeon resects all the LNs that he can find (this procedure is called *modified radical neck dissection*). The number of resected LNs is a measure of the quality of the surgery, as the probability for a residual metastatic LN decreases. The resection of the primary tumor is not a very difficult task, as the *ear, nose and throat (ENT)* specialist sees the tumor easily. In addition, the lymphatic paths in the cervical region are well–known. Therefore there is no indication for intra–operative radio–guidance in the primary tumor surgery.

Due to the mentioned poor prognosis of HNSCC in the presence of cervical LN metastases, patients are routinely examined with ultrasound (US) in three–month periods following the primary tumor surgery. Enlarged LNs in the US examination are indications for PET/CT imaging. Recurrent tumor is visible in the PET/CT images. However the surgery is extremely restricted in the case of recurrent tumor, mainly due to the large tissue loss caused by the primary surgery. Furthermore, plastic surgery is required in most cases due to the fact that in the primary tumor surgery some of the muscles and cervical tissue have been removed; that is, the neck has become very thin.

In recurrent tumor surgery the aim is to resect the usually very few metastatic LNs, targeting the best post–operative quality of life. The few metastatic LNs, which are visible in the PET/CT images, are hard to localize intra–operatively. It would therefore be very desirable from the surgeon's point of view to pinpoint those few LNs intra–operatively, such that the surgical incision can be kept minimal. This also has the benefit that as little muscle from the chest area has to be shifted to the cervical area to compensate for the removed tissue. In other words, the plastic surgery needed in recurrent HNSCC becomes less of a challenge. Apart from aesthetic motivations, surgeries in the head and neck region are a sensitive case due to the high risk of post–operative morbidity resulting from the presence of vital anatomic structures. Thus it is of high clinical relevance to intra–operatively guide the surgeon to pinpoint and resect the few metastatic LNs, especially when critical structures such as nerves or vessels make the resection difficult.

[^{18}F]FDG–PET was found to detect cervical LN metastases with the highest sensitivity and specificity, compared to other state–of–the–art pre–operative imaging

methods (CT, MRI, US) [Adam 98]. In that respect, fhPET could be used intra–operatively in a navigated setup in order to guide the surgeon in pinpointing the few [^{18}F]FDG–PET–positive LNs targeted for resection in recurrent HNSCC surgery.

6.2. Design & System Setup

6.2.1. General system setup

Our system combines a high–energy gamma probe (*NodeSeeker 800, Intra Medical Imaging LLC, Los Angeles, CA, USA*), and an optical tracking system (*Polaris Vicra, Northern Digital Incorporated, Waterloo, ON, Canada*). Both the tracking system, as well as the control unit of the probe can be seen in figure 5.1(a). We already presented information about the tracking system in section 5.2.1.2. The following subsection gives brief information about the high–energy gamma probe.

6.2.1.1. High–energy gamma probe (HE probe)

A *high–energy gamma probe (HE probe)* is a pen–sized, hand–held device, typically with a big shielding head around the detector (see figure 6.1), that can detect (annihilation) gamma rays. Annihilation gamma rays have large kinetic energy, and can therefore substantially penetrate matter. Therefore in order to be able to narrow the field of view (FOV) of a HE probe, there is need for a thick shielding material around the detector. This is the rationale behind the big *head* of the probe. Contrary to PET systems, which are based on hardware that can detect such simultaneous gamma rays (*coincidences*), a HE probe does not detect coincidences, but only single $511\ keV$ gamma rays. The calibration of the HE probe detector follows a similar path as the one described for the beta probe in section 5.2.1.1, with the *mutual detector sensitivity estimation* step omitted.

6.2.2. Tomographic imaging with HE probes

A HE probe gives a 1D signal, proportional to the total amount of energy deposited by gamma rays in the detector material within one detection window. Therefore a HE probe is by itself not sufficient for generating 3D (tomographic) images. Along the line of epiphanographic imaging with beta probes outlined in section 5.2.2, combining a HE probe with spatial localization system makes it possi-

Figure 6.1.: Gamma probes. **Top:** high–energy ($511\ keV$) gamma probe. **Bottom:** $140\ keV$ gamma probe.

ble to synchronously record the respective data from both devices. This opens the way for imaging the volumetric distribution of a radiotracer like [^{18}F]FDG with a proper ad–hoc detection model (for the details of the mathematical foundations, refer to section 3.3 and section 5.2.2). In principle, we apply a decomposition of the probe measurements like in equation 3.8:

$$m_i = \sum_j a_{ij}\ c_j$$

We call our system *freehand PET (fhPET)*, despite the fact that it is not based on coincidence detection as in a real PET tomograph. Yet our system works in conjunction with positron–emitting radiotracers like [^{18}F]FDG, and hence performs in a sense *positron emission tomography*. Our system is conceptually the same as the *freehand SPECT (fhSPECT)* system, which has been proposed for the first time in [Wend 07]. The fhSPECT technology and the medical application thereof are coupled to single gamma emitter isotopes like ^{99m}Tc with much lower energies compared to positron emitters like [^{18}F]FDG (compare the $140\ keV$ gammas of ^{99m}Tc to the $511\ keV$ annihilation gammas of ^{18}F). The latter presents more challenges for the ad–hoc detection modeling and the actual workflow. These are the major differences, which we explain in the next subsection.

6.2.3. Challenges & limitations

As already mentioned above, our system is conceptually the same as fhSPECT. However accurate modeling of the detection of high–energy gamma rays poses additional challenges. One big problem is that due to the high energy levels

($511\ keV$), gamma rays from positron emitters can penetrate through matter more than the $140\ keV$ gamma rays of ^{99m}Tc. Thus, a HE probe is usually equipped with much thicker shielding than a low–energy gamma probe, which can still not stop all the gammas.

Another severely restricting problem is due to the differences in radiotracer physiology. As mentioned in section 3.1.1, [^{18}F]FDG is a glucose analog; thus it is coupled to the glucose metabolism. And because glucose is transported to the body cells via the bloodstream, [^{18}F]FDG is administered to the patient by a systematic intravenous injection. Due to this fact, [^{18}F]FDG is taken up by any cells reachable through the bloodstream, and is hence quite unspecific. This means high background radioactivity, which can actually *shadow* the structures of interest within the region of interest at the time of scanning. To make a concrete comparison, in the case of e.g. ^{99m}Tc–labeled radiotracers used in *sentinel lymph node biopsy imaging (SLNB)* (see [Blue 13]), there is almost *no* unspecific uptake due to the peri–tumoral injection of the radiotracer. The background uptake e.g. in the case of SLNB is usually a very big blob of radioactive region around the injection site. The extent of this region however can be anticipated and therefore effectively excluded from the scan region. In other words, it can be prevented from *shadowing* the actual relevant structures searched for (e.g. the lymph nodes).

6.3. Ad–Hoc Detection Model

In this section we present the ad–hoc probe model we use in fhPET imaging. First of all, our model computes the geometric attenuation using the solid angle Ω subtended by the detector on a point source. This determines the portion of the initial radiation that should in the ideal case reach the detector due to the isotropy of radiation. We use the same formula as in equation 5.10 for computing the solid angle:

$$\Omega\left(d_{ij}, r, \alpha_{ij}\right) = \frac{1}{2}\left(1 - \frac{1}{\sqrt{\frac{r^2}{(d_{ij})^2} + 1}}\right) cos\left(\alpha_{ij}\right)$$

where once more d_{ij} is the distance between the detector and the point source, r is the detector radius, and α_{ij} is the inclination angle (see figure 5.12).

In the next step, we consider the effects of the shielding around and the ab-

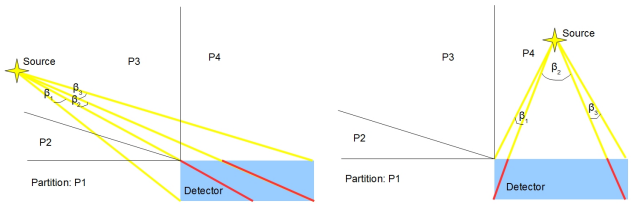

(a) The length of interaction of gamma rays within the detector.

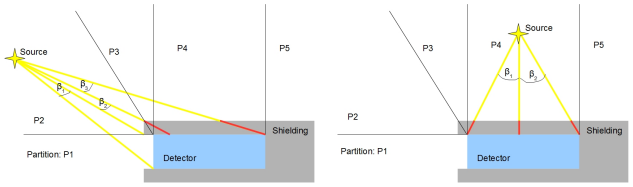

(b) The length of interaction of gamma rays within the shielding material.

Figure 6.2.: Partition–based ad–hoc model for imaging with the high–energy probe. The length that gamma rays take through the detector and shielding (red portions of the rays) is computed depending on the partition (P1, P2, ...) in which the point source lies.

sorption within the detector of the probe. We consider these two by incorporating a probability formula based on the geometric and the material properties of the probe. For this purpose the ad–hoc model computes the mean lengths that gamma rays will traverse through the shielding and the detector. These lengths are obtained by dividing the space around the probe into partitions in each of which these lengths can be computed with a unique formula. Due to the symmetry, the computations can be reduced to a profile slice through the probe. In this slice we consider the four rays that reach the four corners of the detector and for each of these rays we compute the length of interaction l that the ray traverses through the detector (see figure 6.2(a)). The probability of an interaction in the detector along this ray can be computed using the formula:

$$p = p\,(l) = 1 - e^{\mu l} \tag{6.1}$$

where μ is a material coefficient (detector: BGO, shielding: *tungsten* [Phys 10]).

Using this probability function we can now compute the mean probability p_n of an interaction between two successive rays l_n and l_{n+1} by integrating over the probability function with these two rays as boundaries and then dividing by the

difference in the length of interaction of both rays (assuming $l_{n+1} > l_n$):

$$p_n = \frac{\int_{l_n}^{l_{n+1}} \left[1 - e^{\mu l}\right] dl}{l_{n+1} - l_n} \tag{6.2}$$

$$p_n = \frac{[l_{n+1} - l_n] - \left[\frac{e^{\mu l_{n+1}} - e^{\mu l_n}}{\mu}\right]}{l_{n+1} - l_n} \tag{6.3}$$

$$p_n = 1 - \frac{e^{\mu l_{n+1}} - e^{\mu l_n}}{\mu \left[l_{n+1} - l_n\right]} \tag{6.4}$$

By weighting these probabilities with the angle β_n between these rays (see figure 6.2) and dividing by the total angle between the two outer rays we get the mean probability for an interaction of a gamma ray emitted by a point source on a specific position relative to the probe:

$$\overline{p} = \frac{\sum_n \beta_n p_n}{\sum_n \beta_n} \tag{6.5}$$

The absorption in the shielding (see figure 6.2(b)) is computed in a similar way.

The mean probability for an absorption in the shielding $\overline{p_s}$ and in the detector $\overline{p_d}$ computed thus are then used to compute the coefficients a_{ij} for use in equation 3.8:

$$a_{ij} = (1 - \overline{p_s})\ \overline{p_d}\ \Omega \tag{6.6}$$

6.4. Experimental Feasibility Study for HNSCC Surgery

In order to build a realistic phantom representative of a recurrent HNSCC, we retrospectively evaluated a collective featuring 22 patients with histologically proven HNSCC (age: 28–71 years, mean: 55.8 years, gender: 16 males, 6 females). For diagnosis, these patients had been scanned pre–operatively with PET/CT and US. In those 22 cases, the nuclear medicine physicians were able to identify a total of 45 LNs in the PET images (mean: 2.04 per patient). However the number of LNs very much varies from patient to patient. In 5 out of 22 patients, no LNs were visible at all in the PET scan. In 4 patients, 4 or more LNs were identified by the physicians.

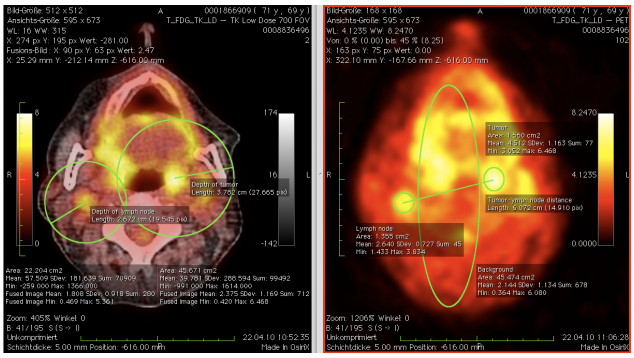

Figure 6.3.: Screenshot from one retrospectively evaluated patient data. We identified the tumor and LN locations, as well as depths, in the overlaid PET/CT images (left). We obtained the corresponding average activity values from the PET images (right). In addition, we calculated the unspecific background radiation values (in this case the large elliptic region). We obtained these values by averaging the activity values within the respective, marked region of interest.

lymph node diameter:	$1.6 \pm 1.10\ cm$
tumor depth from surface:	$5.3 \pm 1.06\ cm$
lymph node depth from surface:	$2.6 \pm 0.99\ cm$
tumor–to–background (T/BG) uptake ratio:	3.3 ± 1.17
tumor–to–lymph node (T/LN) uptake ratio:	1.5 ± 0.97
tumor uptake:	$23.8 \pm 9.41\ kBq/ml$
lymph node uptake:	$21.3 \pm 12.75\ kBq/ml$

Table 6.1.: The mean geometrical and radioactivity–related parameters obtained from patient data assessment for the experiment setup.

6.4.1. Experiment setup

For reducing the complexity, we thoroughly analyzed the PET/CT scans of only 7 patients (age: 53 years mean, gender: 6 males, 1 female) with 1 or 2 identified metastatic LNs. In total there were 10 suspicious LNs (mean: 1.4 per patient, stddev.: 0.53). See figure 6.3 for an illustration and explanation of our retrospective evaluation. Following the surgical resection, all these LNs had been histologically examined for metastases and 5 cases were positive. Using these datasets with suspicious LNs, we calculated the values seen in table 6.1.

We prepared a neck phantom using a plastic compact disc (CD) box (very close to an average human neck in terms of dimension). In order to simulate a recur-

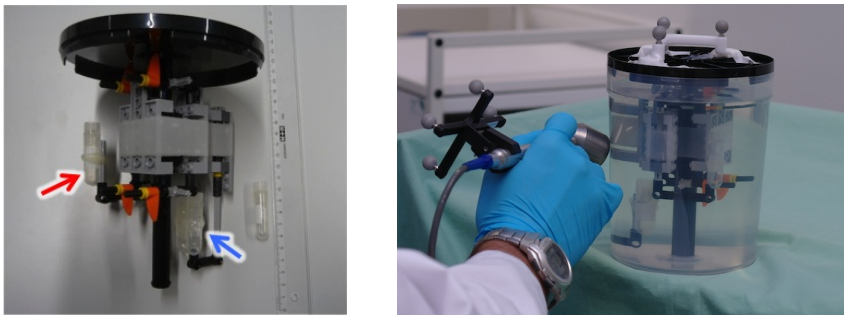

(a) Phantom construction. (b) Operator scanning the neck phantom.

Figure 6.4.: The neck phantom simulating a tumor mass (blue arrow) and an [^{18}F]FDG–PET–positive lymph node (red arrow).

rent tumor (T) mass and an [^{18}F]FDG–PET–positive LN, we glued two 2 ml lab reservoirs rigidly to each other. We used a third one for the LN. We attached these two structures rigidly and reproducibly to the CD box with a construction of Lego™ pieces. After rigidly attaching a tracking target on top of our phantom, we obtained a CT image that serves as a ground truth for the locations of the simulated recurrent T and LN. The fiducials of the tracking target provide landmarks for registering the CT image to each of the fhPET images. The simulated T and LN are apparent in the CT images. For assessing the error in the fhPET images, we manually marked the midpoint of each of these two (by purely visual assessment). This manual marking provided the basis for the ground truth locations for comparing the fhPET images against. The phantom setup can be seen in figure 6.4(a).

6.4.2. Experiment protocol

We conducted three different sets of experiments (referred to as *[^{18}F]FDG–real*, *[^{18}F]FDG–high*, and *^{99m}Tc–high* respectively) with the neck phantom in order to evaluate fhPET with respect to the localization of tumors and metastatic LNs in HNSCC. [^{18}F]FDG–real features [^{18}F]FDG injected into the structures in realistic activity concentrations. [^{18}F]FDG–high simulates homogeneous tracer uptake in the tumor and LN, but a higher dose of [^{18}F]FDG (2 orders–of–magnitude higher than the values obtained from patient data). ^{99m}Tc–high is the same as [^{18}F]FDG–high except that ^{99m}Tc is used instead of [^{18}F]FDG. For this last set of experiments, we performed the scan and reconstruction using the fhSPECT system. Our aim was to compare the images obtained with the fhSPECT system and our fhPET

system, in the light of the discussion about the additional challenges of fhPET compared to fhSPECT, outlined in section 6.2.2. We repeated the experiment sets [^{18}F]FDG–high and ^{99m}Tc–high with background (B) activity (T/B activity ratio of 20:1).

Two operators scanned each phantom configuration two or three times respectively, each time covering about $120\ ^{\circ}$ around the phantom, obtaining 3,000 measurements (see figure 6.4(b)). A total of 7 scans for [^{18}F]FDG–real, 17 scans for [^{18}F]FDG–high, and 12 scans for ^{99m}Tc–high were acquired respectively. In each case we inverted the resulting linear system by applying MLEM with 20 iterations. We smoothed the obtained reconstruction using either a $4\ mm$ or a $6\ mm$ Gaussian filter to reduce the reconstruction noise that is due to the highly under–sampled acquisition with insufficient statistics. The choice of the Gaussian filter size was determined by pure visual assessment of the image quality resulting from filtering.

6.4.3. Evaluation & results

In order to register the fhPET images on to the ground truth, i.e. CT, images of the phantom, we followed the same approach as the one outlined in section 5.6.1.3. Using the registration, we computed the distance between the centroid of the LN in the fhPET (or fhSPECT, depending on the dataset) images and the ground truth–midpoint in the CT (see figure 6.5 for a visual illustration). We repeated this for the tumor as well, for the cases where the tumor was visible in the fhPET images. We refer to these distances as the *localization error (loc. error)*.

For qualitative evaluation, we checked the visibility of the tumor and the LN in the reconstructions. Within the first set of scans ([^{18}F]FDG–real) we were able to identify the LN in 3 of the 7 datasets. However we were able to identify the tumor in none of the datasets. In the second set of scans ([^{18}F]FDG–high) we were able to identify the LN in all of the 17 datasets. Moreover, we were able to localize the tumor in 6 (3 of those with background activity) reconstructions (see figure 6.5). In one of these we could even distinguish the two reservoirs next to each other, simulating the tumor. This reconstruction with a zoom on the two reservoirs is shown in figure 6.6(a). All numerical results are listed in table 6.2.

One thing worth noting is that the datasets from phantom configurations with [^{18}F]FDG lead to reconstructions with a lot of artifacts. We were able to identify the tumor only vaguely in those 6 reconstructions mentioned above due to the ar-

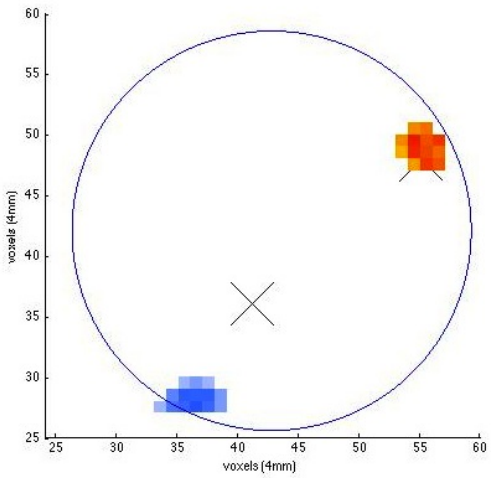

Figure 6.5.: A transverse view from one fhPET reconstruction, illustrating the localization errors visually. **Blue blob:** reconstructed tumor (the cross nearby showing the tumor location in the ground truth). **Red blob:** reconstructed LN (the cross within showing the LN location in the ground truth). **Circle:** an outline of the phantom.

Experiment setup	B:T:LN	LN visible?	T visible?	LN loc. error (mm)	T loc. error (mm)
[^{18}F]FDG–real	0:17:10	3/7	0/7	12.67 ± 2.48	NA
[^{18}F]FDG–high	0:20:20	9/9	3/9	13.57 ± 4.22	34.79 ± 6.20
	1:20:20	8/8	3/8	14.41 ± 5.75	47.39 ± 22.28
^{99m}Tc–high	0:20:20	6/6	5/6	11.35 ± 4.26	39.39 ± 10.60
	1:20:20	6/6	3/6	10.85 ± 4.07	20.42 ± 2.55

Table 6.2.: Numerical results of the HNSCC–phantom study. **B:** background activity, **T:** tumor activity, **LN:** lymph node activity (all relative to each other).

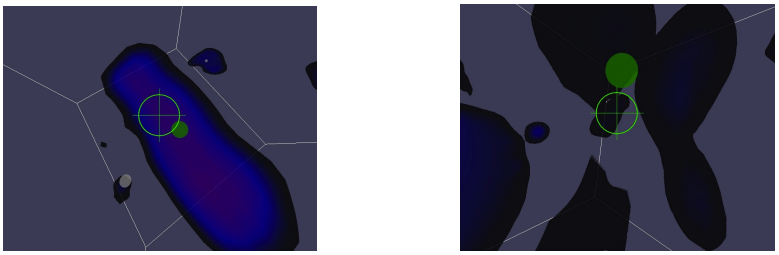

(a) Lymph node. (b) Tumor mass.

Figure 6.6.: Reconstructions of the simulated lymph node and residual tumor mass.

tifacts. In addition, the size and shape of the tumor in the reconstructions varies substantially. On the other hand the datasets from phantom configurations with ^{99m}Tc produced much less artifacts. In addition, the tumor localization error for the [^{18}F]FDG configurations with background activity was more than twice the localization error for the ^{99m}Tc configurations. Curiously, for the configurations without background activity, the [^{18}F]FDG datasets yielded lower tumor localization error compared to the ^{99m}Tc datasets (see table 6.2). However, as a matter of fact the tumor was visible in 8 of 12 ^{99m}Tc datasets, while it was vaguely visible only in 6 of 17 [^{18}F]FDG datasets. Moreover the LN localization error is clearly lower in the ^{99m}Tc datasets than in the [^{18}F]FDG datasets. Last, but not least, the more experienced of the two operators who performed the scans was able to produce scans that identified the two structures of interest within the phantom for both [^{18}F]FDG as well as ^{99m}Tc datasets.

6.5. First Experience in OR

In December 2012 we were able to obtain the first intra–operative datasets of a patient, a 77–year–old male diagnosed with thyroid carcinoma. The [^{18}F]FDG–PET/CT scans of the patient revealed six LNs suspected for metastases. Interesting for us were four out of these six LNs, targeted for surgical resection. These four LNs were located in two sets of two LNs, with each pair of LNs almost joint with each other. The corresponding [^{18}F]FDG–PET/CT slices can be seen in figure 6.7(a) and figure 6.7(b).

On the day of the surgery, the patient was injected $50\ MBq$ [^{18}F]FDG and anesthetized approximately two hours post–injection. However due to *intubation*[1] complications, the patient had to be *reanimated*, i.e. awakened from anesthesia. This introduced a delay of approximately five hours with respect to the originally scheduled time of the surgery. In other words, two and a half additional half–lives of ^{18}F had passed in between.

We scanned the patient with fhPET twice after the initial incision was made; prior to the resection of the first LN pair, and prior to the resection of the second LN pair (each time covering the region where the respective LN pair was located). Screenshots showing the intra–operative fhPET reconstructions obtained after both scans can be seen in figure 6.8(a) and figure 6.8(b) respectively.

[1] *Intubation* refers to the placement of a special tube through the mouth and into the airways of an anesthetized patient, in order to facilitate the breathing during surgery.

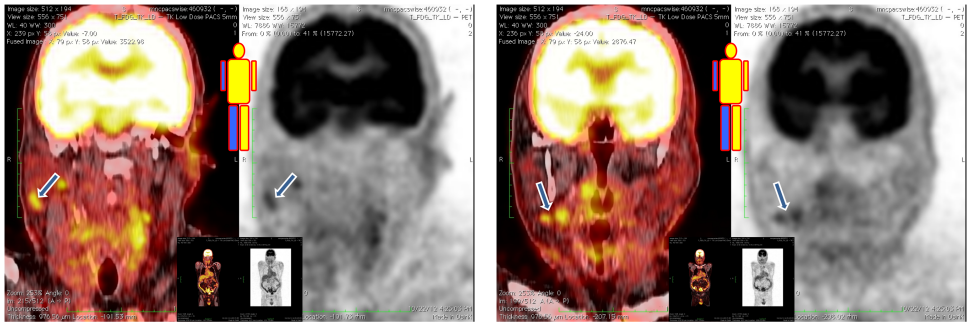

(a) LN # 1 and # 2. (b) LN # 3 and # 4

Figure 6.7.: PET/CT image of the patient: [^{18}F]FDG–PET–positive LNs indicated with a blue arrow. The small centered image at the bottom shows the whole–body PET/CT and PET slice from which the zoomed–in coronal slice was taken. The centered figure in the upper part is a legend for orientation (blue body parts showing the right side).

Unfortunately we have no ground truth data to compare our results against, since the pre–operative scans of the patient can unfortunately not be registered to the intra–operative reconstructions due to the fact that the pre–operative PET/CT images were not obtained with a tracking target attached to the patient for use as a landmark. Therefore we did not conduct any numerical analysis of these data. However we only report here that the chief surgeon who operated the patient was very positive of the results we obtained by his purely visual intra–operative assessment. In figure 6.8(a), the HE probe can be seen pointing to the LN with the distance between the probe tip and the LN displayed in the upper right corner of the screenshot. During the surgery, the chief surgeon was quite confirmative even about these navigation values, pinpointing the LNs. In our retrospective evaluation, we saw however that the LNs were reconstructed much closer to the surface (i.e. to the skin of the patient) than they really were. We believe this is due to the extremely limited–angle of the scans, because of the locations of both LN pairs and the somehow thick neck of the patient.

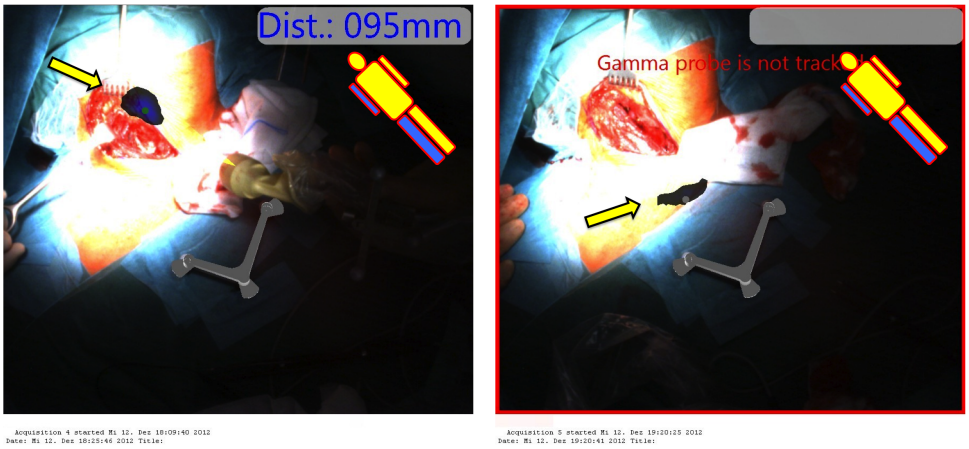

(a) (b)

Figure 6.8.: fhPET image of the LNs **6.8(a)** in figure 6.7(a) and **6.8(b)** in figure 6.7(b) (seen as a dark blue blob indicated by the arrow in each image). The legend for orientation is the same as in the corresponding pre–operative image. Note that due to the small distance between the two LNs, the fhPET image could not resolve these separately.

6.6. Discussion

SIMILAR to the case of epiphanography, our approach to fhPET can be categorized somewhere between using high–energy probes standalone and the dedicated intra–operative PET systems presented in section 4.2.2.

We have made an attempt to put fhPET into the medical context of the surgical management of (especially recurrent) HNSCC, by constructing the presented neck phantom. This phantom has high geometrical customizability and reproducibility. Our results show that we are able to reconstruct the mock LN in all cases, albeit with a high localization error between $12.7\ mm$ and $14.4\ mm$. The main drawback is that the system falls short of reconstructing structures of interest that lie a little deeper (as in the case of the mock tumor within the study), especially at realistic activity concentrations. At higher activity concentrations this mock tumor was visible, but with unacceptably high errors (see table 6.2).

The high energies of annihilation gammas detected by a high–energy probe combined with a sub–optimal collimation contribute to a decrease in accuracy. Coincidence detection is a remedy to this issue. Therefore a dedicated PET sys-

tem like the hand–held imagers of Stolin *et al.* outlined in section 4.2.2 could be a more suitable approach. On the other hand the major advantage of our system over dedicated intra–operative PET systems based on coincidence detection is the absence of a second detector block to be placed e.g. underneath the patient. Hence it avoids a potentially bulky setup [Shak 12b].

The first fhPET images we obtained during our first experience in the OR looked very good. However it was disappointing to find out later that the reconstructed lymph nodes were too far away in term of depth from the actual locations. Yet the viewing angle of the stereo–cameras during the surgery had made them appear to be just on the right spot. This could have been due to the small angular coverage of the region of interest with the probe during the surgery. Especially the fact that within the phantom study the structures of interest could be reconstructed in those scans where the more experienced operator achieved firstly; a better angular coverage, and secondly; a better *exclusion* of the cold regions makes us draw this conclusion.

Part III.

Conclusions & Back Matter

CHAPTER 7

Conclusions

IN this final chapter of this PhD thesis, we outline the conclusions from this research work and provide a guideline in terms of the future work for resuming the research and development of the two novel imaging modalities we have introduced.

7.1. Intra–operative Epiphanography

THIS work has laid down the technical foundations for intra–operative imaging with beta probes and shows the first positive results in general. In particular, we have attempted to put this novel imaging modality into the context of the neurosurgical management of LGGs.

The long–term vision is to conduct studies with patients before fully integrating this novel imaging modality into the surgical workflow. The path that leads to this vision passes through the proof–of–concept on realistic phantoms first. Our phantoms have evolved along this line. Nonetheless, we are not yet at the point of a fully realistic LGG–neurosurgery–mimicking phantom, mainly due to the positron challenge. Therefore the most important part of future work remains in designing more realistic phantoms and conducting a study with surgeons on how to integrate epiphanography into the workflow. Major issues that could arise should be discussed as well. However we think that most of the problems associated with using pre–operative images intra–operatively, such as brain shift and

deformation would play only a minor role, due to the fact that epiphanography is real–time. Alongside these, it is important to assess the minimal dose of the radiotracer to be delivered to the patient, obviously for radiation protection purposes. This could be done by e.g. varying the amount of radioactivity in the phantom by evaluating real patient data in correlation to the injected dose. Once this proof–of–concept on phantoms is firmly accomplished, epiphanography could be studied in an intra–operative scenario featuring HGG patients, before moving on to LGG patients. The reason is that HGG is an easier case where the imaging modality could be more easily validated, while yet providing useful intra–operative information.

The more short–term vision pertains to the technicalities of the system. First of all, our approach to generating surface models from scattered point clouds and the implementation thereof in our software framework should be further developed towards robustifying it such that it will function under a wide range of different inputs. One other task could be to assess the error in the generated geometric surface model with respect to the *real* surface. If and once sub–millimeter accuracy can be ensured, the ad–hoc models could be enhanced such that they take into account the depth information, i.e. some kind of *positron attenuation*. This information might improve the image quality. Secondly, more precise and reproducible phantoms for quantifying the resolution limitations of the system are to be developed. In addition, the effect of sterile sheathing is to be assessed in terms of attenuating positrons, i.e. decreasing the signal quality of the probe, before moving on to studies with patients. Thirdly, several software issues have to be addressed. First, the source of the bug leading to the synchronization issue elaborated in section 5.6.2.3 is to be found and corrected. Second, our software framework in its current status lacks a good visualization and navigation interface. Only after all these short–term issues have been addressed should the new team focus on the long–term vision of workflow integration.

7.2. Intra–operative PET

THE most important finding we made during our neck phantom study is that the scan protocol makes a big difference in terms of the fhPET image quality. Therefore in the short–term it would be wise to perform a study with the phantom in order to develop and test possible strategies for acquiring data in an intelligent way, such that structures of interest can be *included* and irrelevant regions

with low activity can be *excluded*. Although these two are the implicit purpose of image reconstruction, we emphasize them explicitly here, because they become more important in the challenging scenario of radio–guidance in HNSCC with fh-PET, especially considering the high unspecific uptake associated with [^{18}F]FDG. One other major issue is related to the sub–optimal collimation of the high–energy probe. This must be studied in detail and if necessary, the ad–hoc detection model has to be modified appropriately.

Due to the high unspecific uptake of [^{18}F]FDG (which is to be used in our clinical scenario), it is virtually mandatory to introduce some kind of prior information into the procedure. In that sense, registering pre–operative [^{18}F]FDG–PET/CT images on to the intra–operative scene could be considered as an intuitive option. For this task of registration, intra–operative ultrasound could be used as a common frame. In addition, the capabilities and limitations of the system in the context of feasibility with realistic activities must be studied further. The natural first approach to this task is to follow on our footsteps and get the quantitative numbers pertaining to radioactivity from patient data. Once the feasibility of fhPET in realistic uptake situations based on pre–operative [^{18}F]FDG–PET/CT images has been proven, finding out the minimal activity to inject could be considered as the next step. One other advantage of registering pre–operative [^{18}F]FDG–PET/CT is that it would allow for performing *attenuation correction (AC)* for fhPET, thereby potentially improving the image quality. Last but not least, the AC atlas inferred from the CT data could also serve for constraining the volume of interest in reconstruction. This would then implicitly eliminate a big portion of the artifacts the fhPET images of our neck phantom unfortunately suffer from.

Appendices

A. Spatial Resolution Phantom Images

Abbreviations used are **GT** for *ground truth*, **R** for *reconstruction*.

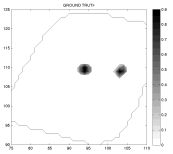

Figure 1.: 4 mm: **GT** (left), **R** (right).

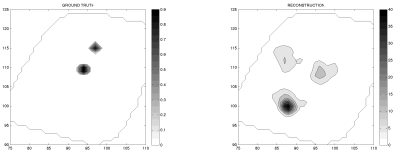

Figure 2.: 5 mm: **GT** (left), **R** (right).

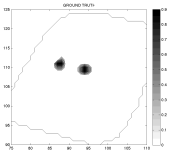

Figure 3.: 6 mm: **GT** (left), **R** (right).

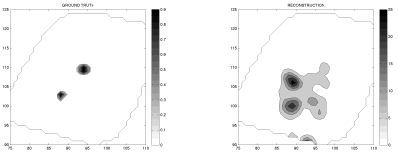

Figure 4.: 7 mm: **GT** (left), **R** (right).

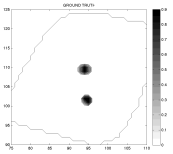

Figure 5.: 8 mm: **GT** (left), **R** (right).

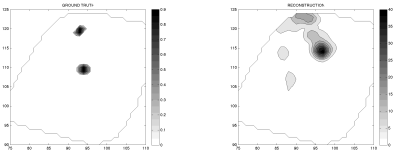

Figure 6.: 9 mm: **GT** (left), **R** (right).

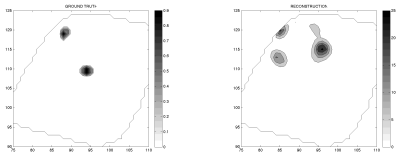

Figure 7.: 10 mm: **GT** (left), **R** (right).

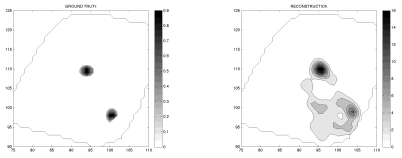

Figure 8.: 11 mm: **GT** (left), **R** (right).

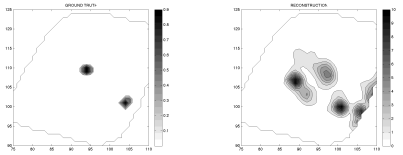

Figure 9.: 12 mm: **GT** (left), **R** (right).

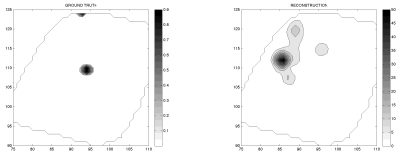

Figure 10.: 13 mm: **GT** (left), **R** (right).

B. Neurosurgery Phantom II Images

Abbreviations used are **GT** for *ground truth*, **DS** for *dataset*, **DBG** for *deep background activity*, **HS** for *hot–spot(s)*.

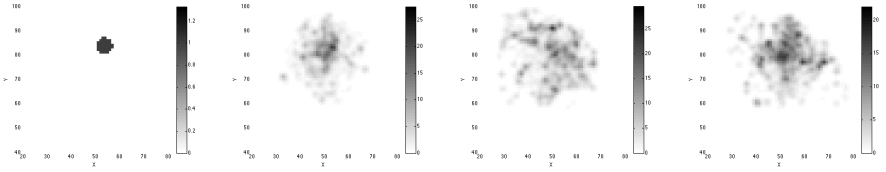

Figure 11.: 1 HS. **GT, DS #1, #2, #3** (left–to–right).

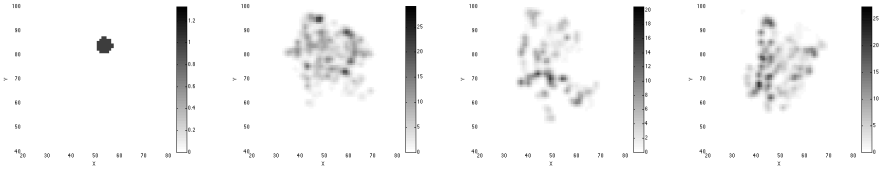

Figure 12.: 1 HS, with DBG. **GT, DS #1, #2, #3** (left–to–right).

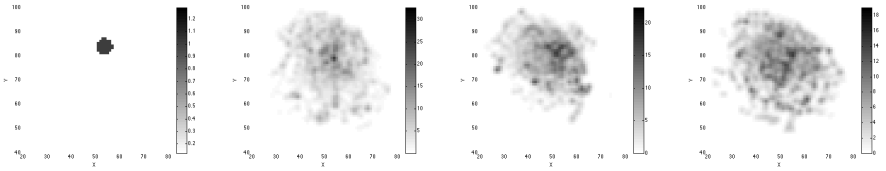

Figure 13.: 1 HS, 8:1 T/B. **GT, DS #1, #2, #3** (left–to–right).

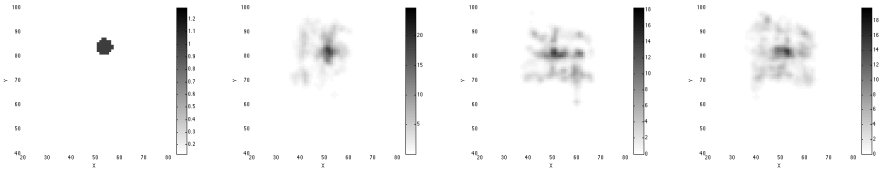

Figure 14.: 1 HS, with DBG, 8:1 T/B. **GT, DS #1, #2, #3** (left–to–right).

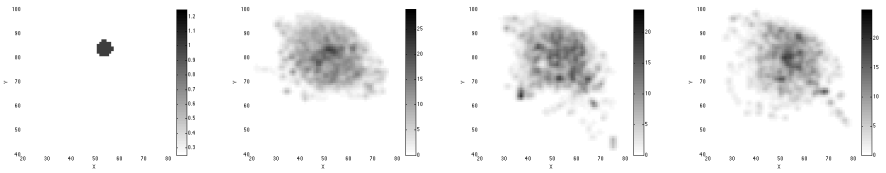

Figure 15.: 1 HS, 4:1 T/B. **GT, DS #1, #2, #3** (left–to–right).

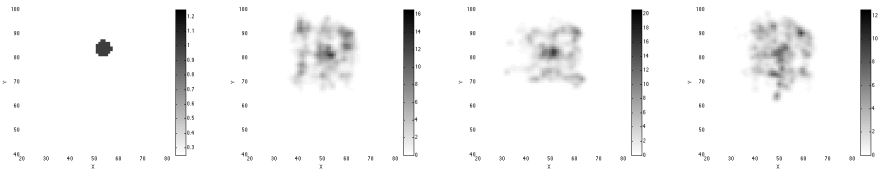

Figure 16.: 1 HS, with DBG, 4:1 T/B. **GT, DS #1, #2, #3** (left–to–right).

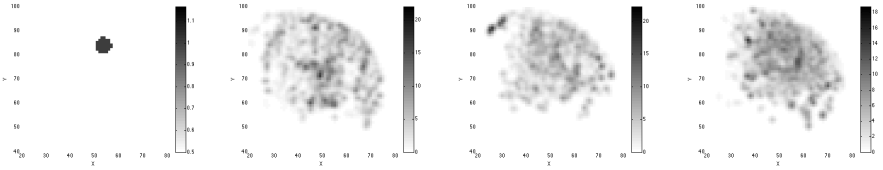

Figure 17.: 1 HS, 2:1 T/B. **GT, DS #1, #2, #3** (left–to–right).

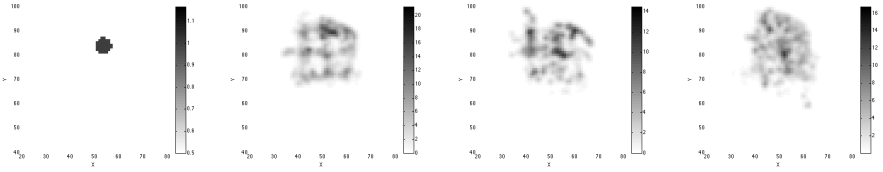

Figure 18.: 1 HS, with DBG, 2:1 T/B. **GT, DS #1, #2, #3** (left–to–right).

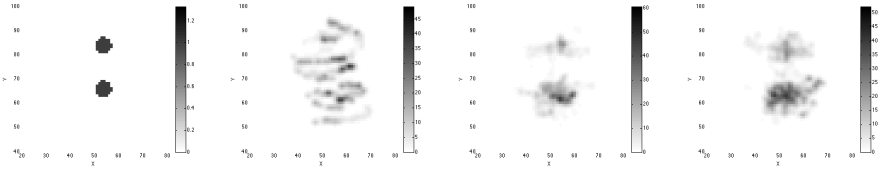

Figure 19.: 2 HSs. **GT, DS #1, #2, #3** (left–to–right).

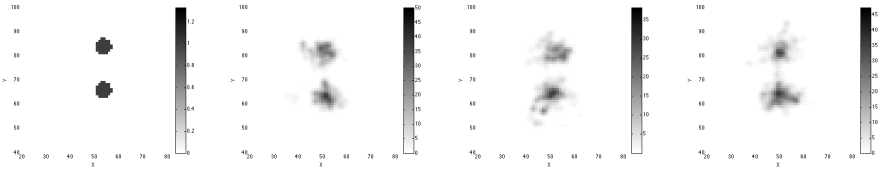

Figure 20.: 2 HSs, with DBG. **GT, DS #1, #2, #3** (left–to–right).

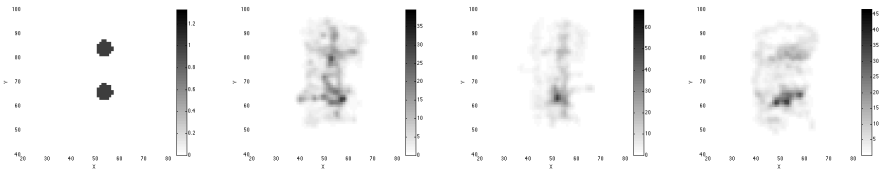

Figure 21.: 2 HSs, 8:1 T/B. **GT, DS #1, #2, #3** (left–to–right).

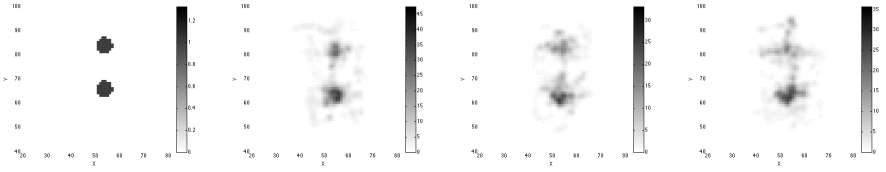

Figure 22.: 2 HSs, with DBG, 8:1 T/B. **GT, DS #1, #2, #3** (left–to–right).

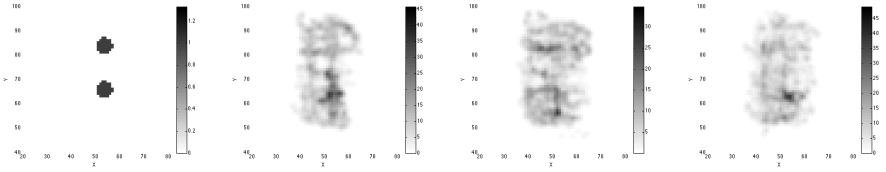

Figure 23.: 2 HSs, 4:1 T/B. **GT, DS #1, #2, #3** (left–to–right).

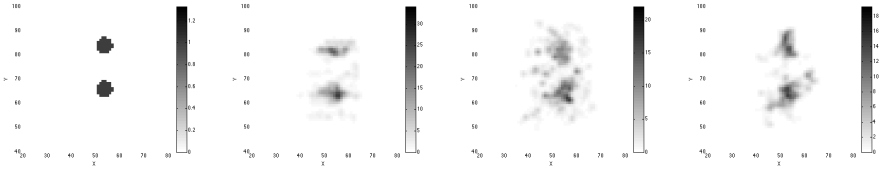

Figure 24.: 2 HSs, with DBG, 4:1 T/B. **GT, DS #1, #2, #3** (left–to–right).

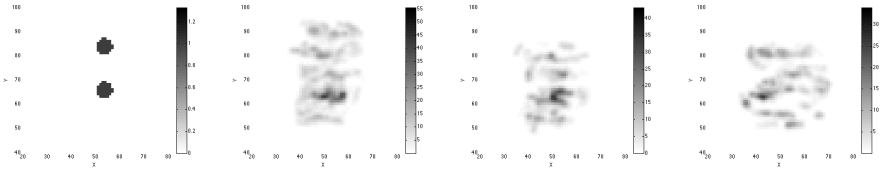

Figure 25.: 2 HSs, 2:1 T/B. **GT, DS #1, #2, #3** (left–to–right).

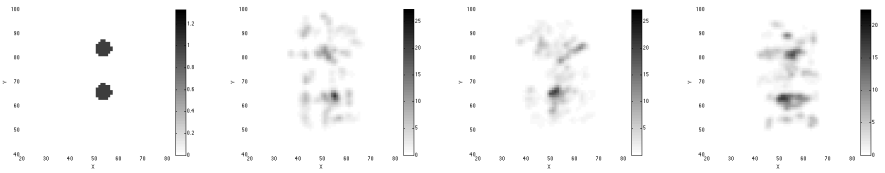

Figure 26.: 2 HSs, with DBG, 2:1 T/B. **GT, DS #1, #2, #3** (left–to–right).

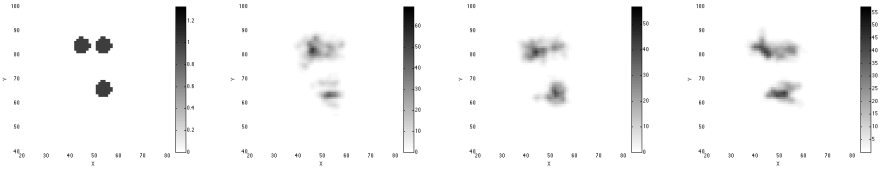

Figure 27.: 3 HSs. **GT, DS #1, #2, #3** (left–to–right).

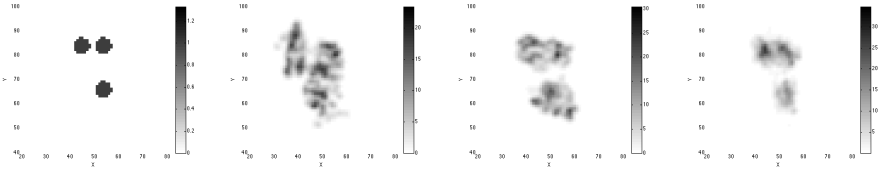

Figure 28.: 3 HSs, with DBG. **GT, DS #1, #2, #3** (left–to–right).

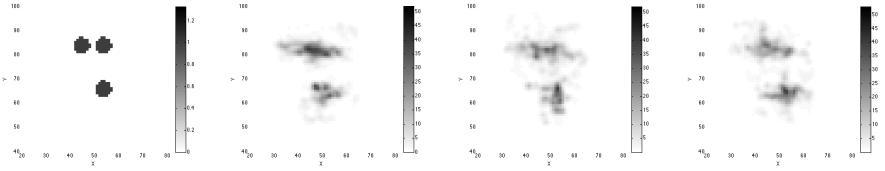

Figure 29.: 3 HSs, 8:1 T/B. **GT, DS #1, #2, #3** (left–to–right).

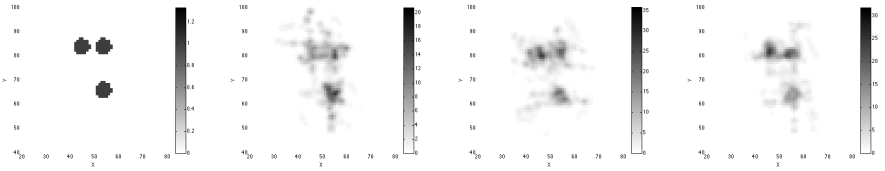

Figure 30.: 3 HSs, with DBG, 8:1 T/B. **GT, DS #1, #2, #3** (left–to–right).

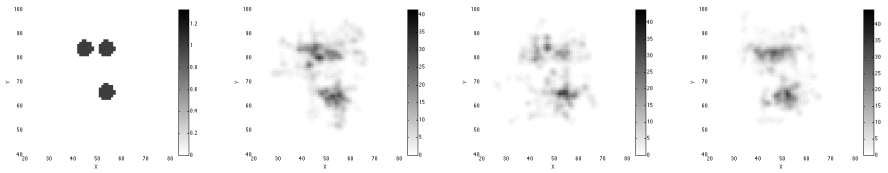

Figure 31.: 3 HSs, 4:1 T/B. **GT, DS #1, #2, #3** (left–to–right).

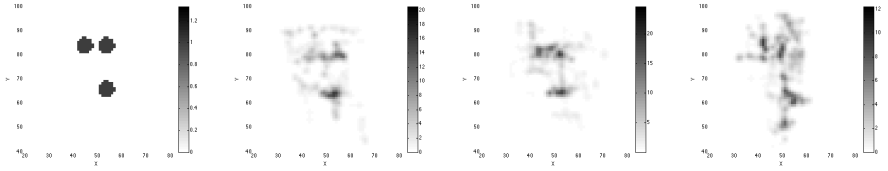

Figure 32.: 3 HSs, with DBG, 4:1 T/B. **GT, DS #1, #2, #3** (left–to–right).

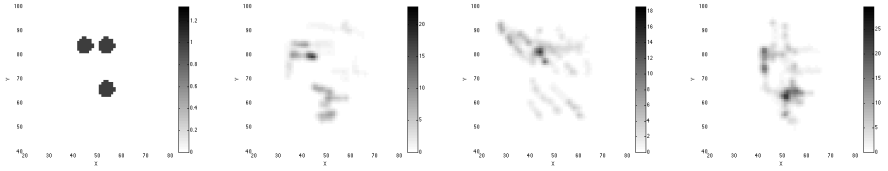

Figure 33.: 3 HSs, 2:1 T/B. **GT, DS #1, #2, #3** (left–to–right).

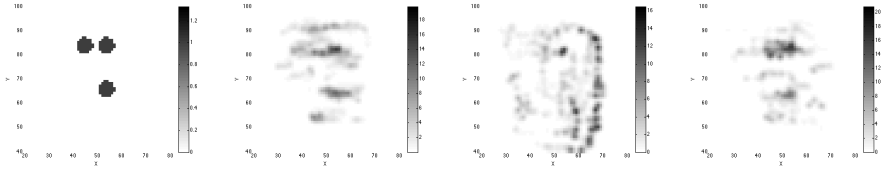

Figure 34.: 3 HSs, with DBG, 2:1 T/B. **GT, DS #1, #2, #3** (left–to–right).

C. Nuclear Intra–operative Navigation (NuIoNa) Software Framework

THIS section briefly introduces the ***Nu**clear **I**ntra–**o**perative **Na**vigation (**NuIoNa**)* software framework we have designed and developed in the course of our PhD project. First we give an overview of **NuIoNa**. Then we present a short guideline with screenshots about how the graphical user interface (GUI) of **NuIoNa** works. Finally we elaborate on the software design for those who would like to use **NuIoNa** for imaging or for further development. This section is meant as a very brief and concise guideline, rather than a detailed overview, since the latter would make this section much too long for the scope of this thesis.

C.1. Overview

Everything pertaining to **NuIoNa** can be found on the SVN server of the Chair for Computer Aided Medical Procedures (`https://camplinux.in.tum.de/svn/`) under the directory `campintern/trunk/src/NuIoNa_v2/`. This directory has the following tree structure:

- `apps/` contains the two applications available to **NuIoNa** users.
- `libs/` contains the libraries (modules).
- `ext/` contains external libraries (modules).
- `cmake/` contains various `CMake` [CMak 13] scripts for configuration.
- `tests/` contains unit tests written for different modules.

For the inter–dependence of the various components of the **NuIoNa** framework, a `Dia` [Apps] graphics file is provided (`Structure.dia`), under the main directory on the SVN server.

C.2. Guideline

In the current version of **NuIoNa**, there are two main applications. The first one features a graphical user interface (GUI) for data acquisition with a probe and a tracking system. The data can be saved for offline use. The second one is a command line–based application for offline reconstruction. We would like to give

a very brief overview of these two applications, with little text and more graphical content.

C.2.1. GUI overview

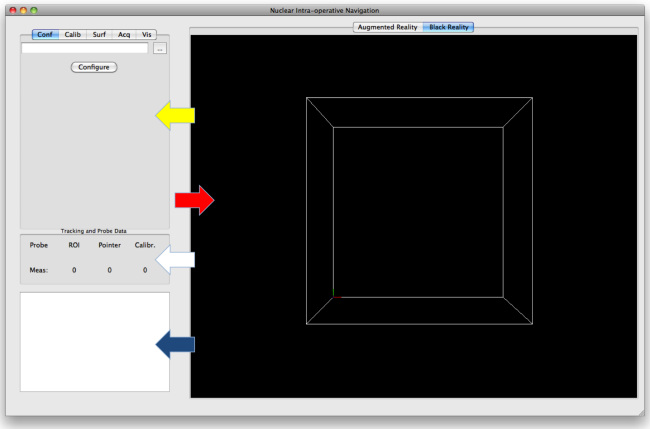

Figure 35.: **NuIoNa** GUI overview. **Yellow arrow:** configuration and control panel. **White arrow:** data panel. **Blue arrow:** message panel. **Red arrow:** visualization panel.

The GUI has four panels, as seen in figure 35. The configuration and control panel features various tabs for steering the application (for details, see section C.2.2). The data panel helps in tracking the status of the data coming from the devices, as well as the measurement values. The message panel is for issuing warnings, errors, or simply feedback messages. The visualization panel features for the time being only a simple rendering window for simple visualization. This panel has another tab that is reserved for augmented reality visualization e.g. with a camera image.

C.2.2. Steps to data acquisition

This section presents the steps to acquiring data with **NuIoNa**, through screenshots and detailed captions. The order of the screenshots follows the order of the steps to data acquisition. Elements on the GUI (e.g. labels, buttons) are highlighted in `blue color`.

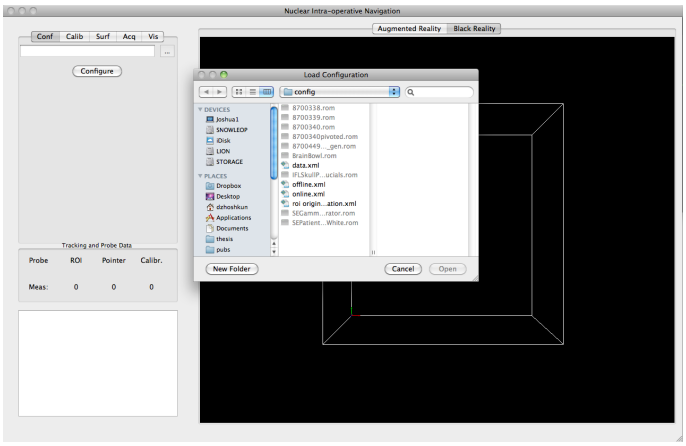

Figure 36.: **NuIoNa** XML file selection. On clicking the `...` button, a pop–up window opens, which allows for selecting the XML configuration file (for exemplary XML configuration files, see the `apps/intraopgui/config/` directory). After the selection, the `Configure` button must be clicked in order to configure **NuIoNa** with the given XML file.

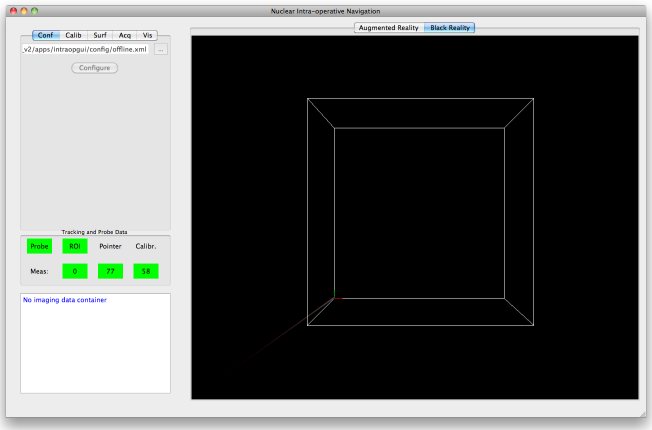

Figure 37.: **NuIoNa** data status and values: normal. Upon clicking the `Configure` button, the XML file is loaded and the application is configured. The green color indicates that data is being received normally.

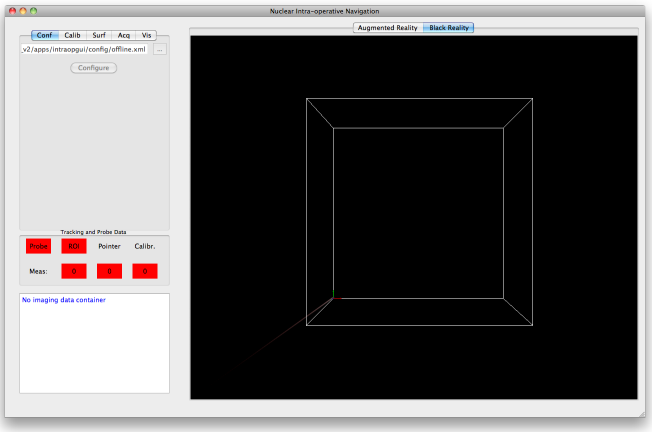

Figure 38.: **NuIoNa** data status and values: problematic. The red color indicates that data is not being received or that data is faulty (e.g. tracking precision lower than required).

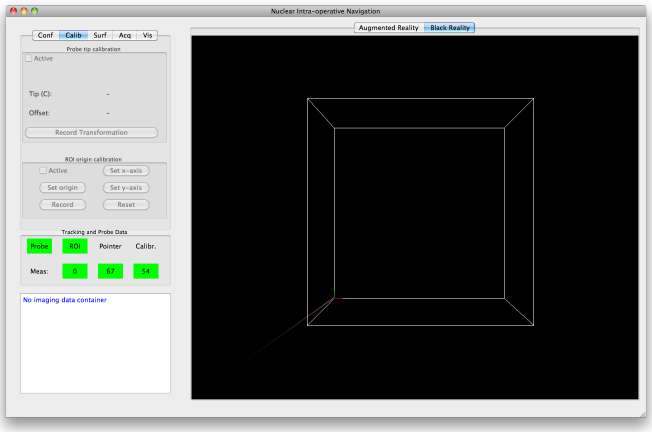

Figure 39.: **NuIoNa** calibrations. There are two types of geometric calibrations in **NuIoNa**. If configured in the XML configuration file, either one or both will be activated in the calibration tab of the control panel. To perform the `Probe tip calibration`: 1. toggle the `Activate` check box, 2. hold the probe and the probe calibrator, with the probe firmly within the corresponding socket of the calibrator, in the tracking field–of–view (FOV), 3. click the `Record Transformation` button, while active (inactive means that tracking data is missing/faulty for either of the instruments), 4. toggle the `Activate` check box. To perform the `ROI origin calibration`: 1. toggle the `Activate` check box, (while both the scan object and the pointer are within the tracking FOV, do:) 2. hold the pointer on the to–be–origin point and click `Set origin` button (success will deactivate the button in this and the subsequent two steps), 3. hold the pointer on the to–be–on–the–x–axis point and click the `Set x-axis` button, 4. hold the pointer on the to–be–on–the–y-axis point and click the `Set y-axis` button, 5. click the `Record` button, 6. toggle the `Activate` check box. Clicking `Reset` will re–start the procedure. In both types of calibration, the transformation is saved in an XML file.

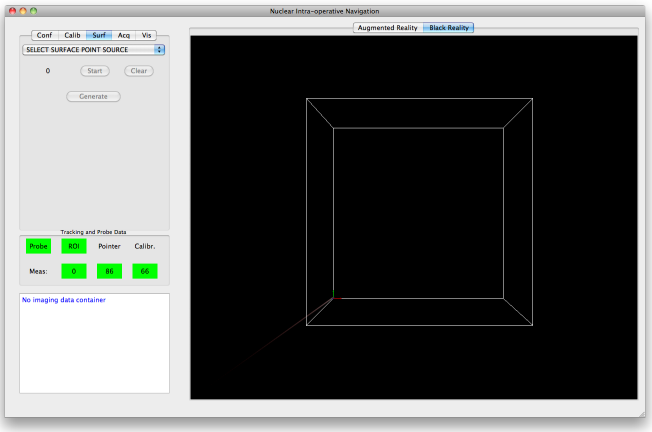

Figure 40.: **NuIoNa** surface point source selection. This tab allows the user to select from three different sources for collecting the surface points with: 1. `Probe tip`, 2. `Pointer`, 3. `Laser`. In case `Pointer` is selected, the `Start` button is activated, allowing for collecting points by scanning the surface with the pointer. To do this, simply 1. click the `Start` button (it becomes `Stop` on successful start), 2. collect points, 3. click the `Stop` button, 4. click the `Generate` button to generate the surface model. The `Clear` button clears all the points so that the collecting can be re–started. The `Laser` option is not implemented yet.

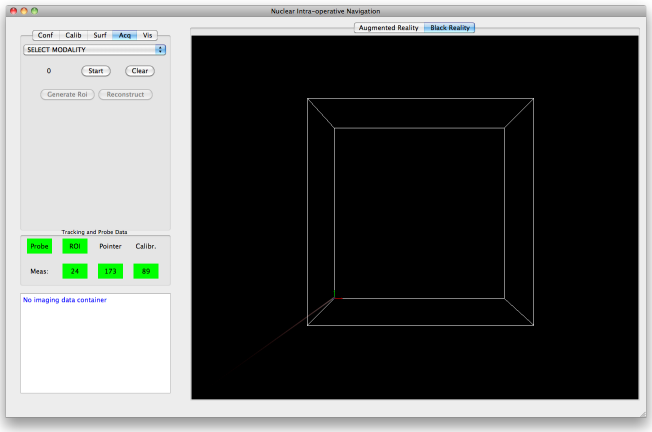

Figure 41.: **NuIoNa** modality selection. This tab allows for selecting the modality and then performing data acquisition. After selecting either of `Epiphanography` or `Freehand PET`, click `Start` to start the data acquisition (it becomes `Stop` on successful start).

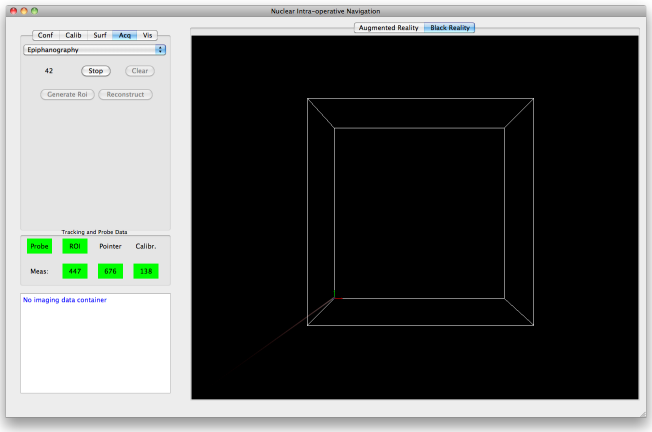

Figure 42.: **NuIoNa** data acquisition. Data is collected while it is being received and is not faulty (i.e. all indicators green). To stop the acquisition click `Stop`. Each time this button is clicked, i.e. the acquisition is stopped, the data collected up to then are saved in XML files. No data is ever overwritten, since a counter is kept that is appended to the corresponding data filenames.

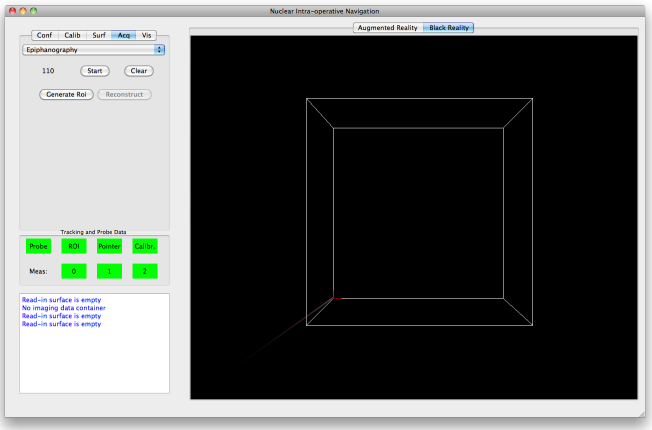

Figure 43.: **NuIoNa** data acquisition done. Clicking `Clear` clears all the collected data. In case `Probe tip` was selected as the surface point source (see figure 40), the `Reconstruction` button is inactive, waiting for the region–of–interest (ROI) model to be generated. This can be done by clicking the `Generate Roi` button. In case ROI is already generated/loaded, the `Reconstruction` button is active.

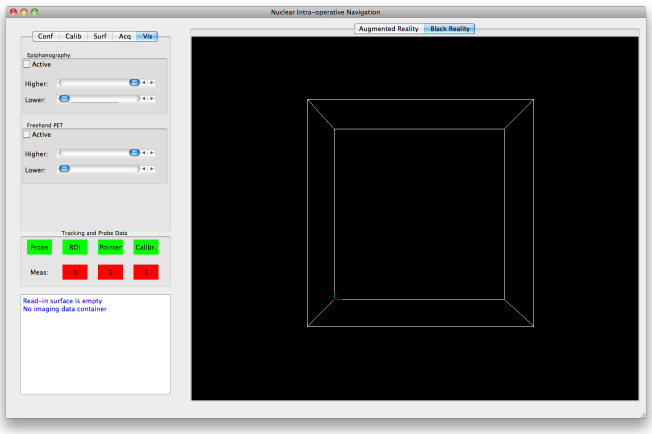

Figure 44.: **NuIoNa** visualization controls. Reconstructions from both `Epiphanography` and `Freehand PET` can be visualized on the visualization panel. This tab controls the visualization, i.e. toggling it on/off, selecting higher and lower thresholds for increasing/decreasing contrast. Currently visualization is turned off, as the application is used merely for data acquisition. To see how visualization works, see section C.2.4.

C.2.3. Steps to (offline) reconstruction

NuIoNa can be configured such that it saves the data collected during the acquisition. For an exemplary XML file that configures **NuIoNa** with this feature, see `apps/intraopgui/config/data.xml`. Each time **NuIoNa** is launched with such a configuration, the application will create a uniquely timestamped folder for saving the data into. Data saved in this manner can be used for performing offline reconstructions. The console application located under `apps/offrecon` serves this purpose. In addition, the saved data can be *replayed* with **NuIoNa**, by configuring the application with a suitable XML file. Such an XML file can be seen under `apps/intraopgui/config/offline.xml`.

C.2.4. Further development

Figure 45 shows an exemplary acquisition guidance for **NuIoNa**. The implementation of this visualization is an extension of Dr. Tobias Lasser's renderer for his `NanuLib`, which already includes the arrows for acquisition guidance. We have

added to the renderer the surface of interest (SOI) visualization seen as a white unstructured grid in this image. Hot–spots can be visualized by e.g. coloring the corresponding vertices of the unstructured grid in red, instead of white. Varying the intensity of the color can be coupled to the controls shown in figure 44.

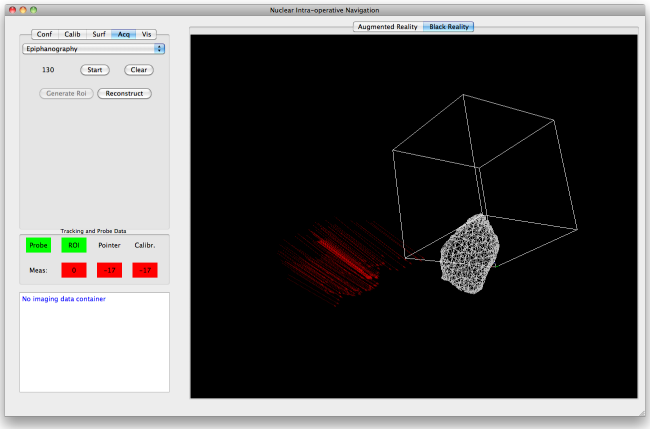

Figure 45.: **NuIoNa** acquisition guidance with arrows showing probe positions and orientations for each measurement, as well as the surface of interest (SOI) visualization (the white unstructured grid).

As the current version of **NuIoNa** is split into an *online data acquisition* and an *offline reconstruction* component, the visualization shown in figure 45 is not active. It can however be turned on with a few lines of code, as the functionality is already implemented in the `Visu` library outlined in section C.3.3.

In general, the online data acquisition application frequently crashes on run–time. Therefore it is still quite sub–optimal in terms of user satisfaction, although all the functionality related to data acquisition is implemented and brought together in it. The crashes are mostly due to multi–threading issues. We would therefore recommend the new developer to compose from scratch an application according to his/her needs, along the line of this current application. This will probably be the best practice to come up with an application featuring a GUI, that is robust and functions smoothly. Once the code of the current application highlighted in section C.3.2 is thoroughly analyzed, composing a new version is only a matter of few weeks of coding.

C.3. Software design

We have made effort to design our framework as modular as possible, with each module having a clear interface for executing a specific functionality. The following subsections give brief information about the organization of the various components of the **NuIoNa** software framework.

C.3.1. Configuration

The main directory contains a file named `EnvironmentSetup.xlsx`. This file lists the different packages and libraries to be installed in order to be able to compile and run the **NuIoNa** applications and libraries. Note that this file must be strictly followed *in the same order* to make **NuIoNa** work under Mac OS X 10.6 (Snow Leopard). For later versions of Mac OS X, the configuration should be more flexible. We have not yet tested this on later Mac OS X versions, on Windows, nor on Linux, though. Two internal libraries not mentioned in this file, but that nonetheless must be available for **NuIoNa** to work are `NanuLib` and `Eos`, developed by Dr. Tobias Lasser and Alexandru Duliu respectively. For the former, a version compatible with **NuIoNa** is located under `ext/NanuLib_v2/`. The latter however, is located on the SVN server under `campintern/trunk/src/Eos/`.

The main directory of **NuIoNa**, as well as all the relevant sub–directories contain `CMake` configuration files (`CMakeLists.txt`). These configuration files have a pretty self–explanatory structure. In addition, the `cmake/` folder contains `CMake` scripts for locating and configuring important components that **NuIoNa** needs.

C.3.2. Applications

Currently only the above mentioned two applications for online data acquisition and offline reconstruction are available under `apps/intraopgui/` and `apps/offrecon/` respectively.

C.3.3. Libraries

The following libraries are the basic working modules of the **NuIoNa** software framework.

`Core` is located under `libs/core/`. This library hosts the basic definitions and datatypes needed in **NuIoNa**.

IO is located under `libs/io/`. This library provides functionality for reading from/writing to files.

MultiTask is located under `libs/multitask/`. This library contains classes crucial in running parallel tasks. Currently it is not in active use, however the development should continue in this direction in the future.

NanuWrap is located under `libs/nanuwrap/`. This library provides a thin wrapper around the functionality and datatypes of the `NanuLib` library.

Probe is located under `libs/probe/`. This library contains all the classes and implementation relevant to communication with the different probes, as well as the class for making use of saved probe data in offline mode.

Roigen is located under `libs/roigen/`. This module provides the functionality for generating geometric surface models from scattered point clouds. It currently hosts only a `PCL` implementation [Rusu 11]. In the future other implementations, e.g. `CGAL` [CGAL 13], could also be integrated.

TrackingX is located under `libs/trackingx/`. This is a very simple extension of the `Tracking` library of `Eos`, which is used for communicating with the tracking system.

Utils is located under `libs/utils/`. As the name implies this is a utility library. It provides classes for collecting and storing data, as well as a `Utilities` class for handling datatypes and values.

Visu is located under `libs/visu/`. This library hosts the functionality pertaining to the visualization of data. The rendering window on the visualization panel of figure 35 is an instance of the `BlackRealityRenderer` class of this library, which also contains the implementation of the visualizations highlighted in figure 45.

NanuLib provides among others the implementations of various reconstruction algorithms. This library is the backbone of our imaging modalities.

`Eos` provides the functionality for XML configuration and also for tracking.

C.3.4. Tests

This portion of the **NuIoNa** framework is meant to host the unit tests written for the various components. Currently it has only an implementation of a simple `Boost` unit test for the `Roigen` library.

Nomenclature

min	Minute(s)
OR	Operating room
Bq	Becquerel – the SI unit of activity, equivalent to an inverse second (s^{-1}) [Vale 07]. $1\ Bq$ can be thought of as "one nucleus decayed per second" [Delo 98]
MBq	Megabecquerel
equivalent dose	The radiation dose in a specific organ or tissue [Vale 07]
effective dose	The tissue-weighted sum of the equivalent doses in all specified tissues and organs of the body [Vale 07]
Sv	Sievert – the SI unit for effective dose. It is equivalent to J/kg.
μSv	Microsievert
mSv	Millisievert
J	Joule – the SI derived unit of energy. Equivalent to $kg \cdot m^2/s^2$
keV	Kiloelectron–volt
MeV	Megaelectron–volt

eV	Electron–volt – the amount of kinetic energy gained by a single unbound electron when it accelerates through an electrostatic potential difference of $1\ volt$. It is not an SI unit and its value has to be determined experimentally. $1\ eV$ is equivalent to $1.602176487 \times 10^{-19}\ J$ [Levi 04].
FWHM	Full width at half maximum. An expression of the extent of a function, given by the difference between the two extreme values of the independent variable at which the dependent variable is equal to half of its maximum value [Medi 13]
FW(1/10)M	Full width at one-tenth maximum. Similar to FWHM, taking one-tenth of the maximum instead of half
CT	(X-ray) computed tomography
PET	Positron emission tomography
MRI	Magnetic resonance imaging
WHO	World Health Organization
TNM staging system	The system put forward by WHO for staging cancers. *T* stands for *tumor*, *N* for *(lymph) nodal involvement*, *M* for distant *metastasis*.
aerobic respiration	The type of respiration that requires oxygen for energy production [Medi 13]
anaerobic respiration	The type of respiration that does not require oxygen for energy production [Medi 13]
palliative	Relieving or soothing the symptoms of a disease or disorder without effecting a cure [Medi 13]
prognosis	A prediction of the course or outcome of a disease or disorder [Medi 13]
morbidity	Pathological or diseased [Medi 13]

oncology	The branch of medicine that deals with tumors, including study of their development, diagnosis, treatment, and prevention [Medi 13]
physiology	The biological study of the functions of living organisms and their parts [Medi 13]
proliferation	Rapid growth or reproduction of new parts, cells, etc. [Medi 13]
positron	The anti–particle of electron – has the same mass but opposite charge
photon	A quantum of electromagnetic radiation, regarded as a particle with zero rest mass and charge [Medi 13]
pre–	Earlier; before; prior to. Anterior; in front of [Medi 13]
post–	After in time or sequence; following; subsequent. Behind; posterior to [Medi 13]
peri–	A prefix that means *around* (as in peri–cardium) or *near* (as in perihelion) [Medi 13]
p.i.	Post–injection
(radiochemical) purity	The proportion of the total activity of a specific radionuclide in a specific chemical or biologic form [Medi 06]
yield	The amount or quantity produced or returned, often measured as a percentage of the starting material [Medi 06]
RNA	Ribonucleic acid; any of a group of nucleic acids, present in all living cells, that play an essential role in the synthesis of proteins [Medi 13]
translation	The process in the ribosomes of a cell by which a strand of messenger RNA directs the assembly of a sequence of amino acids to make a protein [Medi 13]

Bibliography

[18FF 05] "[18F]Fluoro-2-deoxy-2-D-glucose - Molecular Imaging and Contrast Agent Database (MICAD) - NCBI Bookshelf". http://www.ncbi.nlm.nih.gov/books/NBK23335/, 2005.

[Abde 10] W. Abdel-Rahman and E. B. Podgorsak. "Energy transfer and energy absorption in photon interactions with matter revisited: A step-by-step illustrated approach". *Radiation Physics and Chemistry*, Vol. 79, No. 5, pp. 552–566, May 2010.

[Adam 94] R. Adams and L. Bischof. "Seeded region growing". *IEEE Transactions on Pattern Analysis and Machine Intelligence*, Vol. 16, No. 6, pp. 641–647, June 1994.

[Adam 98] S. Adams, R. P. Baum, T. Stuckensen, K. Bitter, and G. Hör. "Prospective comparison of 18F-FDG PET with conventional imaging modalities (CT, MRI, US) in lymph node staging of head and neck cancer.". *European journal of nuclear medicine*, Vol. 25, No. 9, pp. 1255–1260, Sep. 1998.

[Adle 03] L. P. Adler, E. Anashkin, D. Beylin, G. Devincentes, R. Pani, W. Peter, P. Stepanov, I. Weinberg, V. Zawarzin, and J. C. Zeng. "Flexible geometries for hand-held pet and spect cameras". http://www.google.com/patents/WO2003086170A2?cl=en, Oct. 2003. Publication No: WO2003086170 A2, Publication Type: application.

[Ales 10] A. M. Alessio, E. Butterworth, J. H. Caldwell, and J. B. Bassingthwaighte. "Quantitative imaging of coronary blood flow". *Nano Reviews*, Vol. 1, No. 0, Apr. 2010.

[Apps] "Apps/Dia - GNOME Wiki!". `http://live.gnome.org/Dia`.

[Bech 03] A. Becherer, G. Karanikas, M. Szabó, G. Zettinig, S. Asenbaum, C. Marosi, C. Henk, P. Wunderbaldinger, T. Czech, W. Wadsak, and K. Kletter. "Brain tumour imaging with PET: a comparison between [18F]fluorodopa and [11C]methionine.". *European journal of nuclear medicine and molecular imaging*, Vol. 30, No. 11, pp. 1561–1567, Nov. 2003.

[Blue 13] C. Bluemel, A. Schnelzer, A. Okur, A. Ehlerding, S. Paepke, K. Scheidhauer, and M. Kiechle. "Freehand SPECT for image-guided sentinel lymph node biopsy in breast cancer.". *European journal of nuclear medicine and molecular imaging*, June 2013.

[Boga 09] F. Bogalhas, Y. Charon, M. A. Duval, F. Lefebvre, S. Palfi, L. Pinot, R. Siebert, and L. Ménard. "Development of a positron probe for localization and excision of brain tumours during surgery". *Physics in Medicine and Biology*, Vol. 54, No. 14, p. 4439+, July 2009.

[Bouv 12] V. Bouvet, M. Wuest, P.-H. Tam, M. Wang, and F. Wuest. "Microfluidic technology: An economical and versatile approach for the synthesis of O-(2-[18F]fluoroethyl)-l-tyrosine ([18F]FET)". *Bioorganic & Medicinal Chemistry Letters*, Vol. 22, No. 6, pp. 2291–2295, March 2012.

[Brai 12] "Brain and Spinal Tumors: Hope Through Research". `http://www.ninds.nih.gov/disorders/brainandspinaltumors/detail_brainandspinaltumors.htm`, Nov. 2012. NIH Publication No. 09-504.

[Brai 13] "Brain Tumor Trials". `http://www.mayfieldclinic.com/ClinicalTrials.htm`, 2013.

[Brix 05] G. Brix, U. Lechel, G. Glatting, S. I. Ziegler, W. Münzing, S. P. Müller, and T. Beyer. "Radiation Exposure of Patients Undergoing Whole-Body Dual-Modality 18F-FDG PET/CT Examinations". *Journal of Nuclear Medicine*, Vol. 46, No. 4, pp. 608–613, Apr. 2005.

[Butt 11] P. V. Butte, A. N. Mamelak, M. Nuno, S. I. Bannykh, K. L. Black, and L. Marcu. "Fluorescence lifetime spectroscopy for guided therapy of brain tumors.". *NeuroImage*, Vol. 54 Suppl 1, Jan. 2011.

[Canc 13] "Cancer Topics - National Cancer Institute". `http://www.cancer.gov/cancertopics`, 2013.

[CGAL 13] "CGAL - Computational Geometry Algorithms Library". `http://www.cgal.org/`, 2013.

[Cho 75] Z. H. Cho, J. K. Chan, L. Ericksson, M. Singh, S. Graham, N. S. MacDonald, and Y. Yano. "Positron ranges obtained from biomedically important positron-emitting radionuclides.". *Journal of nuclear medicine : official publication, Society of Nuclear Medicine*, Vol. 16, No. 12, pp. 1174–1176, Dec. 1975.

[Chu 99] S. Y. F. Chu, L. P. Ekström, and R. B. Firestone. "The Lund/LBNL Nuclear Data Search". `http://nucleardata.nuclear.lu.se/toi/`, 1999.

[CMak 13] "CMake - Cross Platform Make". `http://www.cmake.org/`, 2013.

[CogN 08] "CogNeuro Animation". `http://www.sinauer.com/cogneuro/animation_page.html?file=cogneuro_0302.swf&TB_iframe=true&height=450&width=450`, 2008.

[Dagh 94] F. Daghighian, J. C. Mazziotta, E. J. Hoffman, P. Shenderov, B. Eshaghian, S. Siegel, and M. E. Phelps. "Intraoperative beta probe: a device for detecting tissue labeled with positron or electron emitting isotopes during surgery.". *Medical physics*, Vol. 21, No. 1, pp. 153–157, Jan. 1994.

[Delo 98] H. M. Deloar, T. Fujiwara, M. Shidahara, T. Nakamura, H. Watabe, Y. Narita, M. Itoh, M. Miyake, and S. Watanuki. "Estimation of absorbed dose for 2-[F-18]fluoro-2-deoxy-d- glucose using whole-body positron emission tomography and magnetic resonance imaging". *Eur J Nucl Med*, Vol. 25, No. 6, pp. 565–574, June 1998.

[Dole 12] T. A. Dolecek, J. M. Propp, N. E. Stroup, and C. Kruchko. "CBTRUS statistical report: primary brain and central nervous system tumors diagnosed in the United States in 2005-2009.". *Neuro-oncology*, Vol. 14 Suppl 5, Nov. 2012.

[Eber 11] U. Eberlein, J. H. Bröer, C. Vandevoorde, P. Santos, M. Bardiès, K. Bacher, D. Nosske, and M. Lassmann. "Biokinetics and dosimetry of commonly used radiopharmaceuticals in diagnostic nuclear medicine - a review". *Eur J Nucl Med Mol Imaging*, Vol. 38, No. 12, pp. 2269–2281, Dec. 2011.

[Ehrl 11] S. D. Ehrlich. "Tyrosine". `http://www.umm.edu/altmed/articles/tyrosine-000329.htm`, July 2011.

[Eins 05] A. Einstein. "Ist die Trägheit eines Körpers von seinem Energieinhalt abhängig?". *Ann. Phys.*, Vol. 323, No. 13, pp. 639–641, Jan. 1905.

[Essn 01] R. Essner, E. C. Hsueh, P. I. Haigh, E. C. Glass, Y. Huynh, and F. Daghighian. "Application of an [18F]Fluorodeoxyglucose-Sensitive Probe for the Intraoperative Detection of Malignancy". *Journal of Surgical Research*, Vol. 96, No. 1, pp. 120–126, March 2001.

[Fale 12] S. W. Falen, R. A. Hoefer, S. Majewski, J. McKisson, B. Kross, J. Proffitt, and A. G. Weisenberger. "Positron emission tomography and optical tissue imaging". `http://www.google.com/patents/US8183530`, May 2012. Publication No: US 8,183,530 B2, Publication Type: grant.

[Fant 10] S. Fanti, M. Farsad, and L. Mansi. *PET-CT beyond FDG a quick guide to image interpretation*. Springer, Berlin, 2010.

[Fowl 05] J. S. Fowler and T. Ido. "Design and Synthesis of 2-Deoxy-2-[18F]Fluoro-D-Glucose (18FDG)". In: M. J. Welch and C. S. Redvanly, Eds., *Handbook of Radiopharmaceuticals*, pp. 307–321, John Wiley & Sons, Ltd, Chichester, UK, Jan. 2005.

[Frag 08] H. Fraga. "Firefly luminescence: A historical perspective and recent developments". *Photochem. Photobiol. Sci.*, Vol. 7, No. 2, pp. 146–158, 2008.

[Gerg 11] V. M. Gerganov, A. Samii, M. Giordano, M. Samii, and R. Fahlbusch. "Two-dimensional high-end ultrasound imaging compared to intraoperative MRI during resection of low-grade gliomas.". *Journal of clinical neuroscience*, Vol. 18, No. 5, pp. 669–673, May 2011.

[Ghol 11] B. Gholami, N. Y. Agar, F. A. Jolesz, W. M. Haddad, and A. R. Tannenbaum. "A compressive sensing approach for glioma margin delineation using mass spectrometry.". *Conference proceedings : ... Annual International Conference of the IEEE Engineering in Medicine and Biology Society. IEEE Engineering in Medicine and Biology Society. Conference*, Vol. 2011, pp. 5682–5685, 2011.

[Gros 10] A.-L. L. Grosu and W. A. Weber. "PET for radiation treatment planning of brain tumours.". *Radiotherapy and oncology : journal of the European Society for Therapeutic Radiology and Oncology*, Vol. 96, No. 3, pp. 325–327, Sep. 2010.

[Gule 06] S. A. Gulec, F. Daghighian, and R. Essner. "PET-Probe: Evaluation of Technical Performance and Clinical Utility of a Handheld High-Energy Gamma Probe in Oncologic Surgery.". *Annals of surgical oncology*, July 2006.

[Gule 07] S. A. Gulec, E. Hoenie, R. Hostetter, and D. Schwartzentruber. "PET probe-guided surgery: applications and clinical protocol.". *World journal of surgical oncology*, Vol. 5, p. 65+, June 2007.

[Guyt 11] A. C. Guyton and J. E. Hall. *Textbook of Medical Physiology: Enhanced E-book (Guyton Physiology)*. Saunders, 12 Ed., Sep. 2011.

[Hadd 08] R. I. Haddad and D. M. Shin. "Recent Advances in Head and Neck Cancer". *N Engl J Med*, Vol. 359, No. 11, pp. 1143–1154, Sep. 2008.

[Hall 07] N. Hall, S. Povoski, D. Murrey, M. Knopp, and E. Martin. "Combined approach of perioperative 18F-FDG PET/CT imaging and intraoperative 18F-FDG handheld gamma probe detection for tumor localization and verification of complete tumor resection in breast cancer". *World Journal of Surgical Oncology*, Vol. 5, No. 1, p. 143+, Dec. 2007.

[Harp 12] D. Harper. "Online Etymology Dictionary". `http://www.etymonline.com/`, 2012.

[Harr 04] D. M. Harrison. "The Interaction of X-rays With Matter". `http://www.upscale.utoronto.ca/PVB/Harrison/Flash/Nuclear/XRayInteract/XRayInteract.swf`, 2004.

[Head 12] "Head and Neck Cancer". `http://www.cancer.net/cancer-types/head-and-neck-cancer`, July 2012.

[Hoff 04] E. J. Hoffman, M. P. Tornai, M. Janecek, B. E. Patt, and J. S. Iwanczyk. *Intraoperative Probes and Imaging Probes*, pp. 335–358. Elsevier, San Diego, 2004.

[Huh 07] S. S. Huh, W. L. Rogers, and N. H. Clinthorne. "An Investigation of an Intra-Operative PET imaging Probe". In: *2007 IEEE Nuclear Science Symposium Conference Record*, pp. 552–555, IEEE, Oct. 2007.

[Huh 08] S. S. Huh, W. L. Rogers, and N. H. Clinthorne. "On-line sliding-window list-mode PET image reconstruction for a surgical pet imaging probe". In: *2008 IEEE Nuclear Science Symposium Conference Record*, pp. 5479–5484, IEEE, Oct. 2008.

[Huh 09] S. S. Huh, L. Han, W. L. Rogers, and N. H. Clinthorne. "Real time image reconstruction using GPUs for a surgical PET imaging probe system". In: *2009 IEEE Nuclear Science Symposium Conference Record (NSS/MIC)*, pp. 4148–4153, IEEE, Oct. 2009.

[Ishi 02] T. Ishimori, T. Saga, M. Mamede, H. Kobayashi, T. Higashi, Y. Nakamoto, N. Sato, and J. Konishi. "Increased 18F-FDG Uptake in a Model of Inflammation: Concanavalin A-Mediated Lymphocyte Activation". *Journal of Nuclear Medicine*, Vol. 43, No. 5, pp. 658–663, May 2002.

[Ius 12] T. Ius, M. Isola, R. Budai, G. Pauletto, B. Tomasino, L. Fadiga, and M. Skrap. "Low-grade glioma surgery in eloquent areas: volumetric analysis of extent of resection and its impact on overall survival. A single-institution experience in 190 patients: clinical article.". *Journal of neurosurgery*, Vol. 117, No. 6, pp. 1039–1052, Dec. 2012.

[Jack 06] R. S. Jackson, T. C. Schlarman, W. L. Hubble, and M. M. Osman. "Prevalence and Patterns of Physiologic Muscle Uptake Detected

with Whole-Body 18F-FDG PET". *Journal of Nuclear Medicine Technology*, Vol. 34, No. 1, pp. 29–33, March 2006.

[Jage 01] P. L. Jager, W. Vaalburg, J. Pruim, E. G. de Vries, K. J. Langen, and D. A. Piers. "Radiolabeled amino acids: basic aspects and clinical applications in oncology". *Journal of nuclear medicine: official publication, Society of Nuclear Medicine*, Vol. 42, No. 3, pp. 432–445, March 2001. PMID: 11337520.

[Judy 07] P. G. Judy, B. Welch, T. St. Saviour, D. Kieper, S. Majewski, J. McKisson, B. Kross, J. Proffitt, A. Stolin, M. J. More, N. L. Dinion, and M. B. Williams. "Molecular breast imaging with directly opposing compact gamma cameras". In: *2007 IEEE Nuclear Science Symposium Conference Record*, pp. 4040–4043, IEEE, 2007.

[Judy 10] P. G. Judy, Z. Gong, N. L. Dinion, B. L. Welch, T. St. Saviour, D. Kieper, S. Majewski, J. McKisson, B. Kross, J. Proffitt, A. V. Stolin, M. J. More, and M. B. Williams. "Analysis of Image Combination Methods for Conjugate Breast Scintigraphy". *IEEE Transactions on Nuclear Science*, Vol. 57, No. 3, pp. 1146–1154, June 2010.

[Kim 11] W. W. W. Kim, J. S. S. Kim, S. M. M. Hur, S. H. H. Kim, S.-K. K. Lee, J. H. H. Choi, S. Kim, J. Y. Y. Choi, J. E. E. Lee, J.-H. H. Kim, S. J. J. Nam, J.-H. H. Yang, and J.-H. H. Choe. "Radioguided surgery using an intraoperative PET probe for tumor localization and verification of complete resection in differentiated thyroid cancer: a pilot study.". *Surgery*, Vol. 149, No. 3, pp. 416–424, March 2011.

[Kyrk 12] J. Kyrk. "glycolysis". `http://www.johnkyrk.com/glycolysis.html`, 2012.

[Lalu 04] D. S. Lalush and M. N. Wernick. *Iterative Image Reconstruction*, pp. 443–472. Elsevier, 2004.

[Laur] A. Lauria, G. Mettivier, M. C. Montesi, L. Aloj, S. Lastoria, and P. Russo. "Experimental study for an intraoperative probe for 18F imaging with a silicon pixel detector". `http//iworid-8.df.unipi.it/presentations/lauria.pdf`.

[Laur 07] A. Lauria, G. Mettivier, M. C. Montesi, L. Aloj, S. Lastoria, M. Aurilio, and P. Russo. "Experimental study for an intraoperative probe for 18F imaging with a silicon pixel detector". *Nuclear Instruments and Methods in Physics Research Section A: Accelerators, Spectrometers, Detectors and Associated Equipment*, Vol. 576, No. 1, pp. 198–203, June 2007.

[Leun 05] K. Leung. "O-(2-[18F]Fluoroethyl)-L-tyrosine - Molecular Imaging and Contrast Agent Database (MICAD) - NCBI Bookshelf". `http://www.ncbi.nlm.nih.gov/books/NBK23454/`, 2005.

[Levi 04] C. Levin. "Chapter 4 - Basic Physics of Radionuclide Imaging". In: M. N. Wernick, Ph.D., and P. John N. Aarsvold, Eds., *Emission Tomography*, pp. 53–88, Academic Press, San Diego, 2004.

[Levi 99] C. S. Levin and E. J. Hoffman. "Calculation of positron range and its effect on the fundamental limit of positron emission tomography system spatial resolution". *Phys. Med. Biol.*, Vol. 44, No. 3, p. 781, 1999. `http://dx.doi.org/10.1088/0031-9155/44/3/019`.

[Lewe 04] T. Lewellen and J. Karp. *PET Systems*, pp. 179–194. Elsevier, 2004.

[Li 10] F. Li, C. Shen, and C. Li. "Multiphase Soft Segmentation with Total Variation and H1 Regularization". *J. Math. Imaging Vis.*, Vol. 37, No. 2, pp. 98–111, June 2010.

[Loui 07] D. N. Louis, H. Ohgaki, O. D. Wiestler, W. K. Cavenee, P. C. Burger, A. Jouvet, B. W. Scheithauer, and P. Kleihues. "The 2007 WHO classification of tumours of the central nervous system.". *Acta neuropathologica*, Vol. 114, No. 2, pp. 97–109, Aug. 2007.

[MacD 95] L. R. MacDonald, M. P. Tornai, C. S. Levin, J. Park, M. Atac, D. B. Cline, and E. J. Hoffman. "Investigation of the physical aspects of beta imaging probes using scintillating fibers and visible light photon counters". In: *Proceedings of 1994 IEEE Nuclear Science Symposium - NSS'94*, pp. 1380–1384, IEEE, 1995.

[Maje 10a] S. Majewski and N. H. Clinthorne. "High Resolution PET Imaging Probe for the Detection, Molecular Characterization and Treatment

Monitoring of Prostate Cancer". Tech. Rep., Defense Technical Information Center (DTIC®)), July 2010.

[Maje 10b] S. Majewski and J. Proffitt. "Dedicated mobile high resolution prostate PET imager with an insertable transrectal probe". `http://www.google.com/patents/US20100187424`, 2010. Publication No: US 2010/0187424 A1, Publication Type: application.

[Maje 11a] S. Majewski, A. Stolin, E. Delfino, P. Martone, and J. Proffitt. "High resolution fast stereotactic PET imager for prostate biopsy". In: *2011 IEEE Nuclear Science Symposium Conference Record*, pp. 3406–3409, IEEE, Oct. 2011.

[Maje 11b] S. Majewski, A. Stolin, P. Martone, and R. Raylman. "Dedicated mobile PET prostate imager". *J NUCL MED MEETING ABSTRACTS*, Vol. 52, No. 1_MeetingAbstracts, p. 1945, 2011.

[MARG 13] "MARGINator Beta Camera (investigational)". `http://www.gammaprobe.com/marginator/`, 2013.

[McGi 08] M. J. McGirt, K. L. Chaichana, F. J. Attenello, J. D. Weingart, K. Than, P. C. Burger, A. Olivi, H. Brem, and A. Quinoñes Hinojosa. "Extent of surgical resection is independently associated with survival in patients with hemispheric infiltrating low-grade gliomas.". *Neurosurgery*, Vol. 63, No. 4, pp. 700–708, Oct. 2008.

[McPh 08] C. McPherson and T. Orgon-Stamper. "Glioma brain tumors (astrocytoma, oligodendroglioma, glioblastoma)". `http://www.mayfieldclinic.com/PE-Glioma.htm`, Nov. 2008.

[Medi 06] "Medical Dictionary – Comprehensive Medical Terminology Search". http://www.medilexicon.com/medicaldictionary.php, 2006.

[Medi 13] "Medical Dictionary". `http://medical-dictionary.thefreedictionary.com/`, 2013.

[Mell 06] B. Meller, K. Sommer, J. Gerl, K. von Hof, A. Surowiec, E. Richter, B. Wollenberg, and M. Baehre. "High energy probe for detecting lymph node metastases with 18F-FDG in patients with head and neck

cancer.". *Nuklearmedizin. Nuclear medicine*, Vol. 45, No. 4, pp. 153–159, 2006.

[Moli 12] J. A. Moliterno, T. R. Patel, and J. M. Piepmeier. "Neurosurgical approach.". *Cancer journal (Sudbury, Mass.)*, Vol. 18, No. 1, pp. 20–25, 2012.

[NCI 13] "NCI Dictionary of Cancer Terms - National Cancer Institute". `http://www.cancer.gov/dictionary`, 2013.

[Neur 11] "Neurological Diagnostic Tests and Procedures". `http://www.ninds.nih.gov/disorders/misc/diagnostic_tests.htm`, Aug. 2011. NIH Publication No. 05-5380.

[NRC 12a] "NRC: Glossary". `http://www.nrc.gov/reading-rm/basic-ref/glossary.html`, 2012.

[NRC 12b] "NRC: Radiation And Its Health Effects". `http://www.nrc.gov/about-nrc/radiation/rad-health-effects.html`, 2012.

[Nucl 08] "Nuclear Instrumentation Research: Beta Probe". `http://www.hsc.wvu.edu/cai/raylman/betaProbe.asp`, Feb. 2008.

[Okur 13] A. Okur, D. I. Shakir, P. Matthies, A. Hartl, S. I. Ziegler, M. Essler, T. Lasser, and N. Navab. "Freehand Tomographic Nuclear Imaging Using Tracked High-Energy Gamma Probes". In: H.-P. Meinzer, T. M. Deserno, H. Handels, and T. Tolxdorff, Eds., *Bildverarbeitung für die Medizin 2013*, pp. 362–367, Springer Berlin Heidelberg, 2013.

[Orri 12] D. Orringer, D. Lau, S. Khatri, G. J. Zamora-Berridi, K. Zhang, C. Wu, N. Chaudhary, and O. Sagher. "Extent of resection in patients with glioblastoma: limiting factors, perception of resectability, and effect on survival.". *Journal of neurosurgery*, Vol. 117, No. 5, pp. 851–859, Nov. 2012.

[Ozgu 09a] C. Özgür. *An iterative reconstruction framework for "Surface PET": Positron activity surface imaging using tracked beta probes for intraoperative control of resection borders in cancer surgery*. Master's thesis, Technische Universität München, Feb. 2009.

[Ozgu 09b] C. Özgür, J. Bieniarz, T. Lasser, S. I. Ziegler, N. Navab, and T. Wendler. "Phenomenological Models for Intraoperative Positron Emission Surface Imaging using Handheld Probes". In: O. Dössel and W. C. Schlegel, Eds., *World Congress on Medical Physics and Biomedical Engineering, September 7 - 12, 2009, Munich, Germany*, pp. 213–216, Springer Berlin Heidelberg, 2009.

[Panc 12] P. P. P. Panciani, M. Fontanella, B. Schatlo, D. Garbossa, A. Agnoletti, A. Ducati, and M. Lanotte. "Fluorescence and image guided resection in high grade glioma.". *Clinical neurology and neurosurgery*, Vol. 114, No. 1, pp. 37–41, Jan. 2012.

[Paul 03] D. Pauleit, F. Floeth, H. Herzog, K. Hamacher, L. Tellmann, H.-W. Müller, H. H. Coenen, and K.-J. Langen. "Whole-body distribution and dosimetry of O-(2-[18F]fluoroethyl)-L-tyrosine". *Eur. J. Nucl. Med. Mol. Imaging*, Vol. 30, No. 4, pp. 519–524, Apr. 2003. PMID: 12589478.

[Phys 10] "Physical Measurements Laboratory". http://physics.nist.gov/PhysRefData/Xcom/html/xcom1.html, Aug. 2010.

[Pier 07] M. Piert, M. Burian, G. Meisetschläger, H. J. Stein, S. Ziegler, J. Nährig, M. Picchio, A. Buck, J. R. Siewert, and M. Schwaiger. "Positron detection for the intraoperative localisation of cancer deposits.". *European journal of nuclear medicine and molecular imaging*, Vol. 34, No. 10, pp. 1534–1544, Oct. 2007.

[Pola 13] "Polaris Vicra Measurement Volume". `http://www.ndigital.com/medical/polarisfamily-volumes-vicra.php`, 2013.

[Popp 04] G. Pöpperl, C. Götz, W. Rachinger, F.-J. J. Gildehaus, J.-C. C. Tonn, and K. Tatsch. "Value of O-(2-[18F]fluoroethyl)- L-tyrosine PET for the diagnosis of recurrent glioma.". *European journal of nuclear medicine and molecular imaging*, Vol. 31, No. 11, pp. 1464–1470, Nov. 2004.

[Povo 08] S. Povoski, N. Hall, E. Martin, and M. Walker. "Multimodality approach of perioperative 18F-FDG PET/CT imaging, intraoperative

18F-FDG handheld gamma probe detection, and intraoperative ultrasound for tumor localization and verification of resection of all sites of hypermetabolic activity in a case of occult recurrent metastatic melanoma". *World Journal of Surgical Oncology*, Vol. 6, No. 1, p. 1+, Jan. 2008.

[Povo 09] S. Povoski, R. Neff, C. Mojzisik, D. O'Malley, G. Hinkle, N. Hall, D. Murrey, M. Knopp, and E. Martin. "A comprehensive overview of radioguided surgery using gamma detection probe technology". *World Journal of Surgical Oncology*, Vol. 7, No. 1, p. 11+, Jan. 2009.

[Rayl 01] R. R. Raylman. "Performance of a dual, solid-state intraoperative probe system with 18F, 99mTc, and (111)In.". *Journal of nuclear medicine : official publication, Society of Nuclear Medicine*, Vol. 42, No. 2, pp. 352–360, Feb. 2001.

[Read 07] A. J. Reader and H. Zaidi. "Advances in PET Image Reconstruction". *PET Clinics*, Vol. 2, No. 2, pp. 173–190, Apr. 2007.

[Reic 13] T. Reichl. *Advanced Hybrid Tracking and Navigation for Computer-Assisted Interventions*. PhD thesis, Technische Universität München, 2013.

[Rick 92] D. W. Rickey, R. Gordon, and W. Huda. "On lifting the inherent limitations of positron emission tomography by using magnetic fields (MagPET)". *Automedica*, Vol. 14, pp. 355–369, Nov. 1992.

[Robe 12] D. W. Roberts, P. A. Valdés, B. T. Harris, A. Hartov, X. Fan, S. Ji, B. W. Pogue, F. Leblond, T. D. Tosteson, B. C. Wilson, and K. D. Paulsen. "Adjuncts for maximizing resection: 5-aminolevuinic acid.". *Clinical neurosurgery*, Vol. 59, pp. 75–78, 2012.

[Roes 12] K. Roessler, A. Becherer, M. Donat, M. Cejna, and I. Zachenhofer. "Intraoperative tissue fluorescence using 5-aminolevolinic acid (5-ALA) is more sensitive than contrast MRI or amino acid positron emission tomography ((18)F-FET PET) in glioblastoma surgery.". *Neurological research*, Vol. 34, No. 3, pp. 314–317, Apr. 2012.

[Russ 08] P. Russo, A. Lauria, G. Mettivier, M. C. Montesi, M. Marotta, L. Aloj, and S. Lastoria. "18F-FDG positron autoradiography with a parti-

cle counting silicon pixel detector". *Physics in Medicine and Biology*, Vol. 53, No. 21, p. 6227+, Nov. 2008.

[Rusu 11] R. B. Rusu and S. Cousins. "3D is here: Point Cloud Library (PCL)". In: *IEEE International Conference on Robotics and Automation (ICRA)*, Shanghai, China, May 9-13 2011.

[SEERa] "SEER Training Modules, *Anatomy & Physiology*. U.S. National Institutes of Health, National Cancer Institute. 25, June 2013". `http://training.seer.cancer.gov/anatomy/respiratory/passages/pharynx.html`.

[SEERb] "SEER Training Modules, *Head & Neck Cancer*. U.S. National Institutes of Health, National Cancer Institute. 25, June 2013". `http://training.seer.cancer.gov/head-neck/anatomy/overview.html`.

[Selb 12] T. Selbekk, R. Brekken, M. Indergaard, O. Solheim, and G. Unsgard. "Comparison of contrast in brightness mode and strain ultrasonography of glial brain tumours". *BMC Medical Imaging*, Vol. 12, No. 1, p. 11+, May 2012.

[Shak 10a] D. I. Shakir, J. Bieniarz, S. Pirsig, T. Wendler, N. Navab, and S. I. Ziegler. "A first study on biological feasibility of intraoperative control of tumor resection borders with navigated beta-probe surface imaging". In: *Proceedings of the Annual Meeting of the Society of Nuclear Medicine (SNM)*, June 2010.

[Shak 10b] D. I. Shakir, N. Navab, and S. I. Ziegler. "Acquisition Model for Iterative Reconstruction of Navigated Beta-Probe Surface Images". In: *Proceedings of the IEEE Nuclear Science Symposium and Medical Imaging Conference (NSS-MIC)*, Nov. 2010.

[Shak 11a] D. I. Shakir, A. Hartl, N. Navab, and S. I. Ziegler. "Evaluation of an ad hoc model of detection physics for navigated beta-probe surface imaging". In: K. H. Wong and D. R. Holmes, Eds., *Proceedings of SPIE Visualization, Image-Guided Procedures, and Modeling Conference*, pp. 796405–796405–7, March 2011.

[Shak 11b] D. I. Shakir, T. Lasser, A. Drzezga, S. I. Ziegler, and N. Navab. "Evaluation of Navigated Beta-Probe Surface Imaging on a Realistic 3D Phantom". In: *Proceedings of the IEEE Nuclear Science Symposium and Medical Imaging Conference (NSS-MIC)*, Oct. 2011.

[Shak 12a] D. I. Shakir, A. Hartl, F. R. Schneider, J. Pulko, S. I. Ziegler, N. Navab, and T. Lasser. "Two new ad-hoc models of detection physics and their evaluation for navigated beta probe surface imaging". In: D. R. Holmes and K. H. Wong, Eds., *Proceedings of SPIE Visualization, Image-Guided Procedures, and Modeling Conference*, pp. 83162G–83162G–6, Feb. 2012.

[Shak 12b] D. I. Shakir, A. Okur, A. Hartl, P. Matthies, S. I. Ziegler, M. Essler, T. Lasser, and N. Navab. "Towards intra-operative PET for head and neck cancer: lymph node localization using high-energy probes.". *Medical image computing and computer-assisted intervention : MICCAI ... International Conference on Medical Image Computing and Computer-Assisted Intervention*, Vol. 15, No. Pt 1, pp. 430–437, 2012.

[Shan 06] L. K. Shankar, J. M. Hoffman, S. Bacharach, M. M. Graham, J. Karp, A. A. Lammertsma, S. Larson, D. A. Mankoff, B. A. Siegel, A. Van den Abbeele, J. Yap, and D. Sullivan. "Consensus Recommendations for the Use of 18F-FDG PET as an Indicator of Therapeutic Response in Patients in National Cancer Institute Trials". *Journal of Nuclear Medicine*, Vol. 47, No. 6, pp. 1059–1066, June 2006.

[Shes 06] I. Shestakova, V. V. Nagarkar, V. Gaysinskiy, G. Entine, B. C. Stack, and B. Miller. "Feasibility studies of an EMCCD-based beta imaging probe for radioguided thyroid surgery". In: L. A. Franks, A. Burger, R. B. James, H. B. Barber, F. P. Doty, and H. Roehrig, Eds., *Proc. SPIE 6319, Hard X-Ray and Gamma-Ray Detector Physics and Penetrating Radiation Systems VIII*, pp. 63191E–63191E–9, Aug. 2006.

[Shes 07] I. Shestakova, V. B. Gaysinskiy, S. C. Thacker, S. Cool, V. V. Nagarkar, and B. C. Stack. "High-resolution beta imaging probe for radioguided surgery". In: F. P. Doty, H. B. Barber, and H. Roehrig, Eds., *Proc. SPIE 6707, Penetrating Radiation Systems and Applications VIII*, pp. 67070G–67070G–7, Sep. 2007.

[Sing 09] B. Singh, B. Stack, S. Thacker, V. Gaysinskiy, S. Cool, G. Entine, and V. Nagarkar. "In vivo imaging of lingual cancer in a rabbit model using a hand-held imaging beta probe". In: *2009 IEEE Nuclear Science Symposium Conference Record (NSS/MIC)*, pp. 3038–3041, IEEE, Oct. 2009.

[Sing 13] B. Singh, B. C. Stack, S. Thacker, V. Gaysinskiy, T. Bartel, V. Lowe, S. Cool, G. Entine, and V. Nagarkar. "A hand-held beta imaging probe for FDG.". *Annals of nuclear medicine*, Vol. 27, No. 3, pp. 203–208, Apr. 2013.

[Stol 08] A. Stolin, C. Freeman, B. Kross, J. McKisson, J. Proffitt, S. Majewski, S. Falen, and B. Welch. "Dual modality planar PET/optical scanner for imaging of surgical margins in extracted tissue samples". In: *2008 IEEE Nuclear Science Symposium Conference Record*, pp. 4845–4847, IEEE, Oct. 2008.

[Stol 09] A. V. Stolin, A. G. Weisenberger, J. E. McKisson, and S. Majewski. "Feasibility study of using detection of direct positrons in plant imaging research". In: *2009 IEEE Nuclear Science Symposium Conference Record (NSS/MIC)*, pp. 2338–2341, IEEE, Oct. 2009.

[Stol 10] A. V. Stolin, S. Majewski, R. R. Raylman, and H. W. Hazard. "Fingertip beta imager based on the SiPM technology". In: *IEEE Nuclear Science Symposuim & Medical Imaging Conference*, pp. 2595–2597, IEEE, Oct. 2010.

[Stol 11] A. V. Stolin, S. Majewski, R. R. Raylman, and P. Martone. "Hand-Held SiPM-Based PET Imagers for Surgical Applications". In: *Proceedings of IEEE Nuclear Science Symposium and Medical Imaging Conference (IEEE NSS-MIC)*, Valencia, Spain, Oct. 2011.

[Stol 13] A. V. Stolin, S. Majewski, G. Jaliparthi, and R. R. Raylman. "Construction and Evaluation of a Prototype High Resolution, Silicon Photomultiplier-Based, Tandem Positron Emission Tomography System". *IEEE Transactions on Nuclear Science*, Vol. 60, No. 1, pp. 82–86, Feb. 2013.

[Stro 09] V. E. Strong, C. J. Galanis, C. C. Riedl, V. A. Longo, F. Daghighian, J. L. Humm, S. M. Larson, and Y. Fong. "Portable PET probes are a novel tool for intraoperative localization of tumor deposits.". *Annals of surgical innovation and research*, Vol. 3, 2009.

[Stru 03] D. Strulab, G. Santin, D. Lazaro, V. Breton, and C. Morel. "GATE (geant4 application for tomographic emission): a PET/SPECT general-purpose simulation platform". *Nuclear Physics B - Proceedings Supplements*, Vol. 125, pp. 75–79, Sep. 2003.

[Thac 08] S. C. Thacker, B. C. Stack, V. Lowe, V. Gaysinskiy, S. Cool, V. V. Nagarkar, and G. Entine. "A novel imaging beta probe for radio-guided surgery". In: *2008 IEEE Nuclear Science Symposium Conference Record*, pp. 3875–3878, IEEE, Oct. 2008.

[The 13a] "The PubChem Project". `http://pubchem.ncbi.nlm.nih.gov/`, 2013.

[The 13b] "The ENDOTOFPET-US". `https://endotofpet-us.web.cern.ch/endotofpet-us/Default.html`, 2013.

[Theo 12] P. Theodosopoulos. "Brain tumors: an introduction". `http://www.mayfieldclinic.com/PE-BrainTumor.htm`, March 2012.

[TRIO 09] "TRIOP, une sonde positon pour la chirurgie des tumeurs cérébrales". `http://www.imnc.in2p3.fr/spip.php?article119&lang=fr`, Nov. 2009.

[Turk 04] T. G. Turkington, M. F. Smith, T. C. Hawk, S. Majewski, B. J. Kross, R. Wojcik, A. G. Weisenberger, T. R. DeGrado, and R. E. Coleman. "PET prostate imaging with small planar detectors". In: *IEEE Symposium Conference Record Nuclear Science 2004.*, pp. 2806–2809, IEEE, 2004.

[Vale 07] J. Valentin. "The 2007 Recommendations of the International Commission on Radiological Protection". *Annals of the ICRP*, Vol. 37, No. 2-4, p. 1, 2007.

[Vale 08] J. Valentin. "Radiation dose to patients from radiopharmaceuticals: (Addendum 3 to ICRP Publication 53) ICRP Publication 106 Ap-

proved by the Commission in October 2007". *Annals of the ICRP*, Vol. 38, No. 1-2, pp. 1–198, Apr. 2008.

[Vu 06] N. T. Vu, Y. H. Chung, Z. T. F. Yu, R. W. Silverman, R. Taschereau, R. Farrell, K. S. Shah, Hsian-RongTseng, and A. F. Chatziioannou. "Direct Detection of Beta Particles on a Microfluidic Chip using Position Sensitive APDs". In: *Nuclear Science Symposium Conference Record, 2006. IEEE*, pp. 3536–3539, IEEE, Oct. 2006.

[Vu 11] N. T. Vu, Z. T. Yu, B. Comin-Anduix, J. N. Søndergaard, R. W. Silverman, C. Y. Chang, A. Ribas, H.-R. R. Tseng, and A. F. Chatziioannou. "A beta-camera integrated with a microfluidic chip for radioassays based on real-time imaging of glycolysis in small cell populations.". *Journal of nuclear medicine : official publication, Society of Nuclear Medicine*, Vol. 52, No. 5, pp. 815–821, May 2011.

[Wats 04] C. C. Watson, D. W. Townsend, and B. Bendriem. *PET/CT Systems*, pp. 195–212. Elsevier, 2004.

[Wein 01] I. N. Weinberg, V. Zavarzin, P. Stepanov, D. Beiline, R. Pani, G. DeVincentes, J. C. Zeng, and L. P. Adler. "Flexible geometries for hand-held PET and SPECT cameras". In: *Nuclear Science Symposium Conference Record, 2001 IEEE*, pp. 1133–1136 vol.2, IEEE, Nov. 2001.

[Weis 10] A. G. Weisenberger, A. Stolin, B. Kross, S. J. Lee, S. Majewski, J. McKisson, J. E. McKisson, W. Xi, C. Zorn, C. R. Howell, A. S. Crowell, C. D. Reid, and M. F. Smith. "Compact beta particle/positron imager for plant biology". In: *IEEE Nuclear Science Symposuim & Medical Imaging Conference*, pp. 1752–1754, IEEE, Oct. 2010.

[Wend 06] T. Wendler, J. Traub, S. I. I. Ziegler, and N. Navab. "Navigated three dimensional beta probe for optimal cancer resection.". *Medical image computing and computer-assisted intervention : MICCAI ... International Conference on Medical Image Computing and Computer-Assisted Intervention*, Vol. 9, No. Pt 1, pp. 561–569, 2006.

[Wend 07] T. Wendler, A. Hartl, T. Lasser, J. Traub, F. Daghighian, S. I. Ziegler, and N. Navab. "Towards intra-operative 3D nuclear imaging: reconstruction of 3D radioactive distributions using tracked gamma

probes.". *Medical image computing and computer-assisted intervention : MICCAI ... International Conference on Medical Image Computing and Computer-Assisted Intervention*, Vol. 10, No. Pt 2, pp. 909–917, 2007.

[Wend 08] T. Wendler, I. Faure de Pebeyre, T. Lasser, and N. Navab. "Integrated Surface Acquisition for Hand-Held Probes". p. BTuF58+, Optical Society of America, March 2008.

[Wern 04] M. N. Wernick and J. N. Aarsvold. "Introduction to Emission Tomography". In: *Emission Tomography*, pp. 11–23, Elsevier, 2004.

[Whit 04] I. R. Whittle. "The dilemma of low grade glioma". *Journal of Neurology, Neurosurgery & Psychiatry*, Vol. 75, No. suppl 2, pp. ii31–ii36, June 2004.

[Whit 77] J. O. Whitehurst and C. A. Droulias. "Surgical treatment of squamous cell carcinoma of the oral tongue: factors influencing survival.". *Archives of otolaryngology (Chicago, Ill. : 1960)*, Vol. 103, No. 4, pp. 212–215, Apr. 1977.

[Wilk 04] F. Wilkinson. *Scintillators*, pp. 229–254. Elsevier, 2004.

[Zeng 04] G. L. Zeng, J. R. Galt, M. N. Wernick, R. A. Mintzer, and J. N. Aarsvold. *Single-Photon Emission Computed Tomography*, pp. 127–152. Elsevier, 2004.